Theoretical and Applied Fracture Mechanics 140 (2025) 105142

Contents lists available at ScienceDirect

Theoretical and Applied Fracture Mechanics

journal homepage: www.elsevier.com/locate/tafmec

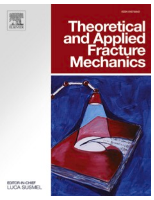

Overview of interfacial fracture toughness testing of ceramic coatings at room and elevated temperatures

Borhan Uddin Manam [a,*], Nico Langhof [a], Carolin Sitzmann [a,d], Stefan Schafföner [a,b,c]

[a] *University of Bayreuth, Chair of Ceramic Materials Engineering, Prof.-Rüdiger-Bormann-Str. 1, 95447 Bayreuth, Germany*
[b] *Bayreuth Center for Materials Science and Engineering, Prof.-Rüdiger-Bormann-Str. 1, 95447 Bayreuth, Germany*
[c] *Bavarian Polymer Institute, Universitätsstraße 30, 95447 Bayreuth, Germany*
[d] *Fraunhofer ISC, Center for High Temperature Materials and Design HTL, Gottlieb-Keim-Straße 62, 95448 Bayreuth, Germany*

ARTICLE INFO

Keywords:
Delamination
Interfacial fracture toughness
Adhesion
Thermal barrier coatings
Environmental barrier coatings

ABSTRACT

Ceramic coatings such as thermal barrier coatings (TBC), environmental barrier coatings (EBC) and electrodes in solid oxide cells (SOCs) are exposed to high temperatures during operation. Due to the harsh operating environments, these types of layered materials go through various types of thermal cyclic loads and stress conditions, which lead to damage and failure. In order to prolong their life span and understand the failure mechanisms of these coatings, the interfacial adhesion between coatings to substrates of these highly configurated systems is essential. Various test methods have been developed to understand the interfacial mechanical properties of these materials. In this comprehensive review, the test methodologies of multilayered ceramic coatings at room and elevated temperatures along with the microstructure, merits and limitations are discussed. Certain criteria are proposed to conduct interfacial fracture tests depending on the applicability of ceramic coatings.

1. Introduction

Ceramic materials are used for their unique properties of being high temperature and corrosion-resistant [1–4]. Because of these advantages, ceramic materials are applied as protective coatings for high temperature operating conditions and harsh environments. These protective coatings are applied in gas turbines of aerospace propulsion systems particularly as thermal barrier coatings (TBC) to protect the underlying metallic substrates [5–7]. Furthermore, these coatings are also used as environmental barrier coatings (EBC) to protect the underlying ceramic substrates [8,9]. Ceramic coatings include oxides, carbides, nitrides, borides [10] or cermet materials as well as perovskites in functional materials such as solid oxide cells (SOC), where these coatings are known as electrodes [11–13]. Another major application of ceramic coatings is in the field of electronics and microelectronic devices [14], dielectrics [15,16] and semiconductors [17]. The fabrication of these ceramic coatings is conducted by methods such as sol–gel synthesis, atmospheric plasma spraying (APS), physical vapor deposition (PVD), electron beam physical vapor deposition (EB-PVD), chemical vapor deposition (CVD), dipping, laser assisted deposition, screen printing or micro-arc deposition technique [10]. The specific fabrication method depends on the necessary mechanical and functional properties. For this present review, the focus is given to TBCs, EBCs and SOCs as they are multilayered coating systems operating at high temperature and harsh environments.

Schematics of conventional TBC, EBC and an electron microscopy image of a solid oxide electrolysis cell (SOEC) are illustrated in Figs. 1 to 3. It can be observed from Figs. 1 to 3 that these systems have a complex structure. Thus, for the robustness and functional properties of these material systems, it is necessary to understand the interfacial adhesion property between the substrates and coatings in the case of TBCs and EBCs, and the interfacial properties between the electrolyte and the electrode for SOCs. Especially to prolong the lifetime for the above-mentioned three systems, it is necessary to determine the interfacial adhesion property between the coating and the substrate along with the failure behavior and mechanisms. Various failure mechanisms such as cracks, delamination, buckling and spallation have been reported [18–22]. Among them, delamination is one of the major damages which is observed in ceramic coatings [23,24]. Delaminations are often caused by mechanical or thermal loads leading to crack growth. This crack growth causes ultimate detachment of the coating from the substrate [20,21].

As mentioned above, delamination is one of the major damages in coatings. Thus, earlier reported reviews focused mostly on single

---

[*] Corresponding author.
E-mail address: borhan.manam@uni-bayreuth.de (B.U. Manam).

https://doi.org/10.1016/j.tafmec.2025.105142
Received 9 May 2025; Received in revised form 28 July 2025; Accepted 1 August 2025

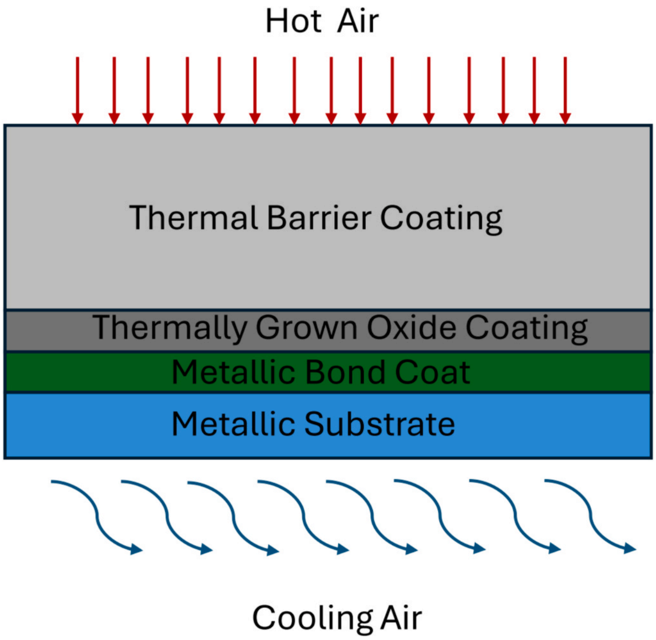

Fig. 1. Schematic of common TBC structure (adopted from Ref. [25]).

coating/substrate systems to evaluate the delamination and the interfacial fracture toughness using indentation methods and other mechanical methods [28,29]. However, no review has yet been published to focus on the failure and interfacial adhesion properties in multilayered ceramic coatings. Therefore, in this overview article, for the first time different test methodologies to study the interfacial adhesion properties in multi-layered coating systems such as TBC, EBC and SOC conducted at room and elevated temperatures along with their advantages and disadvantages have been summarized. It is to be mentioned that the methods performed to determine the interfacial adhesion properties for these types of systems are also transferable to electronics and microelectronics devices. Additionally, certain criteria are proposed to choose and apply suitable interfacial fracture tests because these criteria provide quantitative values for stress distribution at the interface of coating and substrate and will help to design these types of complex systems. Furthermore, these criteria will direct how to conduct valid interfacial fracture toughness tests in TBCs, EBCs and SOCs as these valid tests will contribute to the further development and long-term operation of such coatings.

2. Cohesive and adhesive failures in coatings

In the introduction, it is mentioned that various types of failures that occur in coatings will be discussed. Here, in this section the various types of failures in coatings along with schematics, microstructures and reasons for coating failure are described.

According to ASTM Designation D 907, adhesion is defined as “the state in which two surfaces are held together by interfacial forces. These interfacial forces may consist of valence forces or interlocking action, or both” [28]. The failure between the coating and substrates can be cohesive or adhesive. Cohesive failure is the failure occurring inside the coating and after some time leading to the debonding of the coating and substrate. Adhesive failure can be defined as the failure taking place in between the interface of the coating and the substrate.

Adhesion failure can occur due to several reasons. A coating/substrate system is a layered system which is analogous to laminated composites, thus different reasons for delamination in composites will also occur with the coating/substrate system. For example, various types of defects in physical vapor deposition (PVD) coatings are depicted in Fig. 4. The most common reason for adhesion failure is the coefficient of thermal expansion (CTE) mismatch during heating and cooling (thermocycling). In TBC, the CTE-mismatch acts as the main crack driving force [30]. Thus, bond coats (BC) are applied to reduce the mismatch, so that the substrate cannot be exposed to oxidation [31]. Another reason for failure of coatings is corrosion in TBCs and EBCs [32]. In case of TBC in blades of turbines of aircrafts, the coatings are exposed to high temperature oxidation, particle erosion and water vapor [33] as well as calcium–magnesium–alumina–silicate (CMAS) attack during service. This CMAS corrosion is one of the major reasons for coating failure on turbine blades [34–37].

Like in laminated composites, the impact of foreign objects on the coatings can generate cracks leading to coating failure after a certain period. This foreign object damage (FOD) (see Fig. 5) is caused by large particles moving at low velocities or small particles moving at high velocities. In TBC, this type of failure is characterized by significant deformation of the coatings which can penetrate to the substrate, accompanied by gross plasticity, deformation of the columns, shear bands and extensive cracking [39–45]. The delamination due to CMAS penetration resulting from thermal gradients is presented in Fig. 6 and failures in EBCs after thermal exposure or corrosion is displayed in Fig. 7.

This delamination is also observed in solid oxide cells. A typical delamination in solid oxide fuel cells (SOFC) at the cathode side is shown in Fig. 8 and the delamination at the air electrode after electrolysis operation is presented in Fig. 9.

3. Interfacial fracture toughness of ceramic coatings

In the previous section, various types of failure which occur in coatings were briefly discussed. Among those failure types, crack and delamination resistance is defined by interfacial fracture toughness. In this section, the definition of interfacial fracture toughness, different fracture modes and phase angle for mixed-mode fracture behavior including schematics are briefly described.

The interfacial fracture toughness of a coating/substrate system is characterized by energy release rates depending on the crack positions and loading scenarios, as illustrated in Fig. 10. For example, in-plane crack opening mode due to tensile loading conditions is known as

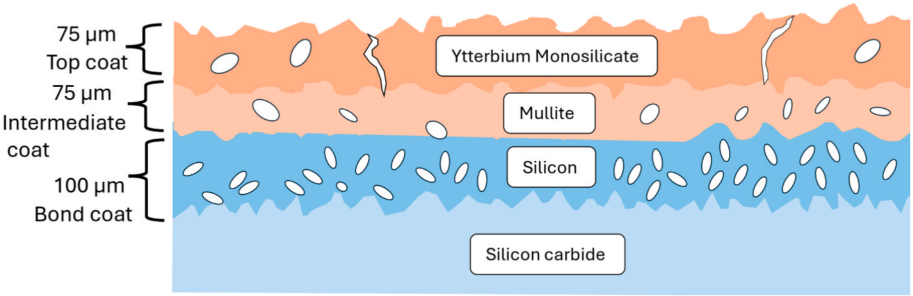

Fig. 2. Schematic illustration of an APS deposited tri-layer EBC structure (adopted from Ref. [26]).

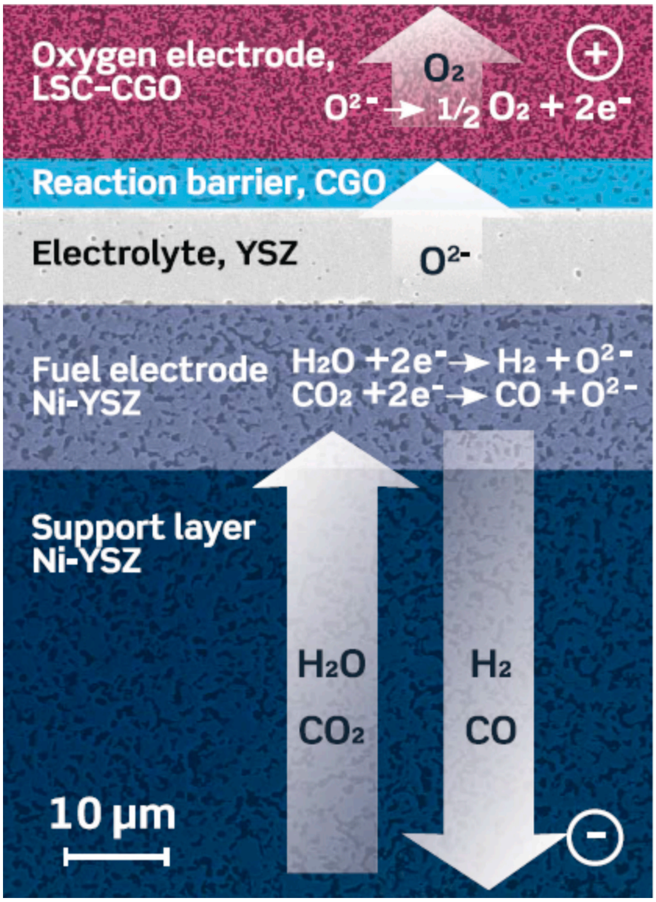

Fig. 3. Electron microscopy image of the active layers of an SOEC (color overlaid) and the electrochemical reactions occurring in the cell during H_2O and CO_2 electrolysis [27].

Mode I. Mode II is defined by in-plane shear loading conditions, whereas the out-of-plane shear loading conditions are known as Mode III failure mode.

As the coatings form a bi-material with the substrate, the fracture behavior will be a mixed-mode loading at the interface. A schematic of the interfacial toughness of the coating/substrate in terms of phase angle or mode mix (ψ) is presented in Fig. 11. The interface, whether weak or strong, is not only dependent on the elastic modulus of the coating and substrate, but also the fracture energy of the interface. To understand the interfacial fracture behavior in the coating/substrate interface, Hutchinson and Suo provided methodologies and analytical solutions [50] and further analytical solutions by Hutchinson and Hutchinson [51].

For the interfacial crack, the energy release rate G is dependent on the complex stress intensity factor (SIF) K^* [52,53], which is described in Equation 1.

$$G = \frac{(\overline{E}_1 + \overline{E}_2)}{2\cosh^2(\pi\cdot\varepsilon)\cdot\overline{E}_1\cdot\overline{E}_2}\cdot|K^*|^2 \tag{1}$$

where

$K^* = K_I + i\cdot K_{II}$, K_I is the mode I fracture toughness due to the normal loading on the crack tip and K_{II} is the mode II fracture toughness because of in plane shear loading at the crack tip.

ε is the elastic mismatch of the material 1 and material 2. This type of elastic mismatch for bimaterials is known as the Dundurs parameter [54]. ε is expressed as in Equation 2.

$$\varepsilon = \frac{1}{2\pi}\cdot\ln\left(\frac{\mu_1 + \mu_2\cdot\kappa_1}{\mu_2 + \mu_1\cdot\kappa_2}\right) \tag{2}$$

μ_j ($j = 1, 2$) denotes the shear modulus of each material.

$\kappa_j = 3 - 4\nu_j$ with ν_j being Poisson's ratio of the material for a plane strain problem, while

$\kappa_j = \frac{(3-\nu_j)}{(1+\nu_j)}$ for plane stress.

$\overline{E}_j = \frac{E_j}{\left(1-\nu_j^2\right)}$ for plane strain, while $\overline{E}_j = \overline{E}_j$ for plane stress.

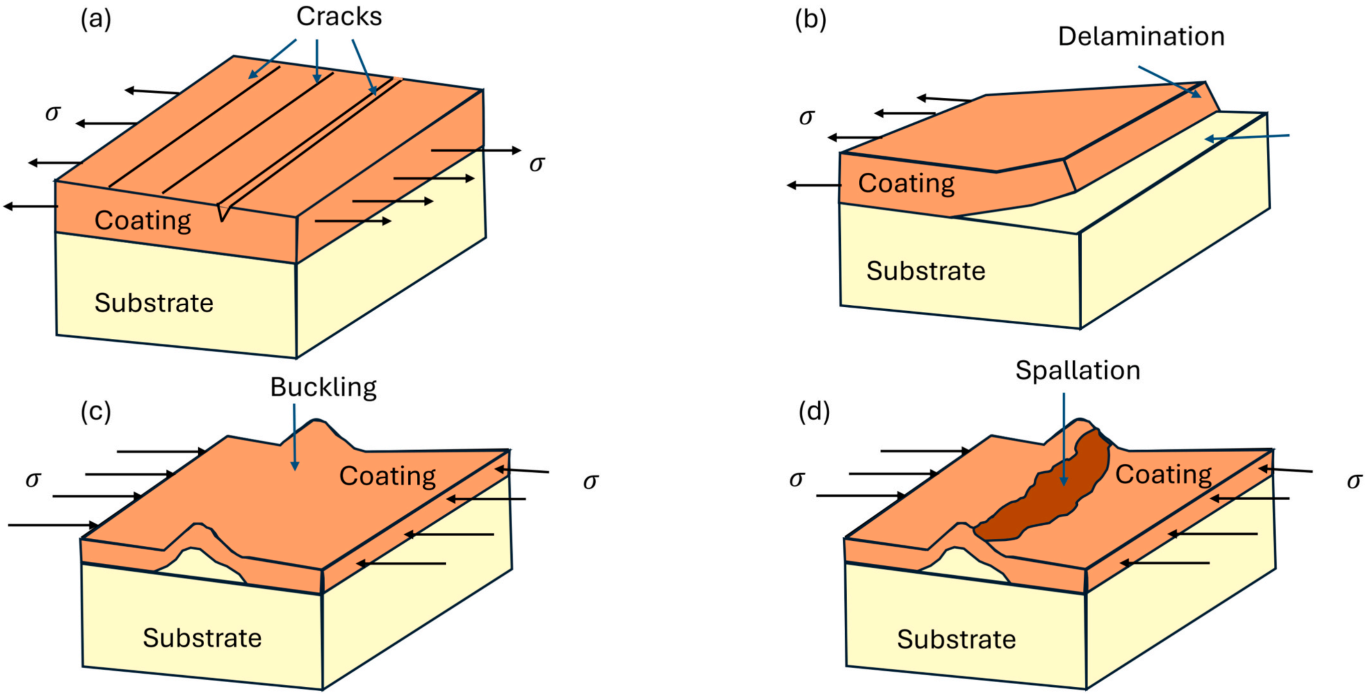

Fig. 4. Types of coating defects experienced in the pvd coating process: (a) cracks, (b) delamination, (c) buckling, and (d) spallation (adopted from Ref. [38]).

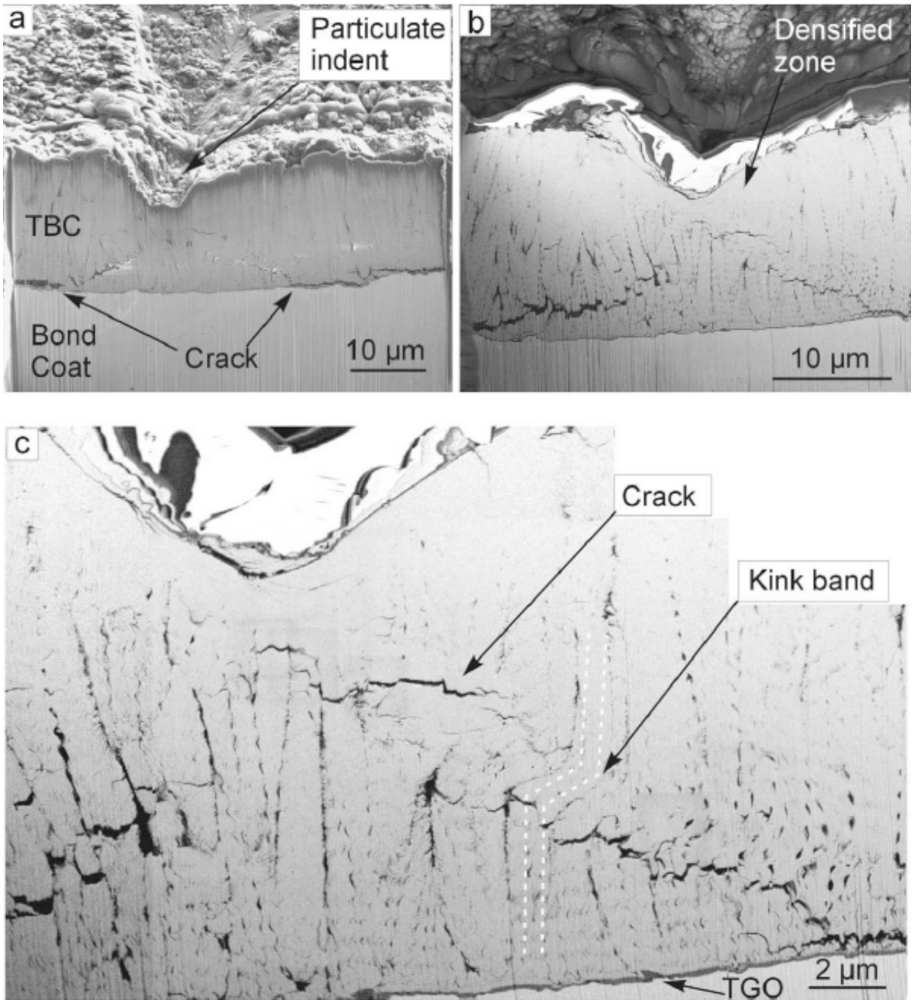

Fig. 5. A FIB cross-section reveals the impact damage by an individual particulate still embedded in the 7% YSZ TBC. A densified zone forms immediately underneath the impact site. Circumferential cracks are evident inside the densified zone as well as near the boundary between the TBC and the thermally growth oxide (TGO) layer. (a) Secondary electron (SE) image; (b) back scatter electron (BSE) image. (c) BSE image of the kink band and cracks. The section plane is at 38° to the electron beam [44].

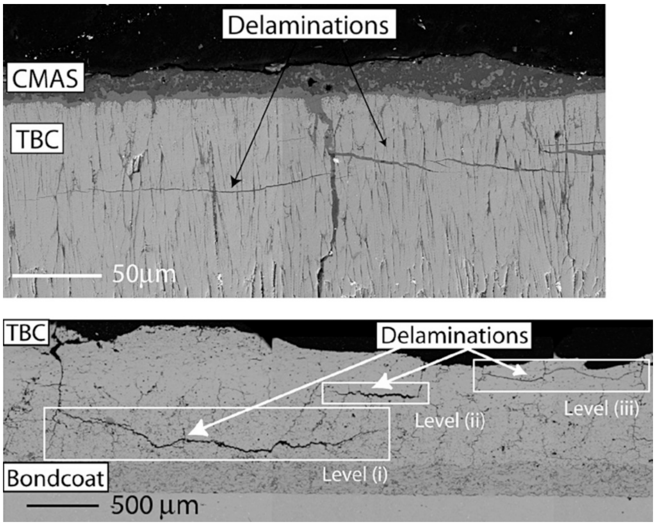

Fig. 6. Examples of delaminations in thermal barrier coatings obtained from components removed from engines subjected to CMAS penetration [46].

A schematic of the crack tip and the loading condition is illustrated in Fig. 12. As mentioned earlier, the mode mix or phase angle ψ is another parameter to classify the interfacial fracture toughness as well as the energy release rate, whether it is in mode I, mode II or mixed-mode I/II. This phase angle is expressed according to Ref. [50,52] in Equation 3.

$$\psi = \tan^{-1}\left(\frac{\mathrm{Im}\left(K^{*} l^{i\epsilon}\right)}{\mathrm{Re}\left(K^{*} l^{i\epsilon}\right)}\right) \tag{3}$$

where l is a reference length at remote distance, which is somewhat an arbitrary length parameter. The functions Im and Re are used to describe the imaginary and real components of the complex SIF, respectively.

From the above considerations, the elastic mismatch of the coating and substrate should be as low as possible to avoid delamination. The larger the elastic mismatch, the larger will be the delamination leading to the failure of the coatings. Thus, it is better to have an elastic modulus ratio of the coating and substrate close to 1. Furthermore, the CTE mismatch should be kept as low as possible to avoid cracking at the interface of the coating and substrate, which will trigger the delamination after hours of thermal cycles.

4. Test methods

In the previous section, various types of interfacial fracture modes

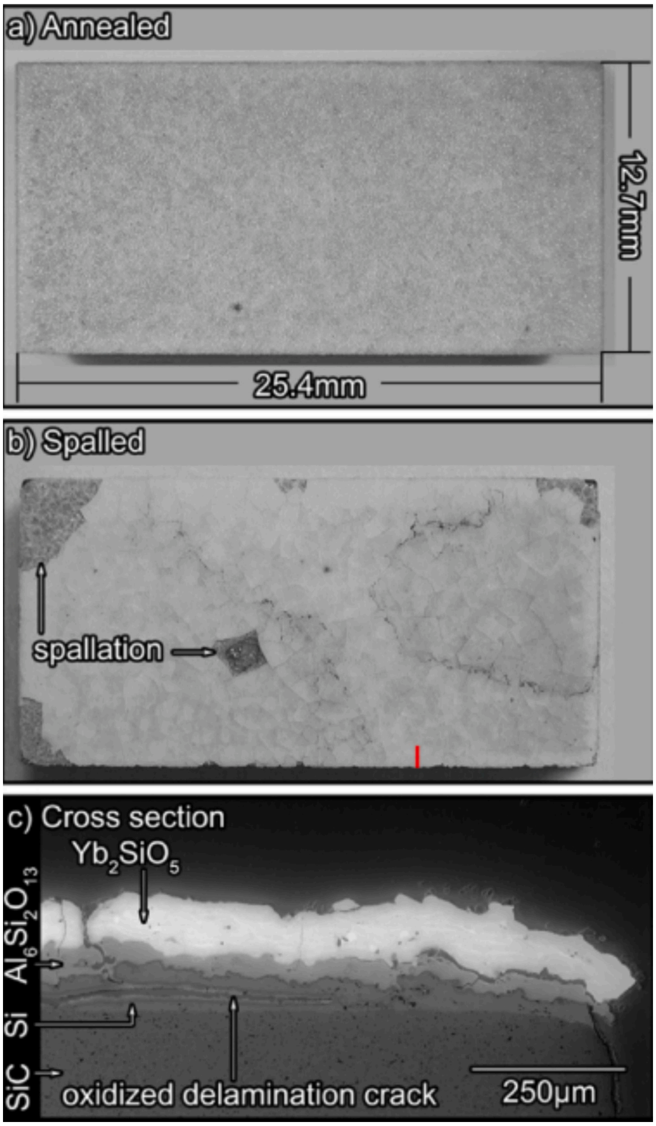

Fig. 7. (a) Shows an annealed tri-layer EBC deposited using low power plasma spray parameters. The same sample after 250 steam cycles at 1316 °C is imaged optically in (b) and its cross section near an edge in (c) using BSE mode SEM imaging. The red bar in (b) indicates the location of the section shown in (c) [22].

between coating and substrate were discussed. In this section, the criteria to perform interfacial fracture toughness are outlined. Furthermore, different types of interfacial fracture toughness tests are described along with advantages and disadvantages of individual test methods at room and elevated temperatures.

An overview diagram of adhesion testing is displayed in Fig. 13. To study the failure type and interfacial adhesion properties of coatings to a substrate, the test methodologies can be classified into two categories. One test category is based on strength, i.e. how is the bonding strength of the coating to the substrate, whereas the other testing method category is based on the interfacial fracture behavior, i.e. interfacial fracture toughness. Most common methods are the pull-off test [55], peel test [56], scratch test [57–60] and cross-cut tape test. However, for the quantitative analysis, except for the cross-cut tape test [61,62], the other mentioned methods are performed. Moreover, the pull-off test is less applicable for porous coatings as the glue penetrates through the coating and provides inappropriate information. Another limitation is that the device employed for this type of testing is limited to the bonding strength of the used adhesive. The interfacial fracture toughness is determined by double cantilever beam tests [63,64], wedge tests [65–67], indentation tests [68,69], bending tests [70,71] and so on.

To perform interfacial fracture toughness tests, specific criteria need to be satisfied. Without meeting those requirements, the tests should not be carried out. The conditions necessary for conducting the reliable interfacial toughness are as follows:

- *Test setup:* test setup and test protocol should be easy to follow. It means, the test setup should not contain too many test features or loading features. If the test setup has complex test features such digital image correlations (DIC), acoustic emissions (AE) and X-Ray imaging, it would be considered as complex and expensive.
- *Specimen preparation:* specimen manufacturing should be simple. It means specimen geometry should be kept simple. The fabrication of the specimen should not take a long time. But most of the fracture toughness tests require notched specimens. Creating a suitable sharp notch is challenging.
- *Fracture modes:* fracture modes such as mode I, mode II, mode III or mixed mode should be clearly defined before performing the test.
- *In-situ/ex-situ test:* whether the crack should be monitored during the test, it should be decided before conducting the test. Otherwise, postmortem or ex-situ of the crack measurement should be implemented. In-situ crack monitoring is regarded as a complicated procedure due to the necessity of a high-speed camera, AE method or carrying out the test in a scanning electron microscope (SEM) chamber.
- *Test conditions:* test conditions such as room and high temperature should be decided to perform the suitable interfacial fracture test. The high temperature interfacial facture toughness tests are difficult to perform due to the essence of extra test features such as muffle furnace, hot stage, thermo-couples, AE device or DIC systems.
- *Closed-form/analytical solutions:* the suitable test should provide direct closed-form solutions to calculate the interfacial fracture toughness or fracture energy. If numerical simulations are necessary, the test should be considered as less cost efficient.
- *Postprocessing:* postprocessing of the potential test should be easy. If a focused ion beam (FIB) milling is required to understand the failure mechanisms, it should be considered as a complicated and expensive test.

A test should be regarded as simple, when

- Test configuration does not contain too many loading features and heavy devices
- Simple specimen geometry and specimen manufacturing do not take longer time
- Ex-situ monitoring of the crack length
- Easy data acquisition and post processing

On the other hand, a test should be regarded as complex or challenging, when

- Test configuration has multiple loading and test features, heavy devices and highly calibrated devices such as DIC or AE technology
- Complex specimen geometry i.e. multiple notches and complex manufacturing of specimen i.e. FIB milling to fabricate specimen
- In-situ monitoring of the crack during testing by using a high-speed camera or a SEM
- Indirect data analysis and complex post processing such as requiring a numerical analysis for evaluating the interfacial fracture toughness

Based on the above-mentioned criteria the appropriate interfacial facture toughness should be performed. The next subsection describes the various types of interfacial fracture toughness tests performed at room temperature.

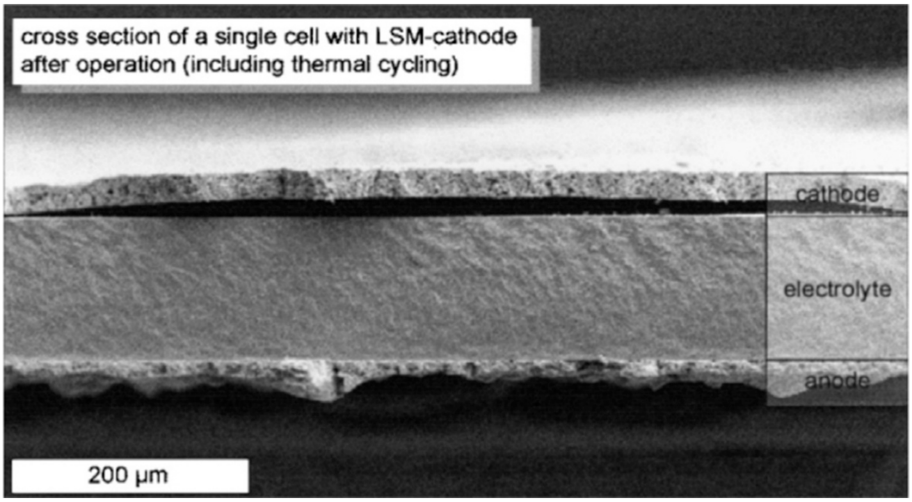

Fig. 8. Delamination occurred at the cathode in electrolyte supported solid oxide fuel cell (SOFC) [47].

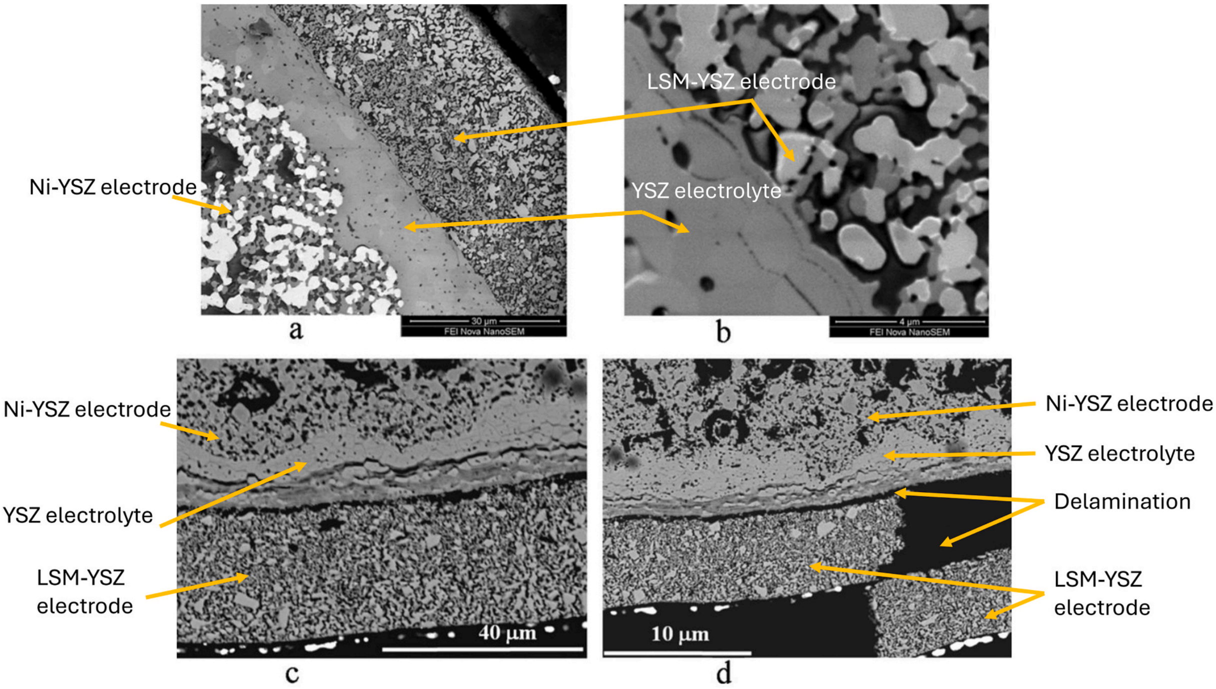

Fig. 9. SEM images showing (a) cell cross-section before testing, (b) degradation at YSZ grain boundaries, (c) cracking in the YSZ electrolyte and (d) delamination of the LSM-YSZ air electrode after electrolysis operation [48].

4.1. *Tests at room temperature*

In this subsection, the test methods which are conducted at room temperature are discussed by evaluating the methodologies, advantages, disadvantages as well as the application of the test methods.

4.1.1. *Double cantilever beam (DCB) test*

It is mentioned in section 3 that there are three types of interfacial fracture modes. Thus, this subsection reviews the double cantilever beam test including schematics and microstructures to estimate the mode I interfacial fracture toughness. Additionally, the merits and demerits of this test are also discussed.

The double cantilever beam (DCB) test is performed in laminated composite materials to determine the mode I fracture toughness [72–74]. The DCB test is carried out under uniaxial tensile loading conditions.

The schematics of the test configuration are illustrated in Fig. 14. The DCB method was adopted and applied to a double cantilever sandwich beam test setup to create pure bending moments and stable crack propagation. The bending moments and crack propagation were used to determine the fracture energy of the interface between dense lanthanum strontium chromite (LSC) and a porous lanthanum strontium manganite (LSM) [63]. For this test, the instrumentation was conducted according to Ref. [75]. The test fixture was mounted during use on an x-y-z stage at a door of the vacuum chamber of an environmental scanning electron microscope (ESEM). The fixture base was driven by a motor and the speed of the fixture was controlled through the software of the microscope. The applied load P, was measured by two strain gauge bonded onto a beam at one of the ends, and a self-temperature-compensation half-bridge Wheatstone bridge strain recorder was used. The load reading was calibrated by applying calibration weights. The opening displacement δ of the fixture was measured by a linear-variable

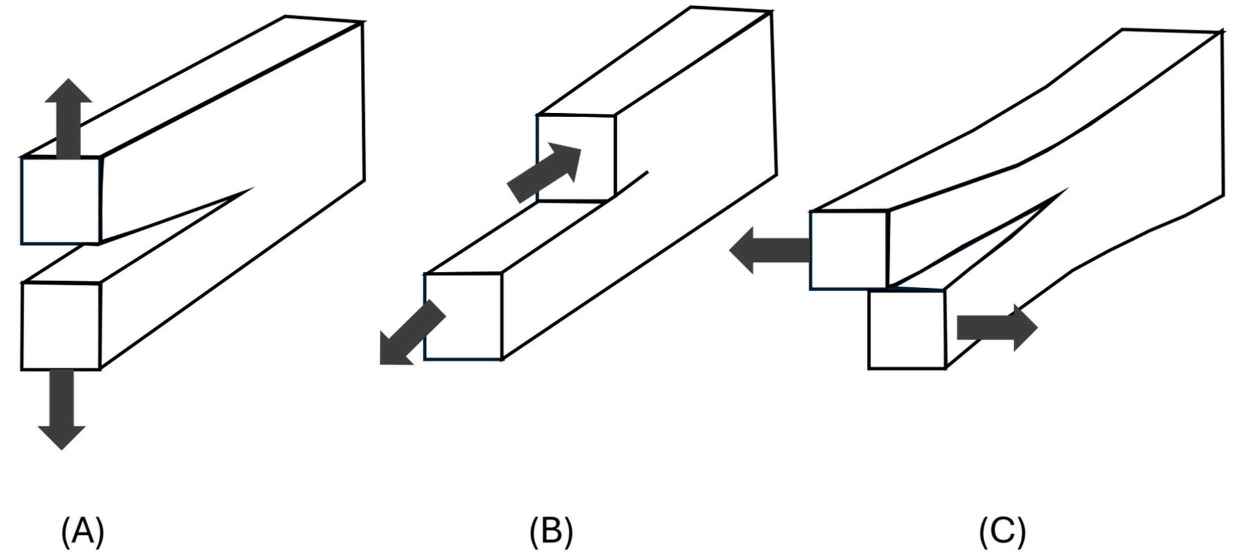

Fig. 10. The different failure modes. (A) Represents mode-I (tensile force), (B) represents mode-II (shear force) and (C) represents mode-III (torsional force) (adopted from Ref. [49]).

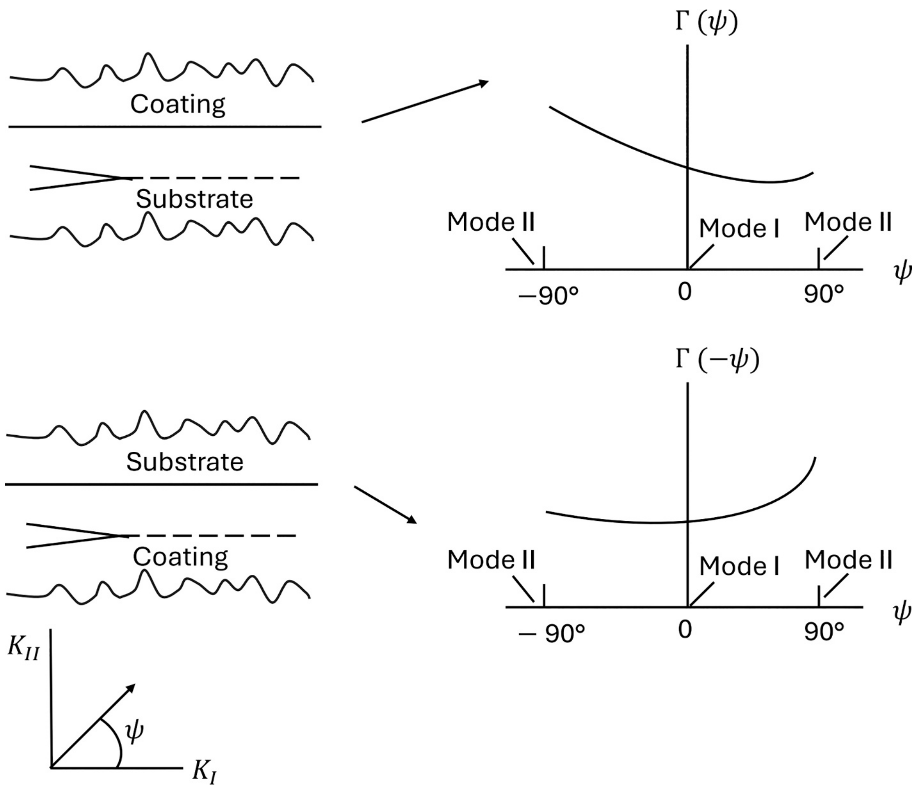

Fig. 11. Schematic of coating/substrate interface toughness as a function of mode mix (ψ) (adopted from Ref. [51]).

differential transducer (LVDT). Crack growth was monitored by acoustic emission (AE); an AE transducer was fixed to the uncracked end of the DCB specimen, and AE signals were collected through a preamplifier. The LSC two beams had a nominal geometry of $55 \times 5 \times 3\ \text{mm}^3$, whereas the thickness of the thin, porous LSM layer was between 20–50 μm.

The energy release rate was independent of the crack length in plane strain for the sandwiched specimen neglecting the residual stress. When the layer thickness t was sufficiently small with respect to the beam thickness H ($t \ll H$), the energy release rate was determined according to Ref. [76] by Equation 4,

$$G = 12\cdot\left(1-\nu_1^2\right)\cdot\left(\frac{M^2}{B^2\cdot H^3\cdot E_1}\right) \tag{4}$$

where G is the energy release rate, B is the width of the beams, H is the beam thickness, E_1 and ν_1 are the Young's modulus and Poisson's ratio of the beams, respectively.

This double cantilever beam (DCB) configuration was further implemented to assess the fracture properties of anode materials (NiO-YSZ) in fuel cells, see Fig. 15 [64]. The reported porosity of the anode materials was 15 %. The crack initiation path and crack opening inside

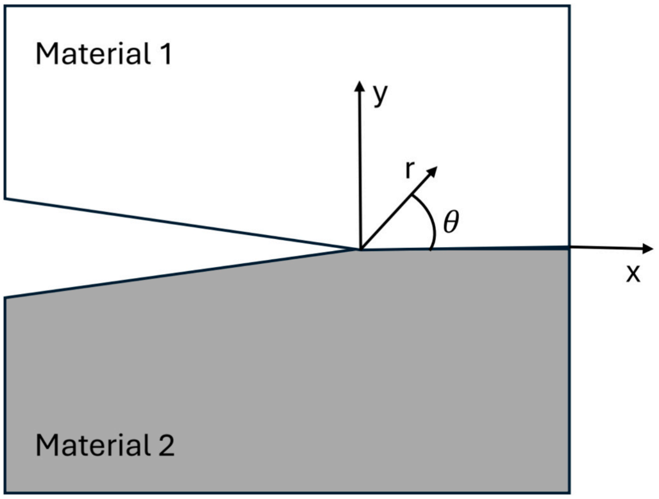

Fig. 12. An interfacial crack between two dissimilar materials (adopted from Ref. [29]).

the ESEM is shown in Fig. 16 and Fig. 17. To implement the configuration, a slight modification was conducted by using steel beams as grippers for the thin anode materials so that the loads can be applied. Due to the introduction of steel as grippers or stiffeners, an equivalent analytical formula for the moment of inertia depending on the geometrical and elastic properties was established.

The key benefit of the DCB test method is that stable crack growth is attained under rotation control. An additional advantage is that crack growth resistance is measured from the sharp crack. Moreover, the crack length is independent of the energy release rate, which is based on only moments. The drawbacks of this test method are that a special test fixture is necessary for creating the bending moments and ESEM is employed to monitor the cracks. Subsequently, the specimen manufacturing is difficult because of a sharp notch. Furthermore, the test procedure is time consuming due to the complexity of test fixture and the startup at the ESEM.

The applicability of this method is basically for thick coatings as creating a pre-crack in thin coatings is very challenging [28]. But this double cantilever beam test was successfully carried out with a razor blade to thin multilayered oxide coatings on glass, each coating had a thickness of less than 50 nm [77–79]. The interfacial fracture toughness was calculated from the simplified adoption of an augmented beam theory model according to Ref. [78], which is expressed in Equation 5.

$$G = \frac{3\cdot E\cdot h^3\cdot \delta^2}{16\cdot (L+0.6\cdot h)^4} \tag{5}$$

where δ is the crack opening length, L is the crack length, E and h are the beam elastic modulus and thickness respectively and G is the energy release rate.

The main advantage of this double cantilever beam test is that it does not require any force data to calculate the energy release rate. It is basically based on the crack tip position and crack propagation length. Although the method is suitable for thin coatings, the in-situ crack propagation and monitoring of the crack length is very challenging for opaque substrates as this method was conducted only on glass substrates [77].

4.1.2. Wedge test

Apart from the DCB test, another test method is applied for determining the mode I fracture toughness where a wedge is inserted into the notched DCB specimen. This wedge insertion method was used to determine the mode I[80] and mixed-mode I/II [81] in laminated composites or with a razor blade to find the mixed-mode I/II fracture toughness in bi-materials [82,83]. This subsection describes the different types of wedge test methods such as wedge impression, wedge loaded asymmetric DCB and single wedge cantilever beam for evaluating the interfacial fracture toughness in electrolyte electrode materials, TBCs and EBCs at room temperature. Further, it includes schematics and microstructure to determine the interfacial fracture toughness. Moreover, the benefits and drawbacks are also discussed.

Although the wedge inserted DCB test is implemented for mode I interfacial fracture toughness, the very first wedge test was introduced for TBCs to determine the mode II interfacial fracture toughness, as

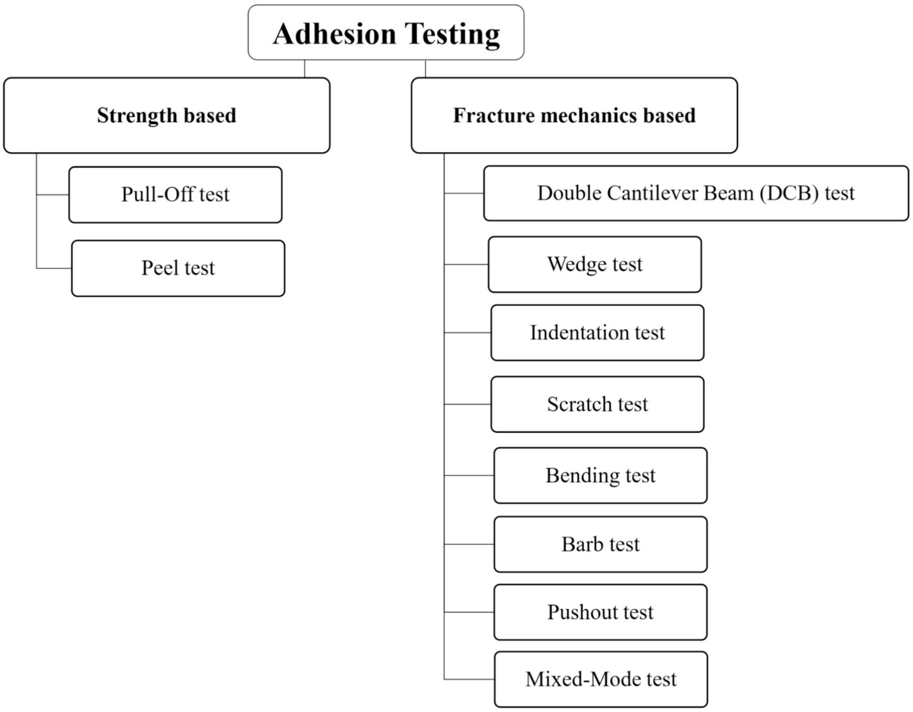

Fig. 13. Overview of adhesion test methods of coatings on substrates.

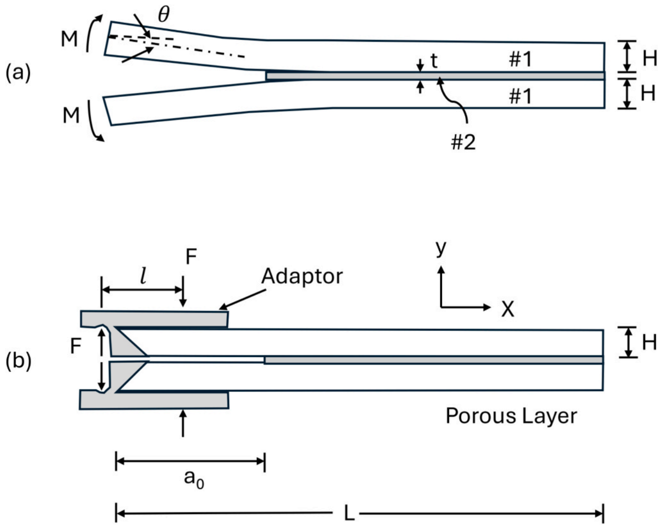

Fig. 14. (a) Geometry and loading of a DCB specimen loaded with pure bending moments. (b) The pure bending moments are created by loading each beam with two forces F of equal magnitude separated by a distance l (adopted from Ref. [63]).

presented in Fig. 18. In that study, the interfacial adhesion between films/coatings and ductile substrates was determined [84,85]. Furthermore, the remnant toughness and the delamination characteristics of thermal barrier coatings (TBCs) after extended thermal exposure was evaluated by a wedge impression. The employed wedge in that experiment was a highly polished WC material with a wedge angle of 90°. To perform the experiments, a matched pair of linear voltage differential transducers (LVDTs) was employed to accurately measure the displacements during testing. The LVDTs were located on opposite sides at equal distances from the impression.

In that study, the TBC was comprised of a thin layer of $Al_2O_3 \approx 3$ μm in thickness and a thick layer of compliant $ZrO_2 \approx 100$ μm in thickness and a 3000 μm thick substrate. An analytical solution to calculate the energy release rate and interfacial fracture toughness of multi-layered coating systems was proposed, which is expressed in Equation 6,

$$G = \frac{1}{2}\cdot\frac{P^2}{E_e^{'}\cdot h_e} + 6\cdot\frac{M^2}{E_e^{'}\cdot h_e^3} \tag{6}$$

where P is the net force acting on the layer before decohesion, and M is the net moment referenced to the neutral axis of the layer, again before decohesion, $E_e^{'}$ is the effective plane-strain modulus of the coatings and h_e is the effective thickness of coatings.

h_e represents the thickness of the bilayer as the single layer, which is presented by Equation 7,

$$h_e \equiv \sqrt{\frac{-M\Delta\varepsilon}{P\Delta\kappa}} \tag{7}$$

where $\Delta\varepsilon$ is the strain change at the neutral axis and $\Delta\kappa$ is the curvature change of the released layer. The parameters P and M can be calculated from the measured residual strains. The detailed expressions to find the values of $\Delta\varepsilon$ and $\Delta\kappa$ as well as to evaluate the interfacial fracture toughness are described in Ref. [84]. The limitation of Equation 6 is that it requires numerical simulation to determine the surface strains to calculate the net force P. Another limitation is that the delamination length should not exceed the wedge length for accurate results.

The key benefits of the wedge impression test are that the test setup is less complicated, and a closed form analytical solution is available for the calculation of the interfacial toughness. Additionally, more area is tested at the interface to evaluate the delamination. Further advantages are that the plain-strain conditions eliminate the tensile stresses parallel to the delamination crack front and the in-situ crack growth is observed by utilizing the plane surface of the wedge. The notable downside of this test method is the necessity of the accurate measurement of the residual strain. Further limitation is that the test requires a ductile and flexible substrate for substantial plastic deformations to initiate crack growth.

Another variant of the wedge test was developed for thermal barrier

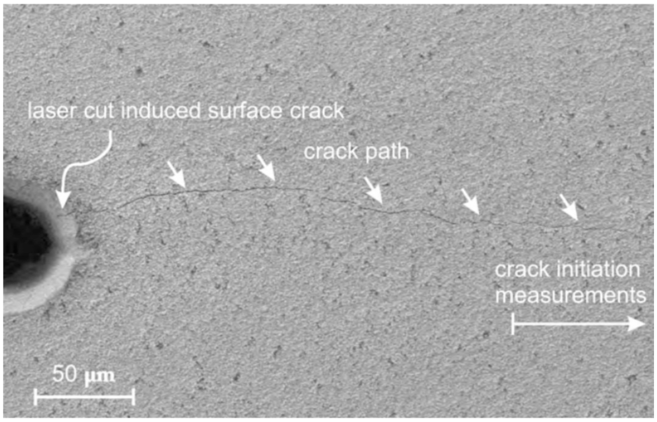

Fig. 16. SEM micrograph of crack propagation [64].

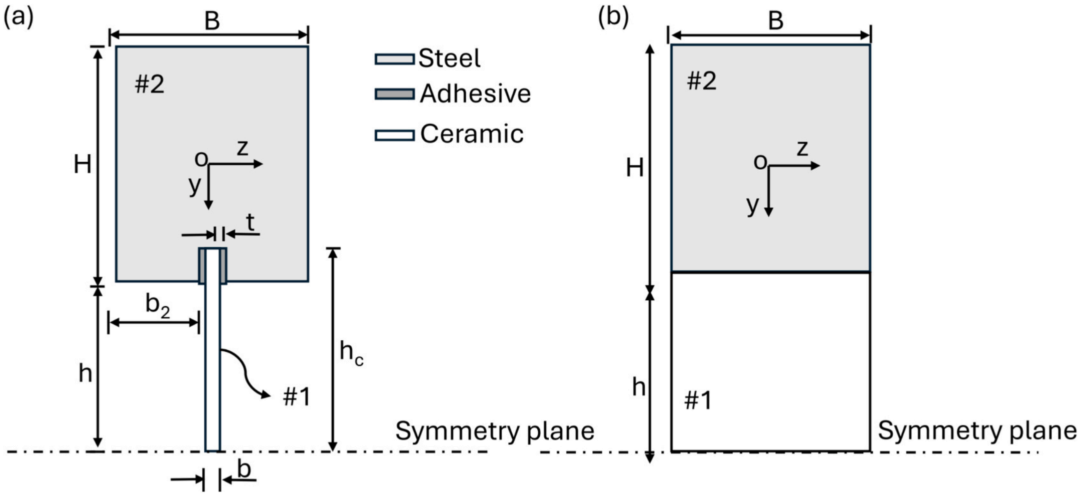

Fig. 15. Symmetric half specimen (a) cross-section, and (b) equivalent cross-section (adopted from Ref. [64]).

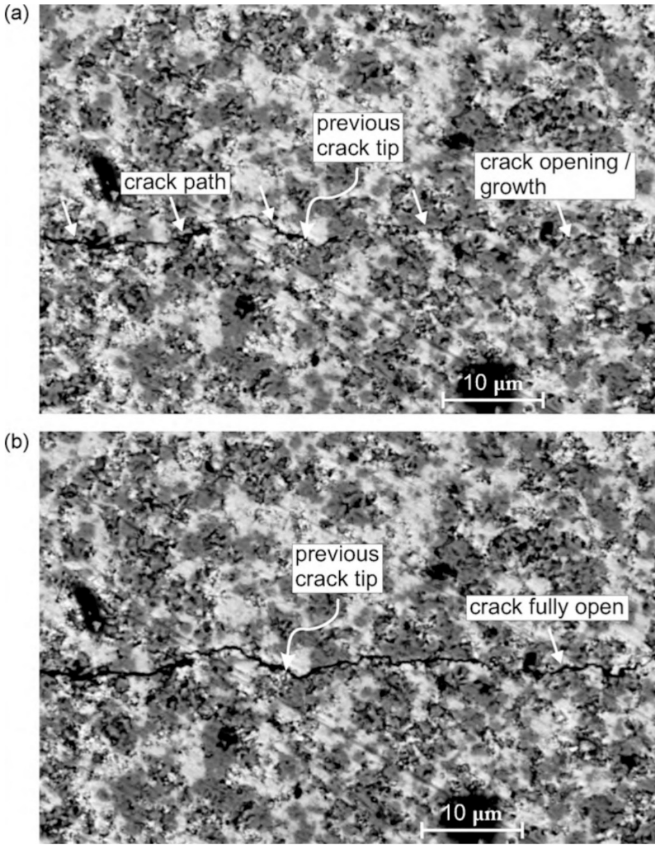

Fig. 17. Backscatter electron micrographs showing the crack opening and path with increasing applied *G*. Darker gray is YSZ, lighter gray is NiO and black areas are porosity [64].

and environmental barrier coating systems, where the wedge is inserted into a notched asymmetric double cantilever beam (ADCB) specimen. This wedge test is carried out to investigate the evolution of interface fracture toughness with thermal exposure treatment by wedge indentation [67]. The data reduction scheme is based on Ref. [86] and the compliance is determined for the coating according to Ref. [87].

The total interfacial fracture toughness between the coating and substrate was determined in terms of critical energy release rate from Equation 8,

$$G = \frac{q\cdot n\cdot F_c^2\cdot d^{n-1}}{2\cdot W} \tag{8}$$

where G is the mode I fracture toughness between the coating and the substrate, q and n are fitting parameters, F_c is the critical load for the crack initiation, d is the pre-crack length inside the specimen and W is the specimen width.

This wedge test was implemented for multilayered environmental barrier coatings, which were characterized by laser textured silicon bond coats to determine the interlaminar fracture toughness [66]. In that study, the tested SiC/SiCN substrates had dimensions of 100 × 40 × 2 mm^3. The applied metallic wedge-shaped tool was 0.5 mm thick with a wedge angle 2θ of 17.6°.

The schematic of this test configuration is illustrated in Fig. 19. This test configuration was first introduced to propose a model to calculate the interface fracture test for ceramic environmental barrier coating (EBC) on ceramic matrix composite (CMC) [65]. The installed test facilities were a motorized stage to move the specimen, a load cell of 50 N, laser displacement measure technique to monitor the coating displacement and a light microscope to record and determine the exact time of the formation of crack.

The interfacial fracture toughness was calculated from this analytical formulation,

$$G = \frac{3\cdot A\cdot P\cdot \delta}{2\cdot b\cdot L} \tag{9}$$

where G is the interfacial fracture toughness, A is the conversion factor between the wedge load and the critical bending load, P is the measured wedge load, δ is the notch displacement calculated from bending force and equivalent bending stiffness, b is the specimen width and L is the measured length of the notch. The total data reduction technique is described in Ref. [66].

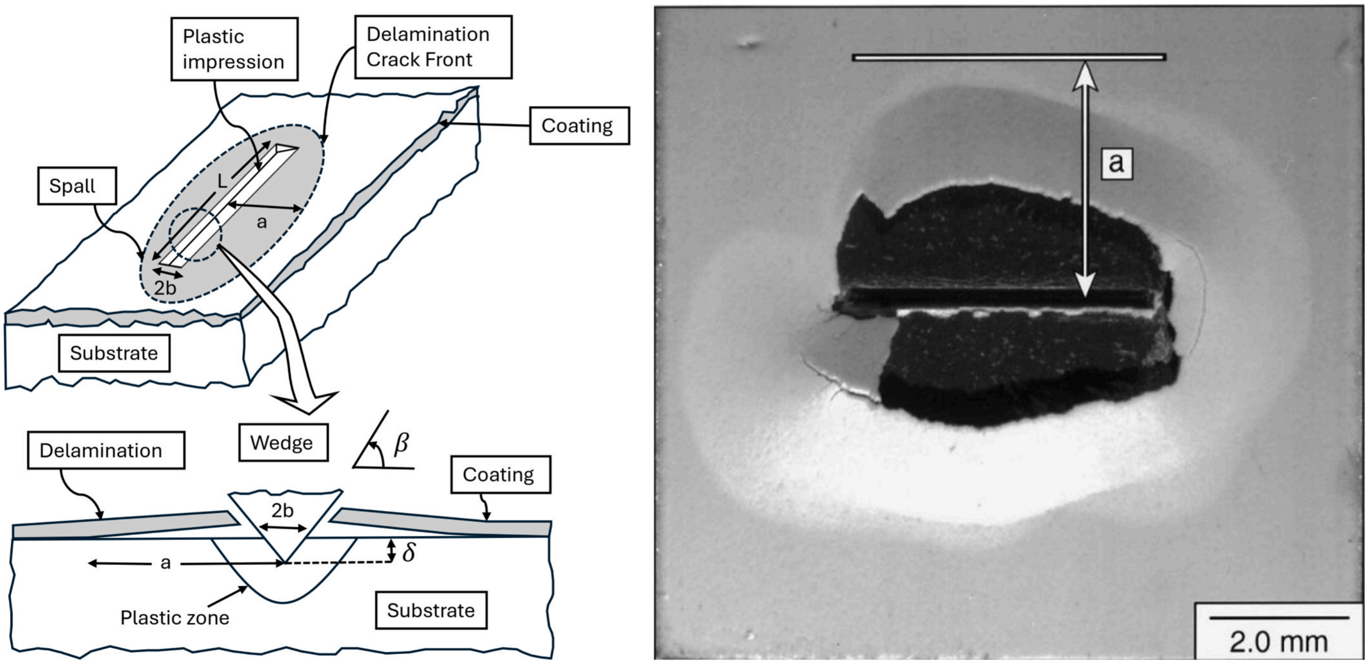

Fig. 18. Schematic diagram of the wedge or cone impression test (left) (adopted from Ref. [85]), typical optical image of an impressed TBC system. The impression area of the wedge appears as a solid dark line. The delamination distance is approximately 25 times the impression size of 30 μm [84].

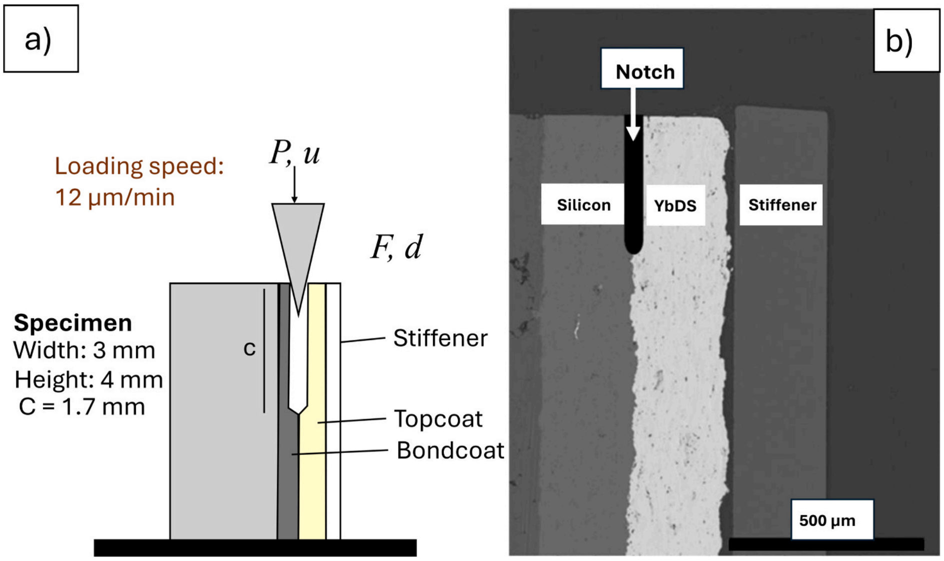

Fig. 19. (a) Draft of the original test setup (adopted from Ref. [66]) and (b) a SEM picture of a prepared sample for the interface toughness test [66].

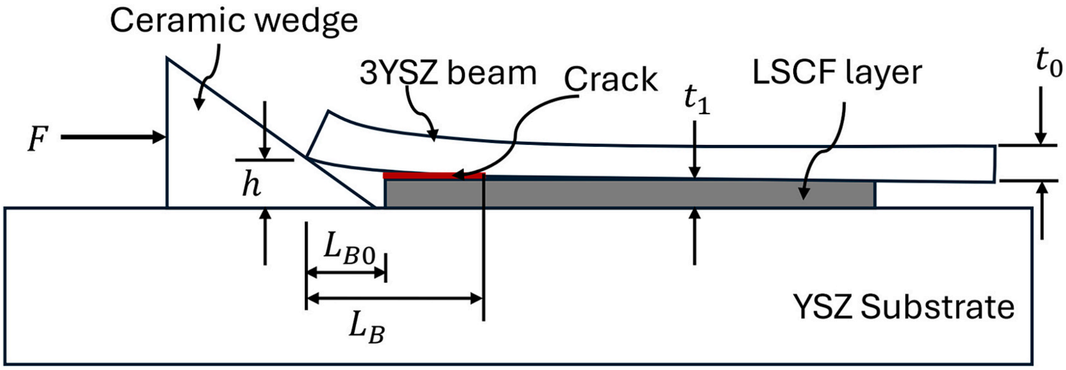

Fig. 20. A schematic of single beam wedge test (adopted from Ref. [88]).

The strengths of this configuration are that it provides the facility to determine the fracture toughness of the desired layer, the crack propagation of this test setup can be monitored with a digital image correlation (DIC) technique as well as with a high-speed camera. The key weakness of the wedge DCB test is that the test setup is complicated because of requiring a specialized motorized stage. Another drawback is the fabrication of the specimen which requires a sharp notch to initiate the crack. Further weakness is the consideration of friction effect due to employing the wedge.

Another variant of the wedge test was introduced for the electrolyte and electrode materials in solid oxide cells. The test configuration was proposed to determine the interlayer fracture toughness of sandwich specimen using a ceramic wedge, where porous $La_{0.6}Sr_{0.4}Co_{0.2}Fe_{0.8}O_3$ (LSCF) was acted as an adhesive to bond the thin (0.15 or 0.3 mm thick) tetragonal zirconia beam with a dense 3YSZ substrate [88].

The proposed geometrical configuration is depicted in Fig. 20. As the thin tetragonal zirconia beam was the movable beam [88], this configuration is known as single wedge cantilever beam. The wedge penetrated between the two zirconia (YSZ) adherents to create a crack inside the LSCF layer and to generate stable crack propagation so that the released strain energy can be measured. In that study, the specimens of thin 3YSZ beams having dimensions of $50 \times 5 \times 0.3$ mm^3 or $50 \times 5 \times 0.15$ mm^3 were joined to 10 mm thickness of thick 3YSZ substrates using a porous LSCF film as the adhesive. A thin porous solid layer (t_1) with a thickness of 10–30 μm of LSCF was achieved after the drying and firing process. The ceramic wedge of 3YSZ sliding on the YSZ substrate had a tip angle of 30°. The main facility for the conduction of the test was the advancing wedge with approximately 0.1 mm each step.

The energy release rate in the thin and bent YSZ beam was determined in terms of the crack propagation which is the changing length of the thin YSZ beam. Thus, the stored energy of the deflected cantilever beam for a point load is defined in Equation 10,

$$U = \frac{3EIh^2}{2L_B^3} \tag{10}$$

where E is the Young's modulus of the beam,L_B is the cantilever beam length, h is the deflection of the cantilever beam, and I is second moment of inertia, and $I = \frac{bt_0^3}{12}$, with b is the width of the beam and t_0 is thickness of the beam. L_B needs to be measured as it works as the driving force for the fracture energy of the bonding joint with the advancement of the wedge.

As the wedge gradually moves, the crack propagates inside the LSCF layer. Thus, in a stable condition, an increment in $h(\delta h)$ leads to an increment of stored energy (δU), which can be released by an increment of the cantilever length δL_B.

The critical energy release rate or the fracture toughness G for the propagated crack along the LSCF bonded layer can be evaluated by Equation 11,

$$G = -\frac{1}{b}\frac{dU}{dL_B} = \frac{9EIh^2}{2bL_B^4} \tag{11}$$

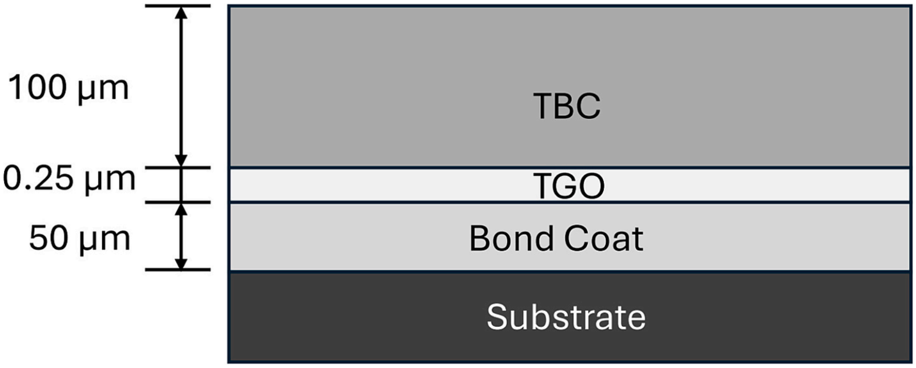

Fig. 21. Diagram of the EBPVD TBC System (adopted from Ref. [89]).

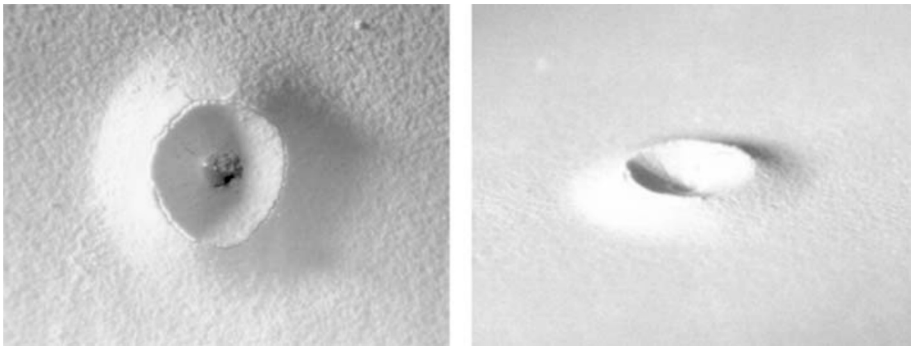

Fig. 22. Debonding in EBPVD TBC system due to indentation top and side view [89].

The notable advantages of this test setup are that it is relatively easy to perform, no force data is necessary, and no in-situ high resolution microscopy is required for an accurate position of crack tip. However, the significant disadvantage of this test method is that a numerical simulation is necessary to know the exact stress distribution at the interface. Furthermore, homogeneous, isotropic and linear elastic materials are assumed to conduct the simulation. But the LSCF material at the interface is a porous and nonlinear material in nature.

4.1.3. Indentation test

Another test method to determine the interfacial fracture toughness in coating to substrate system is the indentation test. Different types of indentation tests such as Rock well indentation, Vickers indentation and nanoindentations are performed to determine the interfacial fracture toughness. In this subsection these types of indentation tests along with schematics, test setups, microstructures, advantages and disadvantages are described and discussed.

For the coated systems, the indentation technique has been in use for several decades. The indentation method was implemented to measure the mixed-mode I/II interfacial fracture toughness in thermal barrier coating (TBC) systems [89]. The thickness of the coatings is illustrated in Fig. 21 and the debonding from indentation in EBPVD TBC system is displayed in Fig. 22. In this test configuration, the studied material was a TBC system of electron beam physical vapor deposition (EBPVD) coatings, basically yttria stabilized zirconia (YSZ) bonded on the bond coat of platinum-aluminide, a TGO layer of alumina and nickel super-alloy substrate. In that study, the experiments were performed with a standard Rockwell hardness tester with a brale C indenter. Two models were proposed for the analysis of interfacial toughness. One model was the large substrate model, and another model was the TBC specimen-sized model. The tested geometry of the substrate was 12.7 mm in radius and 3.18 mm in depth.

The energy release rate due to delamination was calculated from Equation 12,

$$\frac{2\cdot G\cdot(1-\nu^2)}{E_{eff}\cdot(t_{TGO}+t_{TBC})}=\left\{\varepsilon_r+\nu\cdot\varepsilon_\theta-\frac{(1-\nu^2)\cdot\varepsilon_\theta\cdot\left[1-\left(\frac{R_i}{R}\right)^2\right]}{(1-\nu)+(1+\nu)\cdot\left(\frac{R_i}{R}\right)^2}\right\}^2 \tag{12}$$

where G is the energy release rate due to delamination, ν is the Poisson's ratio of TGO and TBC layer due to no mismatch, E_{eff} is the effective Young's modulus for the biaxial residual stress in TBC/TGO layer, t_{TGO} and t_{TBC} are thicknesses of TGO and TBC layer respectively, ε_r and ε_θ are total radial strain and circumferential strain respectively, R is the outer radius of the axisymmetric debonding and R_i is the breaking radius of the debonded coating.

The interfacial stress intensity factor was determined according to Equation 13.

$$K=\sqrt{\frac{G\cdot\overline{E}_{TGO}\cdot(1-\alpha)}{1-\beta^2}} \tag{13}$$

where K is the mixed mode stress intensity factor, $\overline{E}_{TGO}$ is the Young's modulus of the TGO layer in plane strain condition, and α and β are Dundurs elastic mismatch parameters of the TGO layer and the bond coat [89].

Apart from the Rockwell indentation testing method, another indentation method equipped with a pyramidal Vickers indenter was carried out to measure the interfacial fracture toughness, see Fig. 23. In this configuration, the interfacial fracture toughness was estimated between the air plasma sprayed bond coat and substrate of thermal barrier coatings exposed to 1,050 °C at exposure times of 0 h, 10 h, 30 h and 100 h [90]. In that study, the tested thermal barrier coating was NiCrAlY bond coat and the directionally solidified super-alloy DZ40M. The thickness of the bond coat of the samples was about 120 µm. A micro-

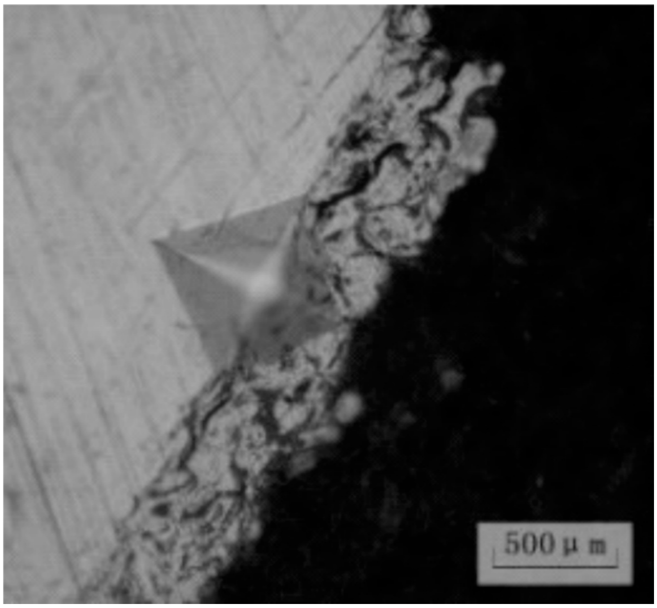

Fig. 23. Indentation at the interface of bond coat and substrate [90].

hardness tester was applied to perform the interfacial fracture test.

The apparent interfacial fracture toughness was calculated according to Equation 14 proposed in Ref. [91],

$$K = 0.015 \cdot \left(\frac{P}{C^{3/2}}\right) \cdot \left(\frac{E}{H}\right)_I^{1/2} \tag{14}$$

where K is the apparent interfacial fracture toughness, P is the force at which crack is generated and C is the crack length and $\left(\frac{E}{H}\right)_I$ is the ratio of elastic modulus and hardness at the interface.

In another study, dynamic loading instead of static loading was applied to calculate the interfacial toughness in thermal barrier coatings for hard and medium hard substrates by a Rockwell hardness tester [92]. Furthermore, similar Rockwell indentation tests were carried out to understand the cracks and delamination behavior at various indentation loads, crack lengths and thermal aging times in thermal barrier coatings [93]. The schematics and microstructures from this test configuration are illustrated in Fig. 24 and Fig. 25. The tested specimens were the substrate of isotropic IN 625 which had a thickness of 4 mm, 100 mm in length and 10 mm in width, with a 100 μm NiCoCrAlY metallic bond coat by EB-PVD and a ceramic coat of partially yttria stabilized zirconia (YSZ) with a thickness of 280 μm. In that study, the porosity of the TGO layer as well as the interface strength or fracture were not reported, only the failure mechanism was investigated.

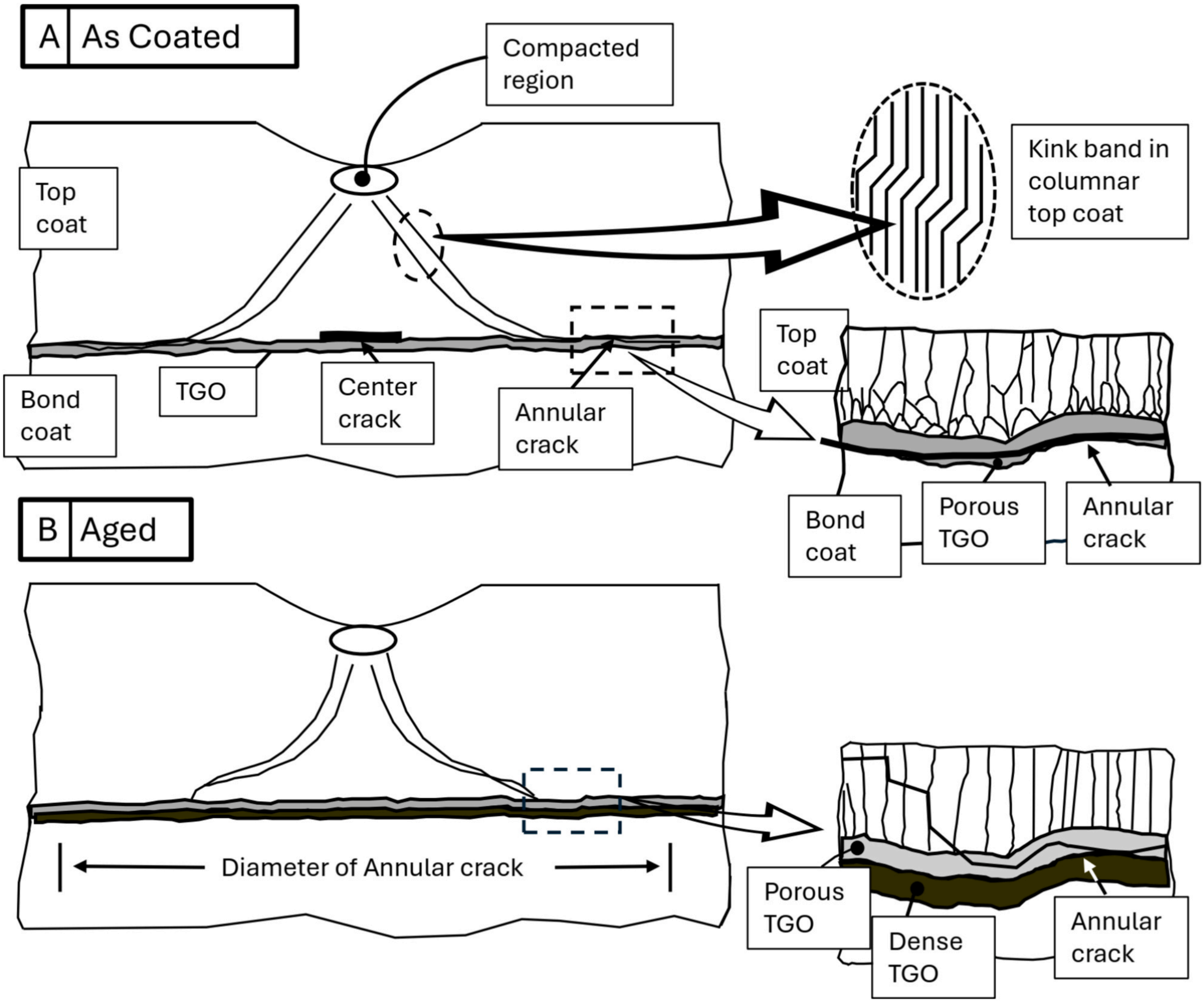

Fig. 24. Schematics summarizing the main crack patterns observed in: (A) as-coated and (B) thermally aged specimens (adopted from Ref. [93]).

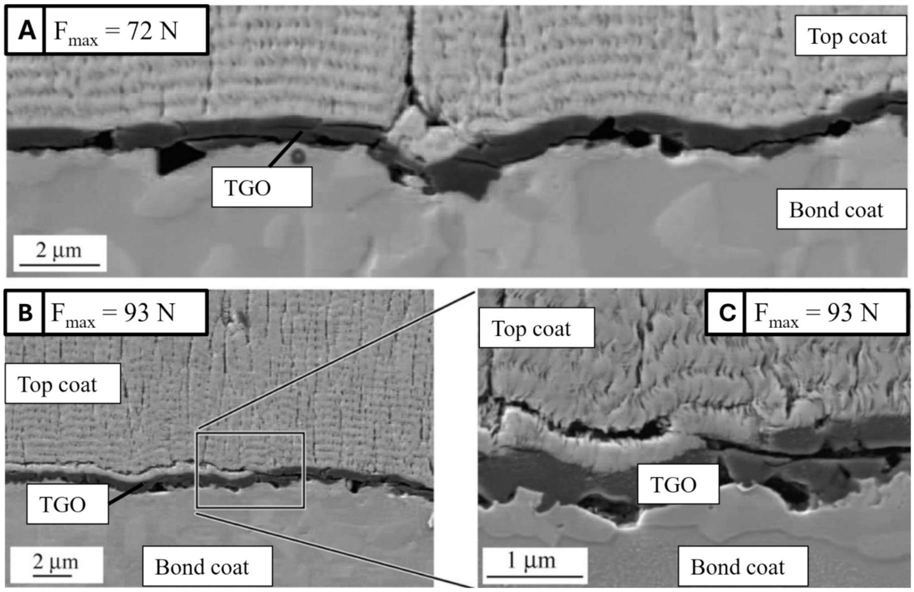

Fig. 25. Crack paths observed in as-coated specimens: (A) crack propagation along the interface between bond coat and TGO facilitated by pores and within the TGO; (B, C) crack propagation within the topcoat between sublayers and change of crack path into the TGO [93].

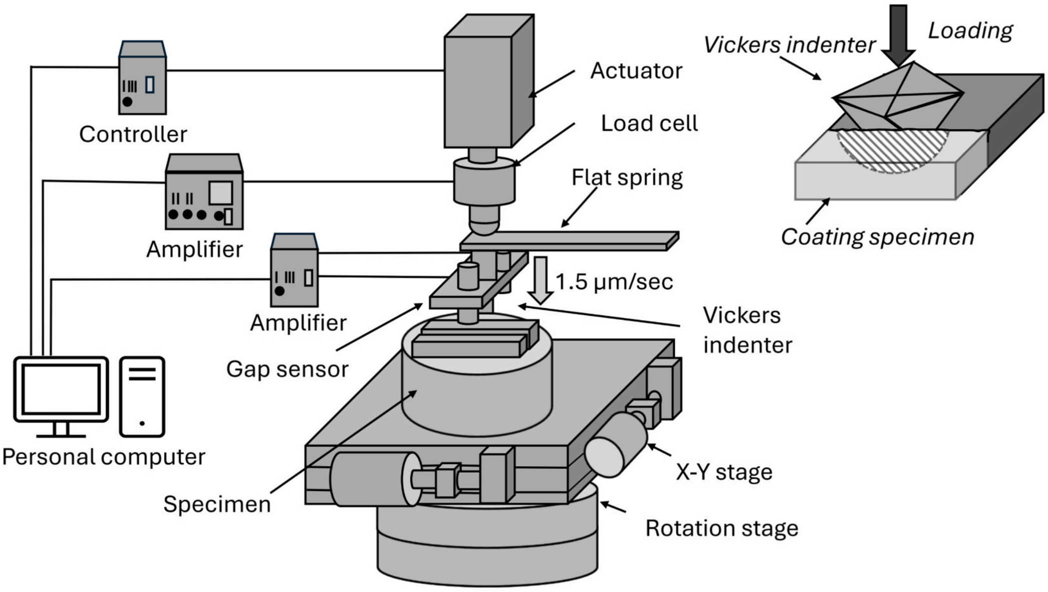

Fig. 26. Schematic of the instrumental indentation test (adopted from Ref. [94]).

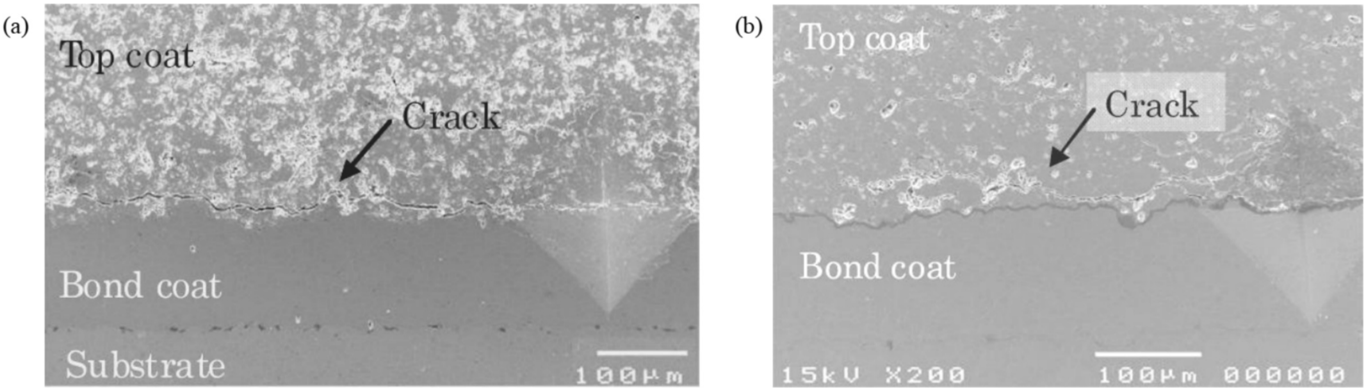

Fig. 27. Typical interfacial cracks initiated by indentation; (a) 0 thermal cycles (as sprayed), (b) after 500 cycles [94].

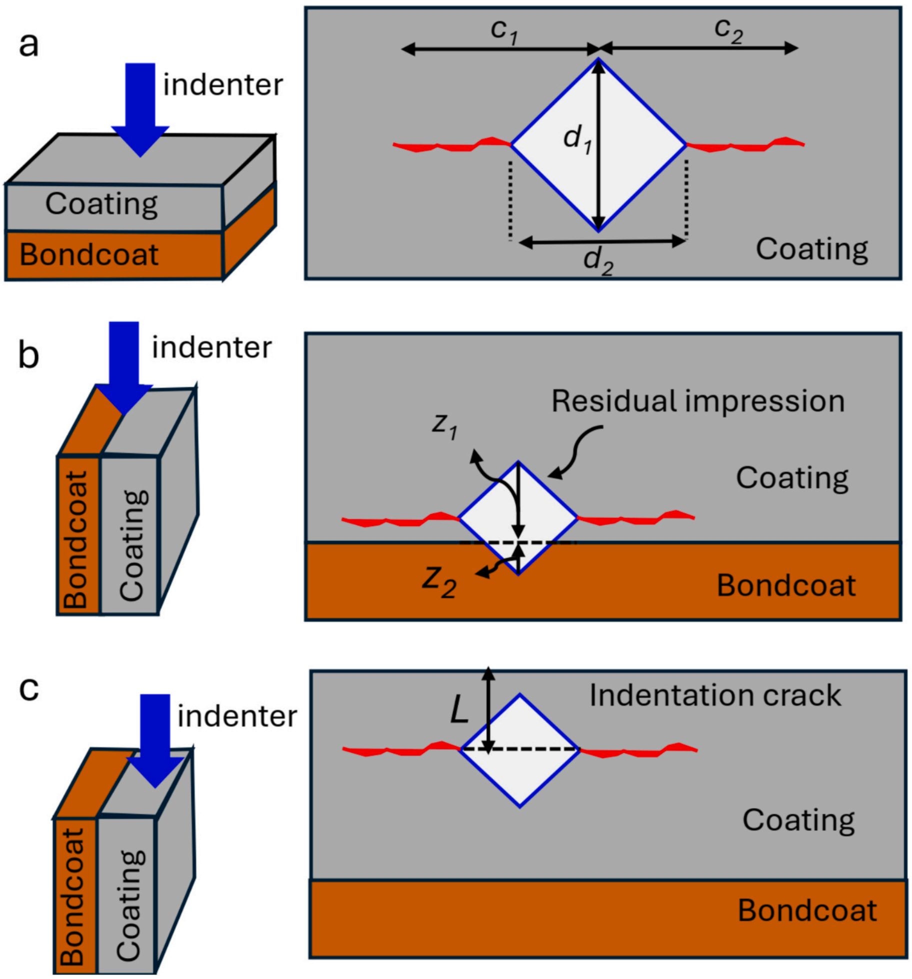

Fig. 28. Schematics of three kinds of Vickers indentations on the top surface (a), near the interface region (b), and on the lateral region (c) (adopted from Ref. [68]).

Afterwards, a new indentation method was introduced to assess the interfacial strength of thermal barrier coatings at the coating and the substrate interface, as presented in Fig. 26 and Fig. 27 [94,95]. The method is known as instrumental indentation test. In those studies, the tested materials were exposed to thermal cyclic fatigue and retired TBC vanes. The investigated TBC system was comprised of a 5 mm thick substrate of a Ni-base super-alloy, a 500 μm thick topcoat of yttria partially stabilized zirconia and a 100 μm thick bond coat of CoNiCrAlY alloy. The geometry of the specimens was 30 × 10 × 5.6 mm^3. The employed test facilities were computer controlled electric actuators for applying the load, a load cell and gap sensors for measuring the indentation load and the indentation depth, respectively. For the implementation of the test, the speed during indentation was 1.5 μm/s and the indentation load was held at the maximum value for 10 s. After the indentation test, the crack length and the diagonal length were measured from the SEM micrographs.

The apparent interfacial fracture toughness for the TBC coatings was calculated from Equation 15.

$$K = \left\{\xi_1 + \xi_2\left(\frac{c}{a}\right)\right\}\cdot\left(\frac{a}{c^{\frac{3}{2}}}\right)\cdot\sqrt{P\cdot E_I} \tag{15}$$

where E_I is the apparent Young’s modulus of the interface and a is the half diagonal length of the impression.

Later on, a modified version of the Vickers indentation method was developed to determine the micro-hardness, fracture toughness and residual stress of an air plasma-sprayed (APS) TBC system, as illustrated in Fig. 28 [68]. In that study, the TBC was exposed to different thermal cycles, including the top surface coating, bond coat and the interface regions of the coating.

For this TBC system, a nickel-based super-alloy (GH3030) substrate having dimensions of 20 × 5 × 2.4 mm^3 was employed. For the bond-coat a NiCrAlY powder with 20–30 μm grain size was sprayed onto the substrate by low pressure plasma-sprayed technique having a thickness of 150 μm. A commercial Vickers indentation instrument (HVS-30) was redesigned for conducting the test. For the determination of the Young’s modulus of the TBCs, the nanoindentation with an indenter equipped with a three-sided pyramidal diamond tip having a radius of 200 nm with peak load 3 N was implemented. To conduct these tests, the loading as well as the unloading times were 100 s and the holding time was 20 s, respectively. Furthermore, an analytical model along with formulation was also described to determine the interfacial fracture toughness considering residual stress inside the coating.

In another study, a new type of indentation technique was introduced, see Fig. 29 [69]. The method is known as cross-sectional indentation method. The method was developed for measuring the mixed-mode I/II interfacial fracture toughness of thermal barrier coatings (TBCs) of turbine blades manufactured by an electron beam physical vapor deposition (EBPVD) system. A scanning electron microscope and luminescence mapping were utilized to investigate the crack length and delamination behavior between the thermally grown oxide (TGO) bond coat interface. In that study, a semi-circular shaped delaminated area was also observed. The indentation tests were carried out by a hardness testing machine providing six loading options from 9.8 to 294 N (1–30 kg), where a sharp cone diamond indenter with an apex angle of $2\theta = 90^\circ$ was applied for testing.

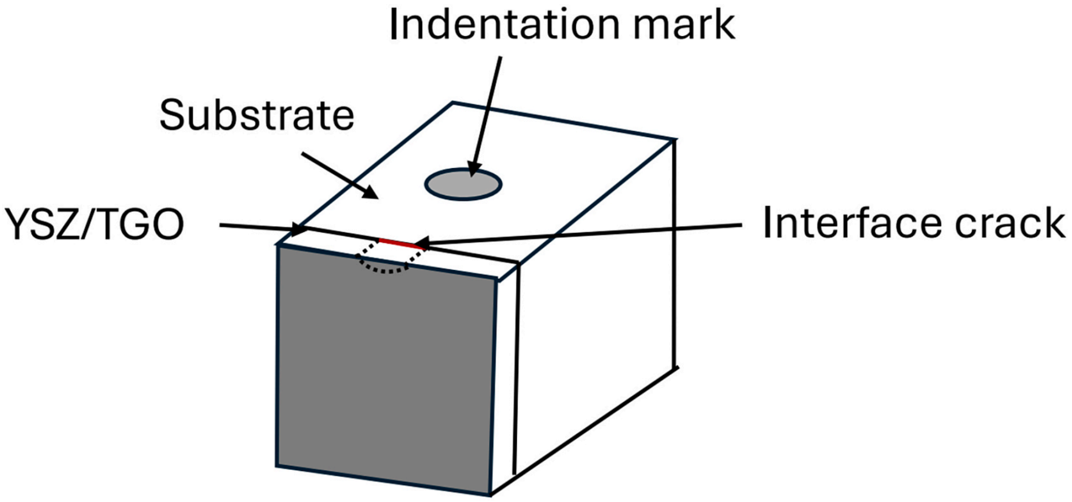

Fig. 29. Schematic of the cross-section indentation (CSI) test arrangement. The broken line indicates the extent of the delaminated region induced by the indent (adopted from Ref. [69]).

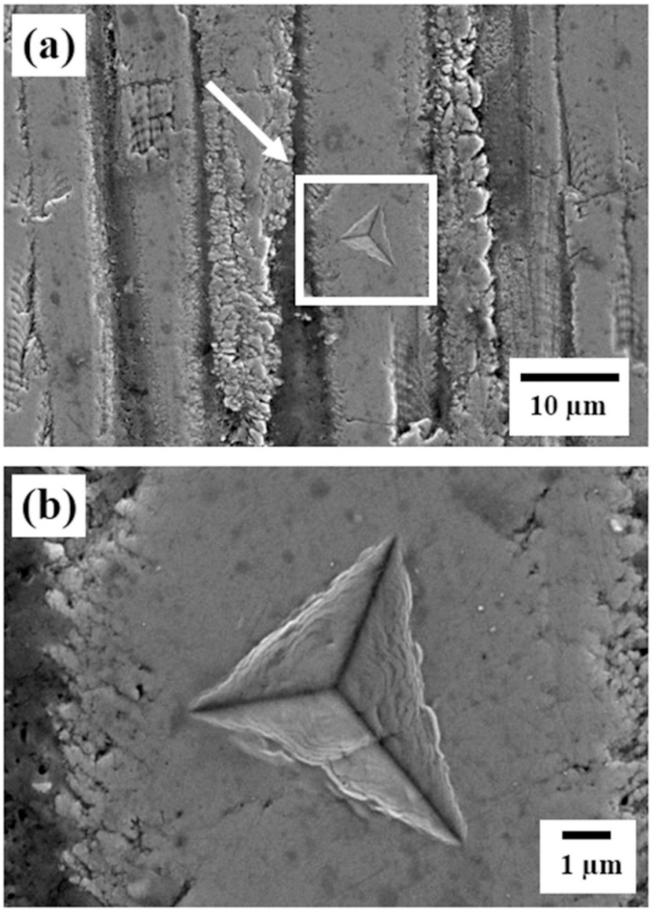

Fig. 30. (a) Low- and (b) high-magnification SEM micrographs of a nano-indentation mark on the side surface of a 4 mol% Y_2O_3–ZrO_2 coating after heat treatment at 1400 °C for 2 h [96].

Nanoindentation was performed in TBCs to determine the nano-mechanical properties including the nano-hardness and the elastic modulus of the 4YSZ topcoat to study the isothermal effect, see Fig. 30 [96]. The tested topcoat was 300 μm thick and the substrate was 2 mm made of 4 YSZ. In that study, the topcoat was heat treated at 1400 °C for 0, 2, 20 and 100 h. To perform the nanoindentation test, a 115° triangular pyramid indenter was employed at a constant load of 100 mN, loading and unloading time was 5 s each. To determine the degree of anisotropy of the coatings, ten indentations were carried out on the top and side surfaces of all the coatings. The hardness and elastic modulus after 100 h of thermal exposures increased due to the densification of YSZ grains and the depletion of pores because of sintering for longer aging times. No fracture toughness of the topcoat as well as interfacial facture toughness was determined.

Nanomechanical properties of nanostructured 8YSZ (n-8YSZ) and conventional 8YSZ (c-8YSZ) were determined by nanoindentation [97]. Both coatings were fabricated by atmospheric plasma spraying (APS). The tested coatings were 300 μm thick. In that study, the elastic indentation work and the plastic indentation work were measured to compare the nanomechanical properties of n-8YSZ and c-8YSZ coatings. That study only investigated the elastic and plastic behavior of the coatings; no fracture toughness or interfacial adhesion properties were evaluated with nanoindentation.

The application of nanoindentation was also broadened to study the interfacial adhesion energies in thin barrier coatings in microelectronics devices [98]. The studied microelectronics device was comprised of silicon wafers (725 μm thick) as substrate with 800 nm of borophosphosilicate glass (BPSG) deposited from plasma-enhanced chemical vapor deposition (PECVD), followed by 400 nm of PECVD silicon nitride (Si_3N_4). A 300 nm thick Tungsten-Titanium (WTi) film was sputter deposited on the Si_3N_4. The WTi film acted as an adhesion and diffusion barrier layer.

The interfacial adhesion energy was determined by nanoindentation, see Fig. 31. The nanoindenter was employed with a 90° conical diamond tip, which had a 1 μm tip diameter. A load range between 100 mN and 500 mN was carried out to generate indentation-induced delamination, presented in Fig. 32 via FIB cross-sections. Fifteen indents were performed per maximum load in this range with increasing loading intervals of 50 mN. The indents were set in a grid being 250 μm apart from each other to avoid any interaction of the formed blisters, indent plastic zones, or fracture events.

After indentation, all resulting delaminations were imaged with an AFM (atomic force microscope) or CLSM (Olympus LEXT OLS 4100). The buckle measurements were made from the AFM and CLSM images and the model of Hutchinson and Suo was modified for a bi-layer film to calculate film stresses and adhesion energies. The adhesion energy was calculated in terms of energy release rate by the following equation,

$$G = c_2\left[1-(\sigma_b/\sigma_d)^2\right]\frac{(1-\nu_w)h\sigma_d^2}{E_w} \tag{16}$$

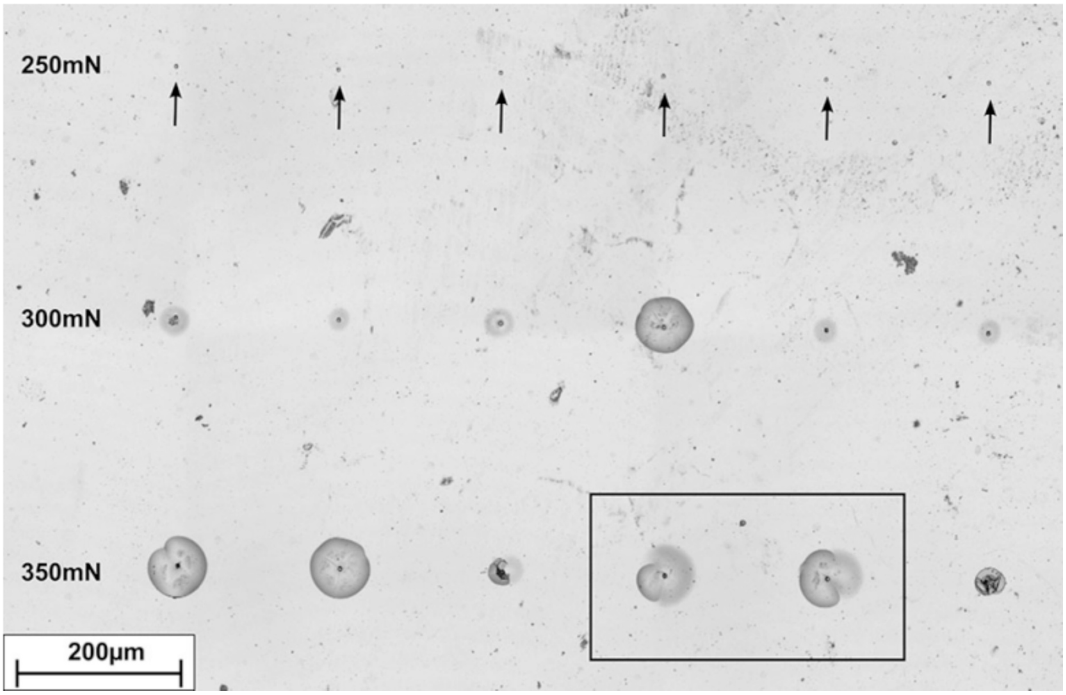

Fig. 31. Indentation buckle overview in a load range of 250–350 mN. Indents made with 250 mN did not produce buckles (indicated by arrows). At 300 mN, two sizes of buckles were produced, small (about 30 μm width) and large (about 60 μm width). Loads of 350 mN resulted in two types of delamination, either large circular buckles or film spallation [98].

where h is the total thickness of the buckling films, σ_b is the critical buckling stress, σ_d is the driving or residual stress, E_w and ν_w are the elastic modulus and Poisson's ratio of the whole buckling system, respectively, with $c_2 = [1 + 0.9021(1 - \nu_w)]^{-1}$. The detailed expressions to calculate the σ_b and σ_d are provided in Ref. [98].

The applicability of the indentation test was later extended to solid oxide cells to estimate the mode II interfacial fracture toughness between the electrolyte and electrodes. The indentation test was performed to determine the interfacial adhesion of solid oxide fuel cells in terms of the radius of the annual crack, as displayed in Fig. 33 and Fig. 34 [99]. An analytical expression was also provided to calculate the interfacial adhesion properties. In that test study, the investigated solid oxide fuel cell included a 0.8 mm thick NiO-YSZ cermet substrate, a 15 μm thick NiO-SDC ($(SmO_{1.5})_{0.2}(CeO_2)_{0.8}$) anode layer top of the NiO-YSZ substrate and a 15 μm thick SDC electrolyte on the anode layer. The applied indenter to perform the test was a Rockwell C indenter (a spherically conical diamond tip of a radius of 200 μm with an included angle of 120°) of a commercial scratch tester where the specimen movement of the tester was disabled.

Furthermore, the elastic modulus, hardness, and fracture toughness of porous LSCF thin films depending on the different sintering temperatures indicating different porosity levels were investigated by nanoindentation techniques as a function of the influence of indenter tip geometries [12,13,100–102].

The key benefits of the indentation method are that it is easy to perform and applicable for very small and thin coating to substrate specimens (less than 1 mm) such as thermal barrier coatings and solid oxide fuel cells (SOFC). However, the notable drawbacks of such test methods are the complexity of specimen geometry and specimen fabrication via FIB in case of nanoindentation. Further weakness is finding the exact indentation location at the interface for the cross-sectional nanoindentation specimens, which is often challenging. Moreover, the evaluation of the tests is dependent on the indenter tip geometry. Furthermore, indentation induced delamination nanoindentation test require complicated postprocessing by using the FIB to view the cross-section of the delamination.

4.1.4. Scratch test

Scratch tests are performed to determine the adhesion strength to the coating with the substrate. It is another variant of the indentation test where the indenter is moving to separate the coating from the substrate. The mode II interfacial fracture toughness is determined by this method. In this subsection, the micro and nano-scratch tests along with the microstructure of tested specimen, testing conditions, advantages and disadvantages are discussed.

For ceramic coatings, a quantitative scratching method is described in the ASTM Standard C1624 – 05 [103]. With this standard it is possible to determine the critical force which is needed to remove the coating from the substrate. A stress dependent analysis as well as failure modes depending on the critical force was described in Ref. [57–60]. Later, a mathematical model was proposed for thin coatings to determine the compressive stresses induced by the scratch indenter [104]. Another model was introduced for the chipped coatings to estimate the interfacial fracture toughness along with interface fracture energy [105]. Furthermore, an overview for the quantification of coating adhesion via scratch testing is described in Ref. [106].

An investigation of the adhesion strength between component layers in a multi-layer coating system was carried out by scratch test via a Rockwell Indenter, as illustrated in Fig. 35 [107]. The tested coating was a $TiC/Ti(C_x,N_{1-x})/TiN$ coating system manufactured through the vacuum-arc method on a high-speed steel substrate. In this test, a load range from 0 to 100 N was applied on the sample surface for the scratch test. In that study, no interfacial fracture toughness was calculated.

The scratch test was further implemented in TBC systems where a comparison of 8YSZ, $La_2Zr_2O_7$ (LZ) and $La_2(Zr_{0.7}Ce_{0.3})O_7$ (LZ7C3) TBCs was studied [108]. The SEM surface morphologies of the different coatings after scratching are presented in Fig. 36. The LZ and LZ7C3 TBCs were manufactured by an EB-PVD process where the bond coat (BC) of NiCrAlYSi was deposited on the substrate by arc ion-plating. In this test, a transverse scratch tester (WS-92 automatic scratch tester) with a load of 200 N at a scratching speed of 4 mm/min was applied to determine the interfacial strength. In that study, a diamond indenter (R = 0.2) was employed to perform the scratch test under the applied load.

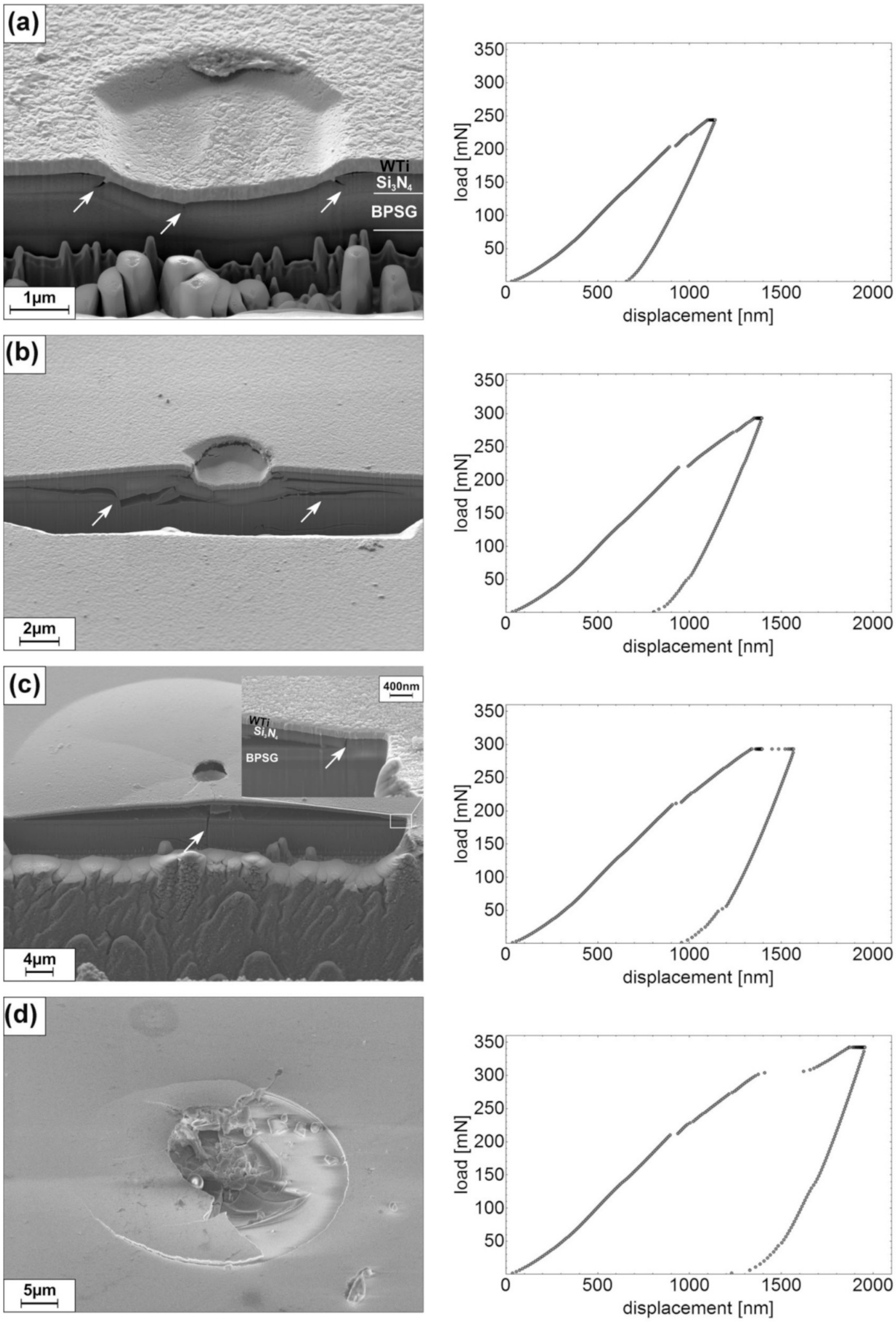

Fig. 32. FIB cross sections of indents made with loads of (a) 250 mN, (b) and (c) 300 mN, and (d) 350 mN. The load–displacement curves are shown next to the corresponding indent. The cross sections show the development of the interface crack and the fracture underneath the indenter with increasing load. The load–displacement curves reveal the pop-in events associated with the fracture and delamination events [98].

No evaluation of interfacial toughness was determined.

Nano-scratching was introduced in TBCs to understand the interfacial behavior of multilayered zirconia toughened alumina (ZTA) and c-zirconia coatings were fabricated by electron beam physical vapor deposition (EBPVD) on 617 Ni-based super alloy [109]. The specimens after scratching are presented in Fig. 37. To perform the nano-scratching a Rockwell indenter with a tip radius of 2 μm and a die angle of 90° was employed. The indenter was sliding with a constant velocity of 3 mm/min and an increasing load of 80 mN/min on the specimen. During the scratching process, the tangential force and normal force along with scratching depth were recorded. The penetration depth of the indenter and the residual scratch depth were calculated from the data of a surface scan with minimal load before and after the scratch testing. In that study, no interfacial toughness was determined, only adhesion strength evaluated based on critical normal force.

In another study, nano-scratch testing was implemented in a wide velocity range of high-energy plasma sprayed yttria-stabilized zirconia (YSZ) thermal barrier coatings to improve the micro-adhesive properties of the splashing splats on the substrate [110]. The splat and topcoat were made of YSZ particles. The interfacial adhesion was determined by the failure of the splat and detachment from the substrate, displayed in Fig. 38. The interfacial fracture toughness between the YSZ splat and the substrate was not evaluated, only the failure load was determined.

Nano-scratching was implemented on the environmental barrier coatings to determine the interfacial fracture energy and interfacial fracture toughness [111]. The polished microstructure of the tested EBC

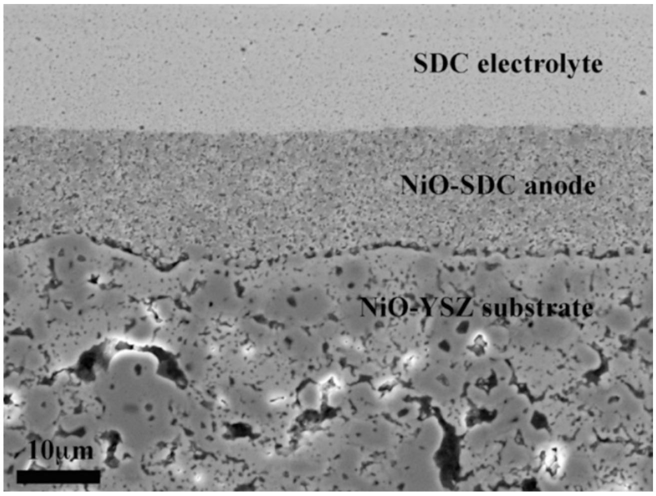

Fig. 33. SEM image of the polished cross-section of the two-coating specimen of substrate/anode/electrolyte [99].

is displayed in Fig. 39. The film thickness after 3 μm diamond paste polishing was $t = 1.07 \pm 0.15$ μm, the surface roughness R_a was less than 6 nm, which was measured by means of atomic force microscope (AFM). The tested coating to substrate material was a mullite film on top of silicon carbide (SiC) substrates, which was deposited using a chemical vapor deposition method. The nano-scratching was performed for both single and multilayered ceramic coating systems. In this test, controlled damage, radial and lateral cracks were introduced until the final delamination and repeated chipping coatings were observed.

The nano-scratch tests were performed using a nanoindenter. The SEM post process analysis for low-load scratching is presented in Fig. 40 and for high-load scratches, it is provided in Fig. 41. A Berkovich indenter was employed to perform progressive load nano-scratches on the polished surfaces of the studied films at a continuous scratch rate of 1 μm/s. The tests were performed to evaluate the intrinsic structural integrity of the mullite films without the significant influence of the substrate in the mullite/SiC coated system. Two load conditions were set for the experiments: (i) maximum load of $P_{max} = 50$ mN and a scratch length of $l_{max} = 50$ μm (loading rate of 1 mN/s; referred to as the "low-load" condition) and (ii) maximum load of $P_{max} = 500$ mN and scratch length of $l_{max} = 200$ μm (loading rate of 2.5 mN/s; referred to as the "high-load" condition). Both loading conditions were applied to observe the damage mechanisms of the film.

Various models were applied to calculate the adhesion energy or the interfacial fracture energy [57,105,112–114] and the interfacial fracture toughness was calculated from Equation 17.

$$K = \sqrt{\frac{G \cdot E_f}{\left(1 - \upsilon_f^2\right)}} \tag{17}$$

where K is the interfacial fracture toughness, G is the interfacial fracture energy, E_f is the elastic modulus of the coating and υ_f is the Poisson's ratio of the coating.

A new cross-sectional scratch test was introduced to perform interfacial adhesion testing on environmental barrier coatings, which is

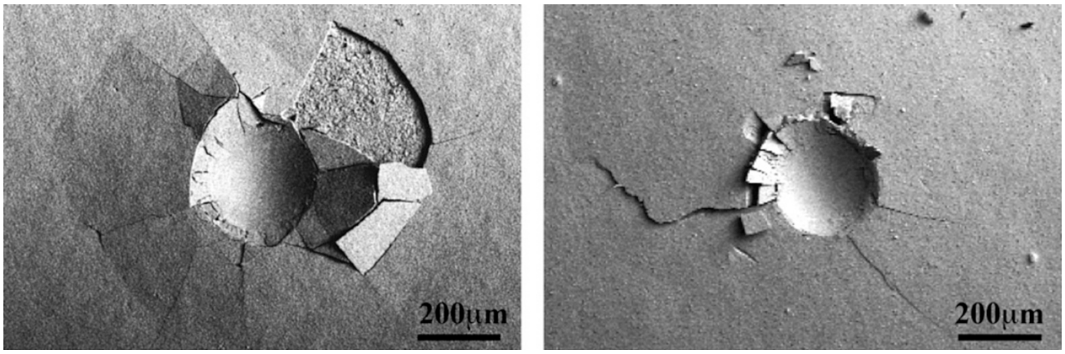

Fig. 34. Top views of indentation delaminations caused by Rockwell C indentations at 200 N. (a) NiO-SDC coating delaminated from NiO-YSZ substrate and (b) SDC and NiO-SDC coatings delaminated from NiO-YSZ substrate [99].

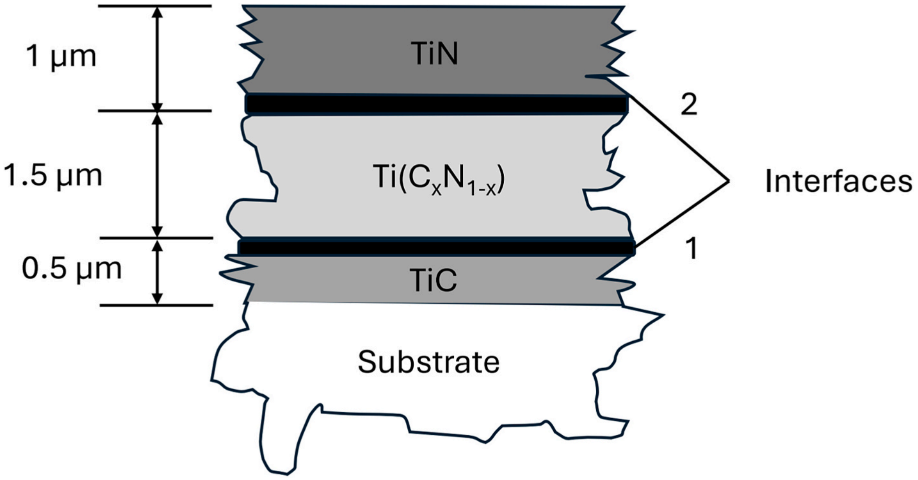

Fig. 35. Multi-layer coating TiC/Ti(C_x,$N_{1\text{-}x}$)/TiN (adopted from Ref. [107]).

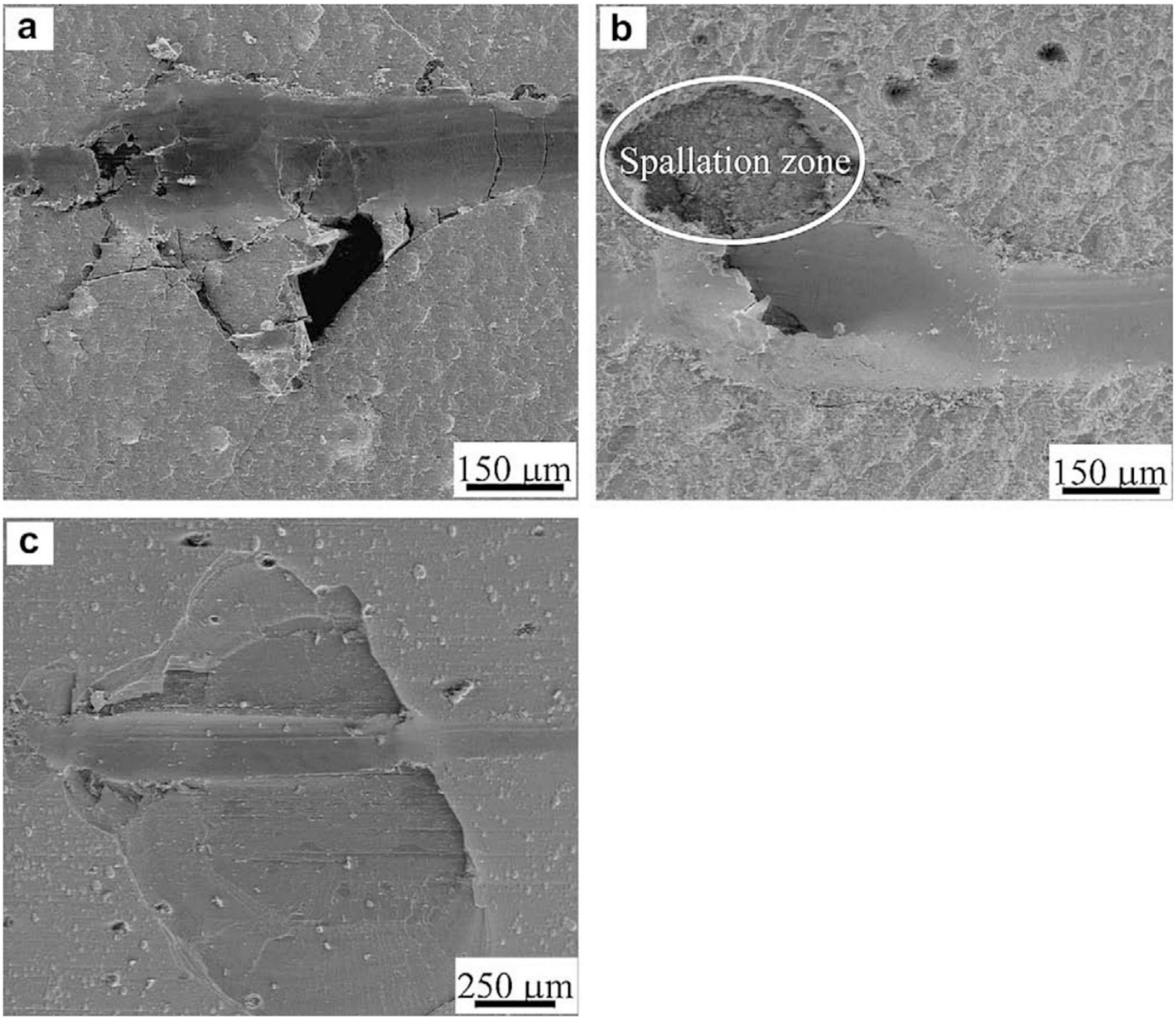

Fig. 36. SEM micrographs of the scratch morphologies for different coatings: (a) 8YSZ; (b) LZ7C3 and (c) LZ [108].

presented in Fig. 42 [115]. The tested EBC was made of a 3 mm thick RB-SiC substrate, a 75 μm thick Si bondcoat, a 100 μm thick YbDS topcoat and a 1000 μm thick abradable porous YbDS layer. All the scratch tests were carried out about a distance of 30 μm from topcoat bond coat interface using the scratch testing machine. The scratch testing device was equipped with a Rockwell indenter which had a radius of 100 μm. The scratches were conducted under constant load of 10 N, scratch speed of 6 mm/min and the length of 1 mm. No evaluation of interfacial fracture toughness was determined.

Similar to the nanoindentation technique, the nano-scratch method is suitable for small and thin (coating thickness needs to be at least 100 nm) specimen. Another key advantage is the simple test setup which does not include complex test devices. Furthermore, the specimen preparation is less complicated. However, one significant disadvantage is that extensive expertise is needed for complex post processing such as focused-ion beam (FIB) to analyze the damage mechanisms.

4.1.5. Bending test

Apart from the DCB tests with or without a wedge, indentation tests and scratch tests, bending tests are available which determine the mixed-mode I/II interfacial fracture toughness. In this sub-section three-point bending (3 PB) and four-point bending (4 PB) tests are elaborated to determine the interfacial fracture toughness between the coating and substrate along with schematic diagrams, test setup and microstructure of the specimens. Furthermore, advantages and disadvantages of individual bending tests are discussed.

4.1.5.1. Three-point bending test (3 PB test). Often three-point bending tests were performed to determine the real time damage evaluation parameters such as surface fracture toughness and the mixed-mode I/II interfacial fracture toughness in thermal barrier coatings, as illustrated in Fig. 43 [116]. The fracture characteristics of the TBCs were usually studied by acoustic emission along with digital image correlation method (DIC). In that study, a theoretical analysis was discussed to determine the surface and interfacial crack of the thermal barrier coatings. The investigated substrate was the Ni-based super-alloy GH3030. The substrate had dimensions of 80 × 9 × 2 mm^3, an air plasma sprayed bond coating of $NiCr_{22}Al_7Y_{0.2}$ having thickness of 150 μm was deposited on the substrate surface, and a 400 μm thick top ceramic coating of ZrO_2-8 wt.%Y_2O_3 was deposited on the free surface of the bond coating. The three-point bending tests were carried out with a universal testing machine. The other installed test facilities were an AE system, a DIC system to measure the strain in TBCs and an image analysis software.

In another study, a modified three-point bending test was introduced to determine the mode I interfacial fracture toughness of thermal barrier coatings, as presented in Fig. 44 [117,118]. The studied substrate was a SUS304 stainless steel having a dimension of 50 × 5 × 2 mm^3 and the coating system consisted of a100 μm thick NiCoCrAl bond-coat and a 200 μm thick yttrium oxide stabilized zirconia topcoat. In this test configuration, a micro-mechanical testing machine was installed to

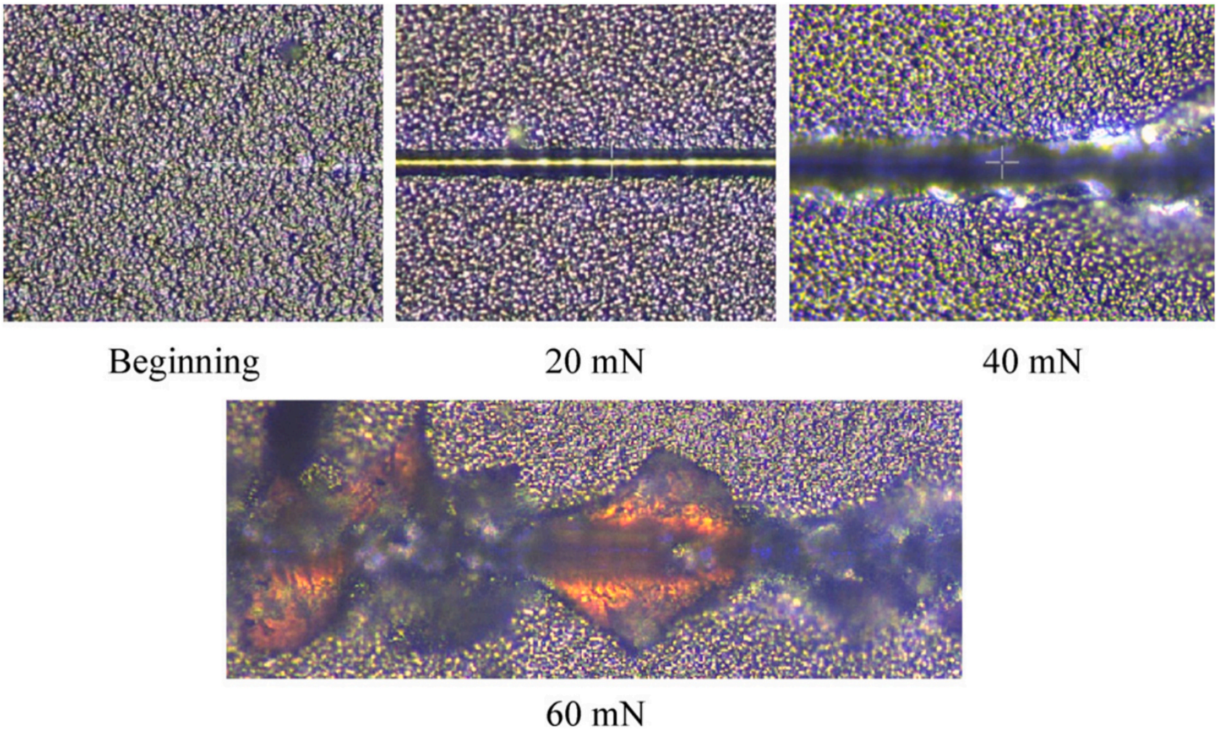

Beginning 20 mN 40 mN

60 mN

Fig. 37. Optical micrographs of the scratch groove at different normal forces, double layer [109].

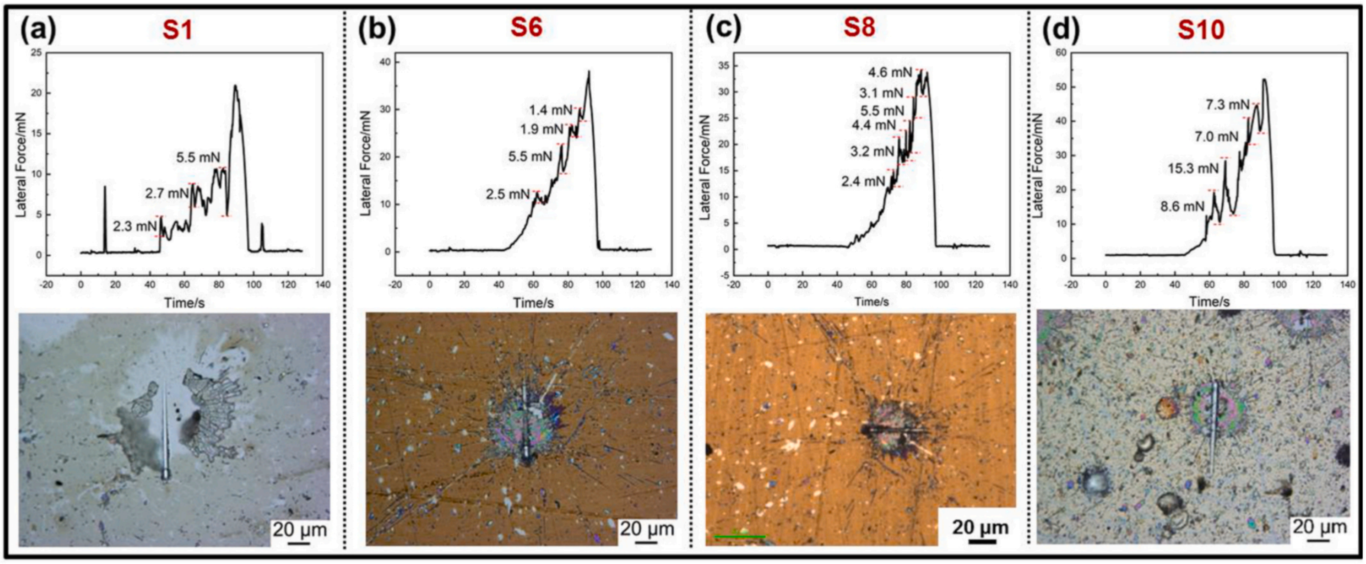

Fig. 38. Nano-scratch curve and morphology of (a) S1; (b) S6; (c) S8 and (d) S10 splats [110].

apply the monotonic load on the specimen. The experiments were carried out with a constant displacement rate of 0.05 mm/min at the loading point, where the force and displacement had a resolution of 1 N and 3 μm, respectively. In this method, real time delamination was monitored by an optical microscope.

The interfacial fracture toughness was calculated from Equation 18 according to Ref. [119].

$$G = \left(\left(\frac{P^2}{2W}\right)\cdot\left(\frac{\mathrm{d}C}{\mathrm{d}l}\right)\right) \tag{18}$$

where G is the critical energy release rate, P is the measured load for starting delamination, W is the width of specimen, l is length of the specimen, C is the compliance of the specimen, expressed as $\frac{u}{P}$; u is the displacement of the specimen.

Later on, using this test methodology, the displacement and strain fields of the TC/BC cross-sections were obtained by a digital image correlation (DIC) method and the crack length was calculated by an inverse finite element model (FEM) [120]. The significant advantages of this test method are simple specimen preparation and test procedure. Further advantages are generation of linear bending moments along the specimen length for stable and controlled crack propagation. These moments are suitable for thermal barrier coatings and multilayer structures. However, the notable downsides of this test are that the tested area is limited and applicable only for thick multi-layered coating systems.

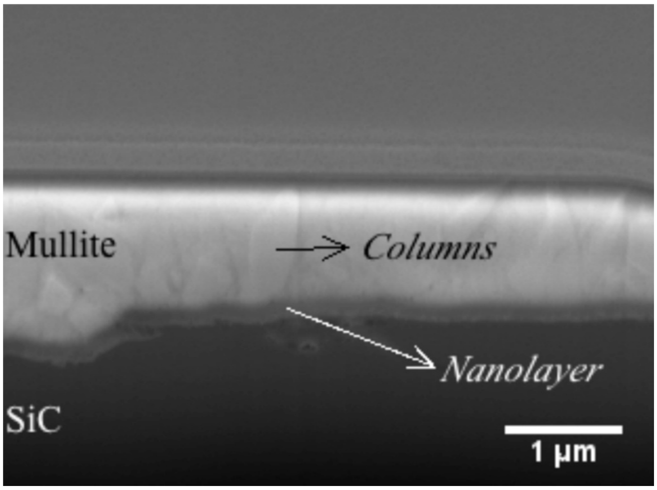

Fig. 39. FIB cross-section of a polished film. The columnar microstructure and nanolayer are indicated [111].

The applicability of the three-point bending test was further implemented to solid oxide cells where a three-point bending test was performed based on the Schwickerath crack initiation test as per ISO 9693 to determine the bonding strength in solid oxide fuel cells' interfaces [121]. The investigated materials were a 3YSZ/Ni anode support and three different configurations of cathodes made of LSM-CGO, LSC-CGO and LSCF-CGO, respectively. The reported average total thickness of the cells was 0.4 ± 0.01 mm, and the interconnect was a 0.3 mm thick Crofer 22 APU made from stainless steel. By this method only the bonding strength of the interfaces of solid oxide fuel cells were evaluated. In that study, neither the interfacial fracture toughness between the interconnector nor the interfacial fracture toughness between the electrolyte and electrodes were determined.

4.1.5.2. Four-point bending test (4 PB test). Apart from three-point bending tests, four-point bending tests are frequently performed to measure the interfacial fracture toughness in coatings to substrate systems. The four-point bending (4 PB) test was carried out for the evaluation of delamination resistance in plasma-sprayed thermal barrier coatings along with the effect of isothermal aging, see Fig. 45 [122]. In that study, the investigated TBC system was comprised of 8 wt% yttria partially stabilized zirconia, 8YSZ as a top coating (TC). The TC had a thickness of 330–340 µm. The CoNiCrAlY alloy and LCO22 were used as bond coating (BC), which had a thickness of 340–350 µm. The substrate was made of single crystal Ni based super-alloy CMSX-4. The substrate had a thickness of 5 mm and a width of 10 mm. The overall prismatic bar specimen had dimensions of 130 × 10 × 9.9 mm^3 with a notch of 2–3 mm in width and the existing stiffener for preventing the vertical crack had dimensions of 60 × 10 × 4.2 mm^3.

In this test configuration, a creep machine with a load cell of 2 kN and a constant displacement rate of 7 mm/min was employed. This creep machine was equipped with a spring unit converter and an extensometer. As shown in Fig. 45, the loaded four-point bending specimen was encountered with delamination under the combination of residual stresses and the stresses caused by the applied mechanical loads during the test. Thus, the energy release rate G was expressed as following,

$$G = G_p + G_{pr} + G_r \tag{19}$$

where G_p represents the standard linear elastic fracture mechanics expression and the residual stress-independent contribution to the crack driving force, G_{pr} defines the interaction between the applied load and the residual stresses distribution and the last term, G_r describes the release rate for the relaxation of the residual stresses, which means crack extension driving force without applied force.

The first term G_p, the energy release rate was considered without the residual stresses. It was expressed as a modification formulation according to the Ref. [123],

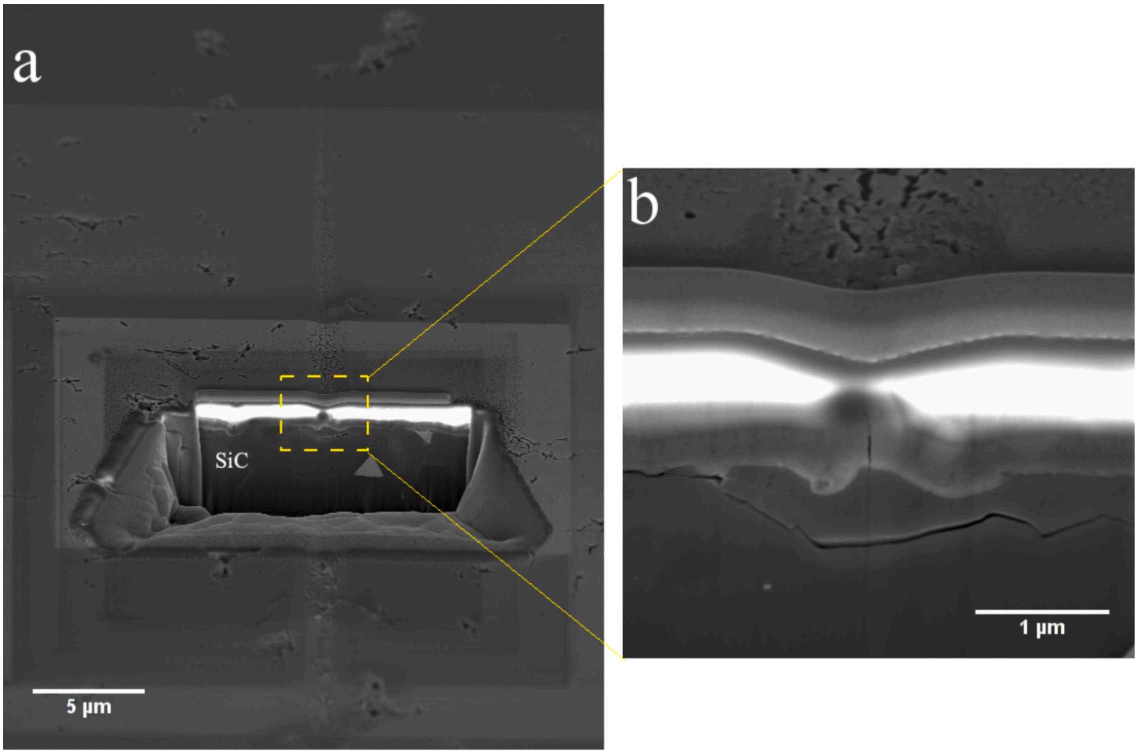

Fig. 40. (a) Cross-section performed using FIB at the midpoint of the scratch, i.e., at $P_{max} = 25$ mN, $l_{max} = 25$ µm. (b) Higher magnification image focused on the center of the track [111].

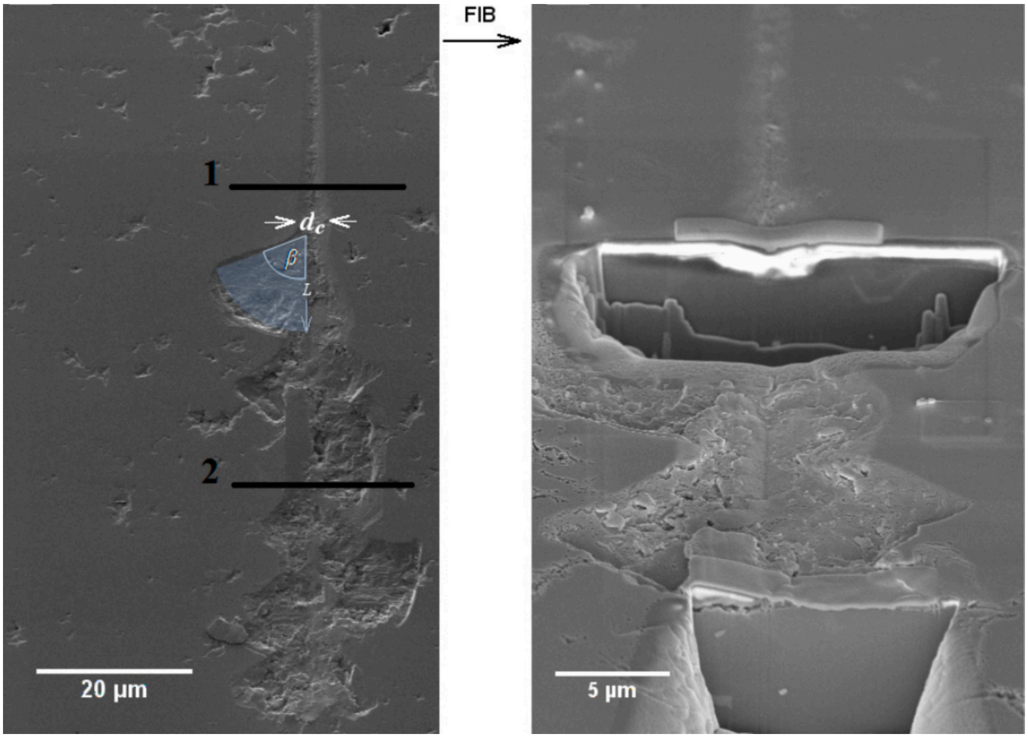

Fig. 41. Surface SEM images of a high load nano-scratch (left) before and (right) after the FIB sectioning process [111].

$$G_p = \frac{M^2}{2 \cdot b^2} \cdot \left\{ \frac{1}{E^*_{c,3} \cdot I^*_{c,3}} - \frac{1}{E^*_{c,5} \cdot I^*_{c,5}} \right\} \tag{20}$$

where $M = \frac{P \cdot L}{2}$ is the constant bending moment, P is the measured critical load for the crack initiation, $I^*_{c,k}$ is the second moment of per unit width, with

$$I^*_{c,k} = \frac{1}{E^*_{c,k}} = \sum_{i=1}^{k} E^*_i \cdot \left\{ I_i + t_i \cdot \left(\frac{t_{c,i} + t_{c,i-1}}{2} - Y_{0,k} \right)^2 \right\}, \quad \text{with} \quad Y_{0,k} = \frac{\sum_{i=1}^{k} E^*_i \left(t^2_{c.i} - t^2_{c.i-1} \right)}{2 \cdot \sum_{i=1}^{k} E^*_i \cdot t_i},$$

$$E^*_{c,k} = \frac{\sum_{i=1}^{k} t_i \cdot E^*_i}{\sum_{i=1}^{k} t_i}, \; I_i = \frac{t_i^3}{12}, \; t_{c,i} = \sum_{i=1}^{i} t_i, \; E^*_i = \frac{E_i}{(1 - \upsilon_i)}$$

where t is the thickness of the layer, b is the width of specimen, and E is the Young's modulus and ν is Poisson's ratio, and the subscripts 1, 2,..,5 refer to the substrate, the BC layer, the TGO layer, the TC layer, and the stiffener, respectively.

The second term G_{pr} was obtained as described by Ref. [124],

$$G_{pr} = \frac{P}{2} \cdot \frac{\mathrm{d}u_r}{\mathrm{d}a} = \frac{P}{2} \cdot \frac{\Delta u_r}{\Delta a} \tag{21}$$

where u_r is the residual displacement, P is the measured critical load and a is the crack length.

The last term G_r was calculated according to the Ref. [124],

$$G_r = \frac{1}{2} \cdot \left(\frac{I_4}{E^*_4} \cdot \kappa^2_{tc} + \frac{I_{c,3}}{I^*_{c,3}} \cdot \kappa^2_{sb} + \frac{t_4}{E^*_4} \cdot \sigma^2_{tc} + \frac{t_{c,3}}{E^*_{c,3}} \cdot \sigma^2_{sb} \right) \tag{22}$$

where κ represents the elastic stress gradient, relaxed by allowing the layer to bend freely, σ defines the average axial elastic stress in the layer to extend or contract freely. The subscript tc and sb refer to the top coating (TC) and the composite of the substrate and bond coating (BC), respectively.

The 4 PB test was implemented to calculate the mixed-mode I/II interfacial fracture toughness in another type of thermal barrier coating system, as depicted in Fig. 46. The ceramic top coating was deposited by electron beam physical vapor deposition (EBPVD) [125]. In that study, to understand the spallation behavior in TBCs, an energetic model was imposed to predict the lifetime in case of cyclic oxidation. The studied TBC system was comprised of substrates from a single-crystal AM1 super-alloy, a bond coat of β-(Ni,Pt)Al or β-NiAl(Zr) and a 135 μm thick EBPVD ceramic top coat of 7 wt.% Y_2O_3-ZrO_2. The tested specimens had dimensions of 60 × 8 × 1 mm^3. Before the conduction of the test, a 1 mm thick steel plate stiffener of AISI 304 L was glued with epoxy adhesive (Araldite 2011) on the ceramic top coating. Furthermore, a wire saw of 100 μm diameter was applied to create the central notch through the stiffener and the ceramic top coating.

In another study, a modified 4 PB test was performed to calculate the mixed-mode I/II interfacial fracture toughness of atmospheric plasma-sprayed thermal barrier coatings, see Fig. 47 [126]. In that study, an analytical solution was also proposed to determine the interfacial fracture toughness. The investigated thermal barrier coating system was comprised of a 4.9 mm thick mild steel Q235 substrate, a 100 μm thick Ni20Cr10Al1Y bond coat and a 250–300 μm thick 8YSZ topcoat which were deposited by atmospheric plasma-spraying. Two stainless steel plates were bonded with commercial adhesive on the wafer with the TBC coatings. The curing of the adhesives was performed at 100 °C for 3 h. To carry out the tests, the wafer was cut into rectangular coupons by a dicing machine. The specimens had nominal dimensions of 42 mm in length, 6 mm in width and 7.3 mm in height. For performing the tests, a servo-hydraulic micro-mechanical testing machine was utilized. To apply the monotonic loads to the specimen, the testing was equipped with a 2000 N load-cell. The tests were conducted at constant displacement rates ranging from 0.01–0.05 mm/min at the loading point. The load, P, and the displacement, u, were continuously measured during the tests by a load-cell and a differential transformer, respectively. The loads were gradually applied to allow the crack to initiate and propagation to occur, and when the crack tip approached the inner loading point, the loads were stopped.

Afterwards, an asymmetric modified 4 PB test methodology was

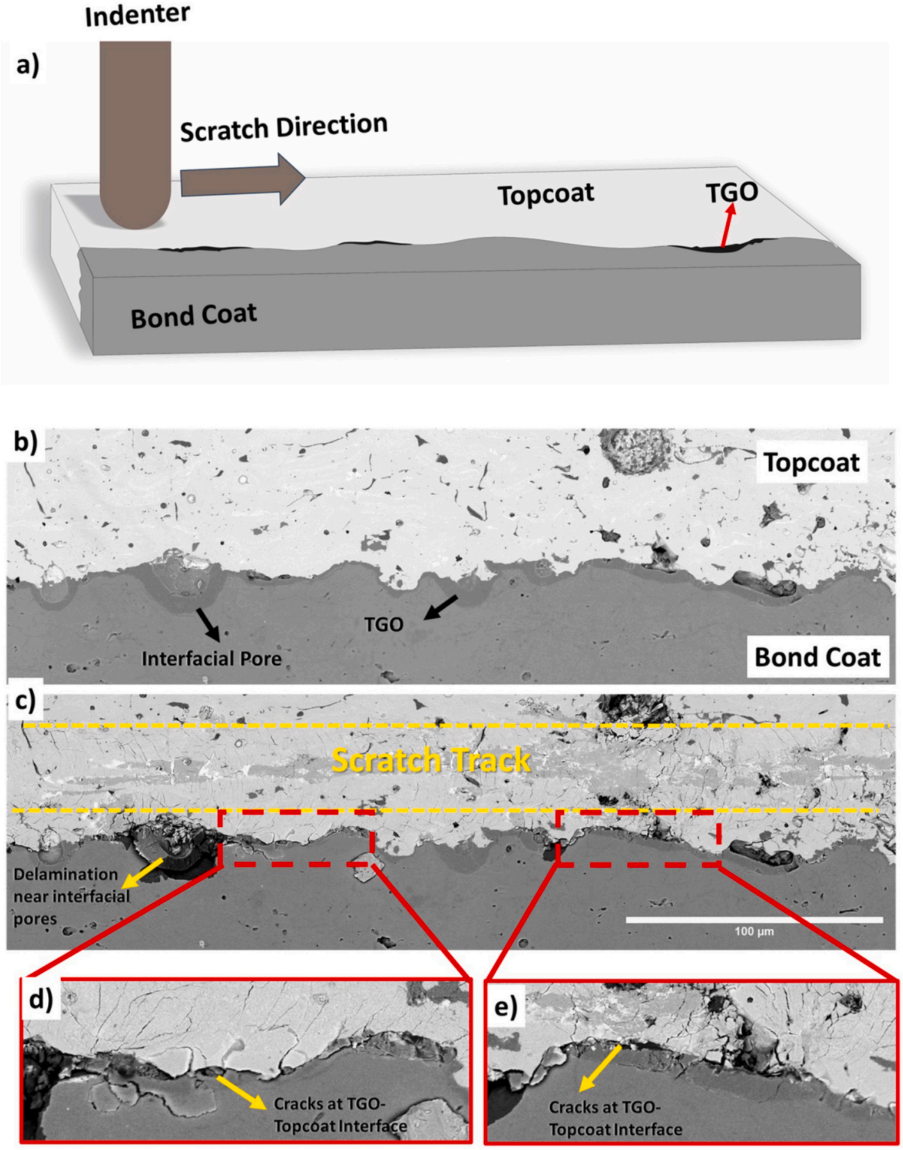

Fig. 42. (A) Schematic illustration of scratch testing parallel to bond coat topcoat interface. (b) and (c) before and after scratch test sem micrographs of the aps coatings exposed to steam for 250 h at 1350 °C respectively, showing traces of severe spallation, primarily in the regions of round shaped porosities. (d) and (e) High magnification micrographs of selected areas with high TGO thickness showing significant failure at the TGO topcoat interface [115].

developed to evaluate the mixed-mode I/II interfacial fracture toughness in double-layer thermal barrier coatings along with understanding the sintering characteristics, as illustrated in Fig. 48 [127]. The crack path during the bending test is presented in Fig. 49. The studied single layer thermal barrier coating was comprised of a substrate of 4.9 mm thick first-generation single crystal alloy in $< 001 >$ direction, a CoNiCrAlY bond coat of 0.32 mm thick and an yttria stabilized zirconia topcoat of 0.51–0.52 mm in thickness, whereas the double-layer thermal barrier coating was comprised of 0.33–0.37 mm thick bond coat and two layers of topcoats. One topcoat layer was 0.40–0.50 mm thick fabricated from gadolinium zirconate (GZO) and the other topcoat layer was 0.10–0.14 mm thick fabricated from yttria stabilized zirconia (YSZ). The energy release rate was calculated as per analytical solution in Ref. [122]. To perform the tests, the specimens were loaded with a constant loading rate of 0.05 mm/min in position control to achieve stable crack growth. To analyze the stable crack growth an LVDT was employed to measure the deflection on the bottom side of the bending specimen.

In another study, an in situ 4 PB test was introduced in a double-ceramic-layer thermal barrier coating (DCL-TBC) system to investigate the failure mechanisms in the perspective of critical crack density and interface fracture mechanics, see Fig. 50 and Fig. 51 [128]. In that study, an analytical approach was proposed to provide the closed-form solution for the crack density and the interface energy release rate. The investigated material system was comprised of a nickel-based super-alloy Hastelloy X having dimensions of 40 × 7 × 1.5 mm^3, a 100 μm thick bond coat of NiCoCrAlY, whereas the LC/YSZ DCL coatings were manufactured by air plasma spraying (APS) method for the different thickness ratios of LC and YSZ layers. The reported total thickness of the two ceramic layers was nearly 300 μm. For performing the in-situ bending test and monitoring the cracking of the TBCs, a four-point bending device (DEBEN, MICROTEST 2000) was integrated into a scanning electron microscope. For carrying out the tests, the inner rollers had a constant speed of 1.6 μm/sec.

In another study, a strain-based lifetime criteria approach was proposed for a novel double-layer thermal barrier coating system by 4 PB tests with the help of in situ acoustic emission method, as provided in Fig. 52 [129]. In that study, the investigated thermal barrier coating was

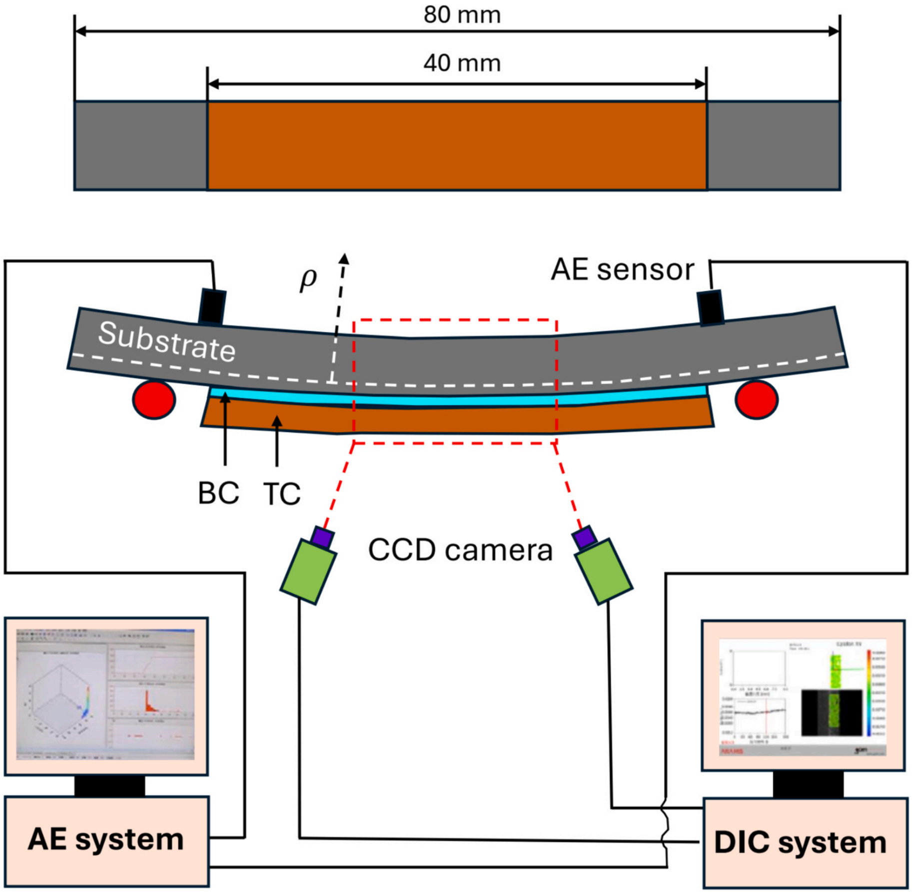

Fig. 43. Schematic AE, DIC monitoring apparatus and specimen dimensions of the three-point bending test (adopted from Ref. [116]).

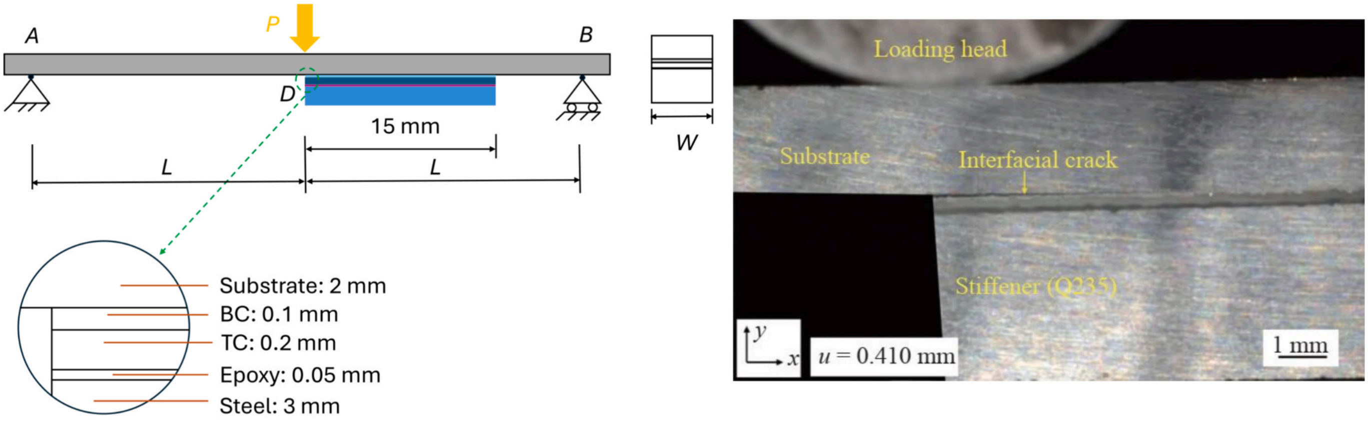

Fig. 44. Specimen shape and size for three-point bending tests. Point D is supposed to be the crack initiation position (adopted from Ref. [118]) (left); cross-sectional image of specimen with displacement of 0.410 mm, magnification is 30 times (right)[118].

comprised of two segments. One system was comprised of the standard TBC with a single-layer topcoat of 500 μm thick 8 wt.% yttria-stabilized zirconia (8YSZ) which was deposited by atmospheric plasma spray (APS) method on top of the 330 μm thick vacuum plasma sprayed NiCoCrAlY bond coat. The other system was consisted of the same bond coat and a double-layer ceramic method, which had a 400 μm thick gadolinium zirconate ($Gd_2Zr_2O_7$, GZO) layer on top of the 100 μm thick 8YSZ layer. For both systems, the substrate of a single crystal nickel-based super-alloy (PWA 1483) had dimensions of 80 × 10 × 5 mm^3 with a notch of 2 mm in depth and 20 mm in width. Failure types depending on the loading scenarios and the empirical equations for the fracture toughness of the coatings corresponding to the failure types were also reported. The 4 PB test was performed with a universal testing machine equipped with a self-designed bending setup. An acoustic emission measurement was utilized for in-situ detection of micro-cracking within the ceramic top layer during the bending test. Moreover, acoustic signals were recorded using a Physical Acoustics PCI card with amplifiers of type 20/40/60 and WD sensors.

The applicability of the 4 PB test is extended to estimate the interfacial fracture toughness in solid oxide cells. The 4 PB test was adopted to determine the interfacial fracture energy between the cathodes and glass ceramic sealants in planar solid oxide fuel cells (SOFC) [70]. In that

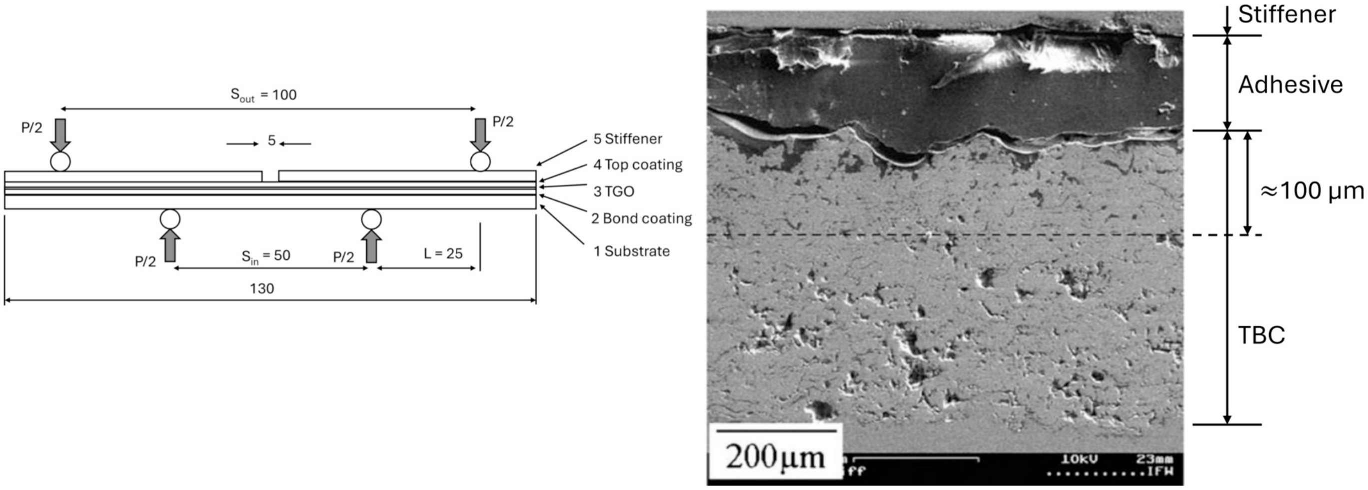

Fig. 45. Specimen of modified four-point bending test (adopted from Ref. [122]), SEM image of the bonded TBC/Stiffener specimens [122].

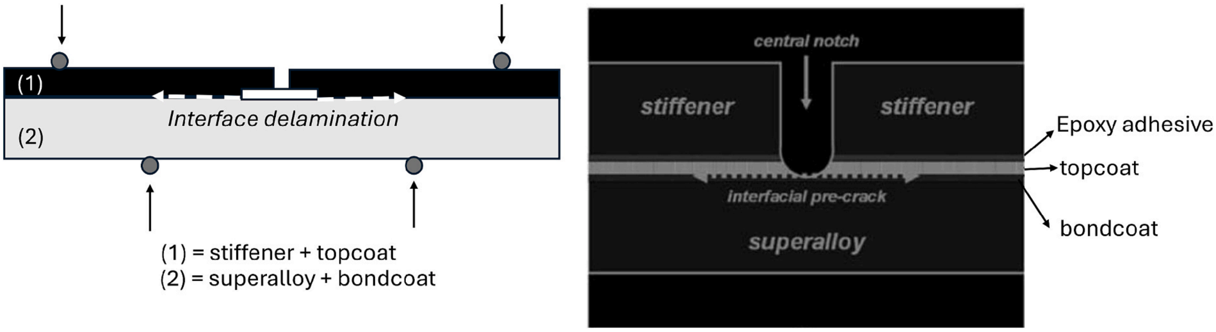

Fig. 46. A bimaterial 4-point bending specimen (adopted from Ref. [125]) and macroscopic cross-sectional view of TBC [125].

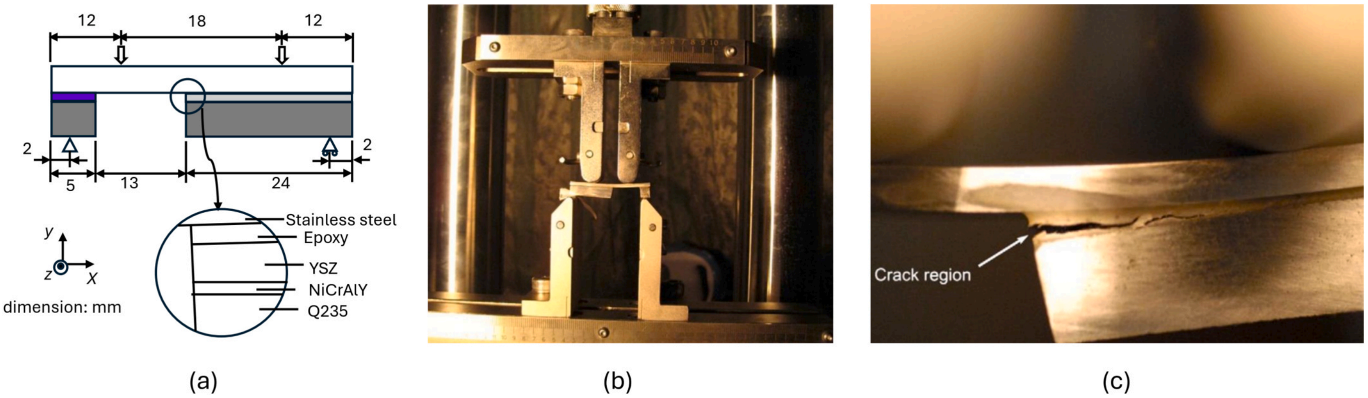

Fig. 47. (a) Shape and size of the modified four-point bending specimen (adopted from Ref. [126]); (b) Photographic illustration of testing system; (c) Overall side view of specimen during the fracture process [126].

study, the reported solid oxide cells were consisted of a porous Ni-yittria-stabilized zirconia (YSZ) cermet anode having a thickness of 1.5 mm supporting a 11 μm YSZ electrolyte film and a porous 60 μm thick lanthanum strontium manganite (LSM).

Later, a reliable method with 4 PB test was developed to calculate the mixed-mode I/II fracture energy at the interface between the porous cathode layer and the electrolyte in planar solid oxide fuel cells (SOFC), see Fig. 53 [71]. The proposed methodology determined the fracture energy by deducting the influence of the glue in the final fracture energy result. An analytical expression was also deduced for producing reliable results. The investigated material was a commercial planar SOFC consisting of a 135 μm thick dense 3YSZ electrolyte. The two sub-layered porous cathode system had a thickness of 16 μm each. The first one was based on LSM/YSZ (functional layer), and the other sublayer consisted of pure LSM outer layer. The anode layer was made of gadolinium doped ceria and nickel (Ni/CGO).

Furthermore, the 4 PB bending was implemented to determine the interface adherence at sealings in solid oxide cell stacks [130]. The investigated materials consisted of joints from Crofer APU (pre-oxidized or coated with $MnCo_2O_4$ or Al_2O_3) sealed with V11 glass. The reported thickness of the Crofer APU and V11 glass were ~ 300 μm and ~ 50 μm, respectively. In another study, the interface fracture energy of contact

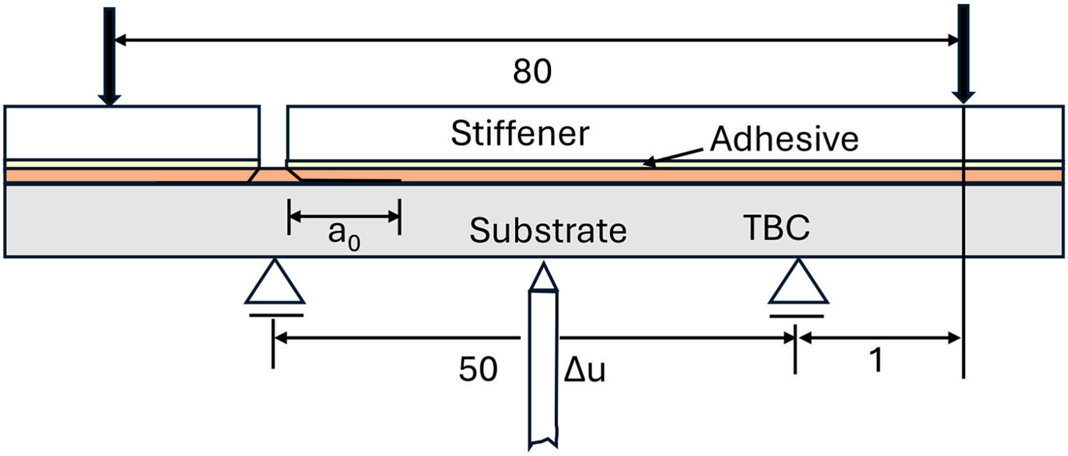

Fig. 48. Modified four-point-bending setup, asymmetric design (adopted from Ref. [127]).

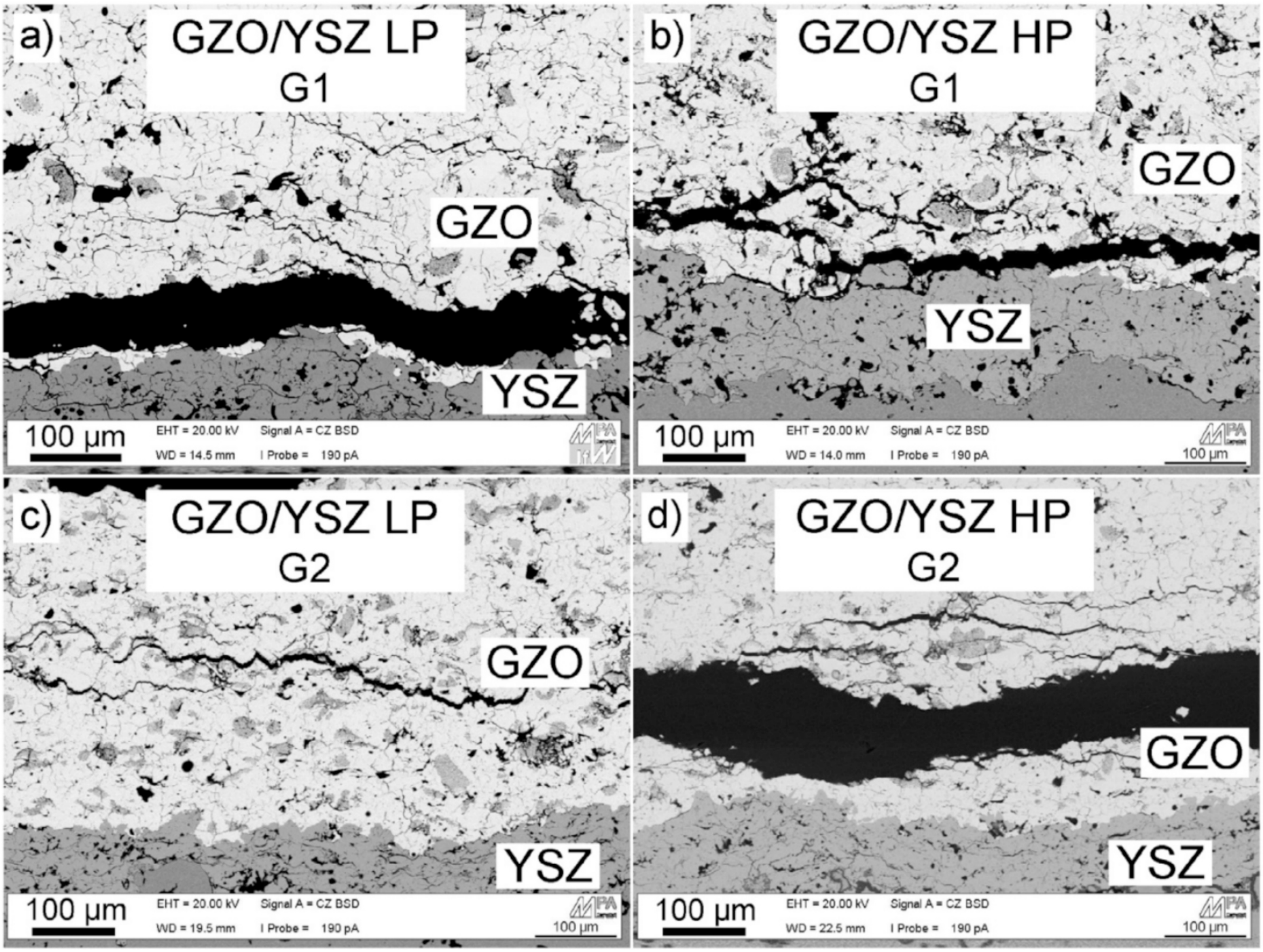

Fig. 49. Crack path during delamination bending experiments [127].

layers in solid oxide cell stacks was determined with modified 4 PB test [131]. The investigation was performed to determine the interfacial fracture energy between the oxygen electrode and the interconnector. Several materials were added to the LSC-CGO and MnCO or Co-coated metallic interconnectors to verify the suitability of the appropriate material pair for the higher interfacial fracture energy.

The 4 PB tests along with different configurations were carried out in different types of thermal barrier coatings and solid oxide cells. The difficulty of symmetrical crack propagation was resolved by using a single crack [126]. The tracking of the crack was carried out with a high-speed camera. Closed-form analytical solutions were available. The applicability of this test method is suitable for multilayer coating

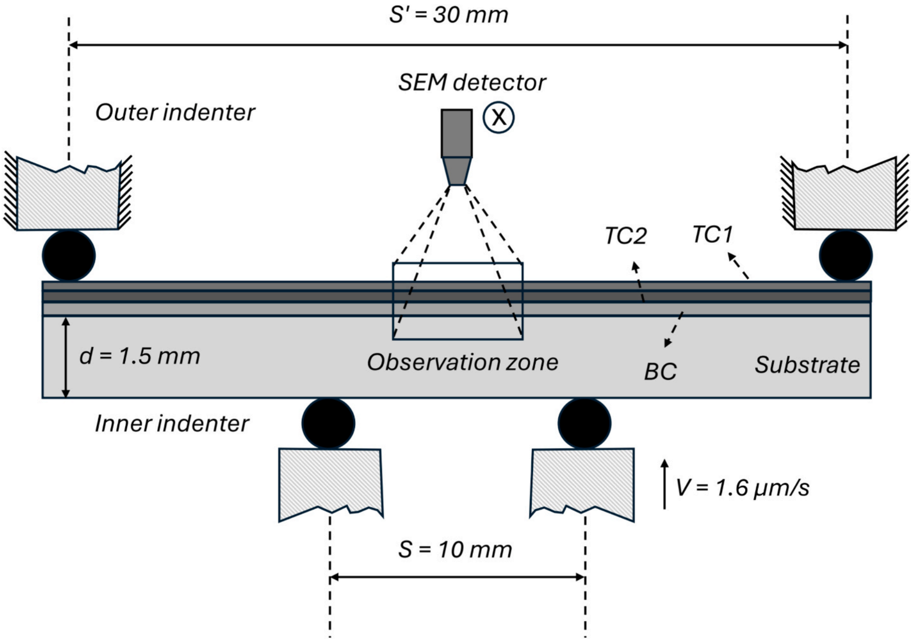

Fig. 50. Schematic diagram of in situ four-point bending test (the cross symbol indicates that the SEM detector is perpendicular to the cross-section of the TBC system sample (adopted from Ref. [128]).

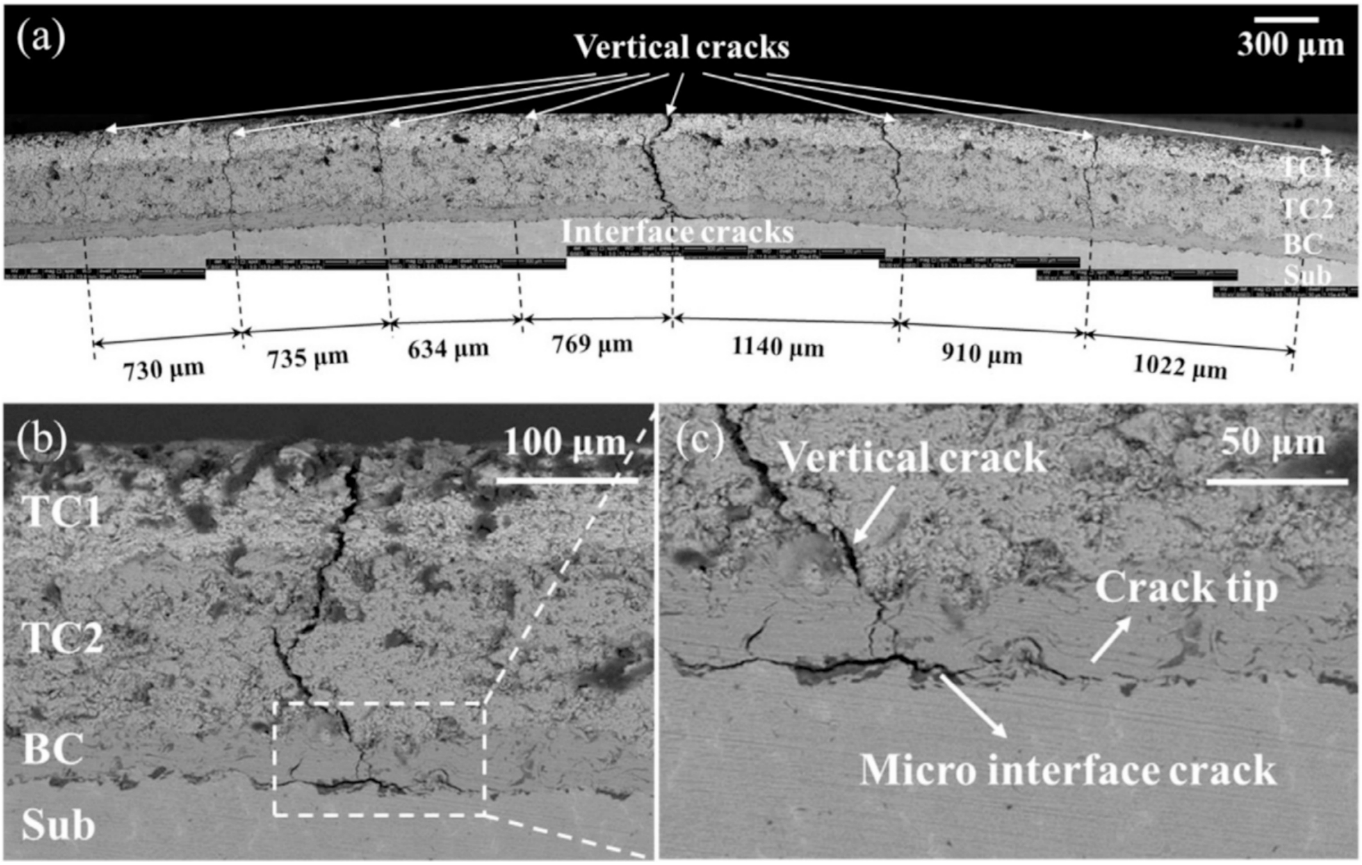

Fig. 51. Backscattered electron images of cross-sections of DCL-TBC system with a ceramic thickness ratio of 100/200: (a) cracks after four-point bending; (b) typical vertical and interfacial cracks in one segment; (c) enlarged view of (b) [128].

systems such as TBCs or solid oxide cells. The notable downsides of this test method are the complexity of the test feature i.e. in-situ crack monitoring in SEM; time consuming test procedure and post processing requires a numerical investigation. Further weakness of this test is the complication of specimen preparation requiring double notches or a single notch.

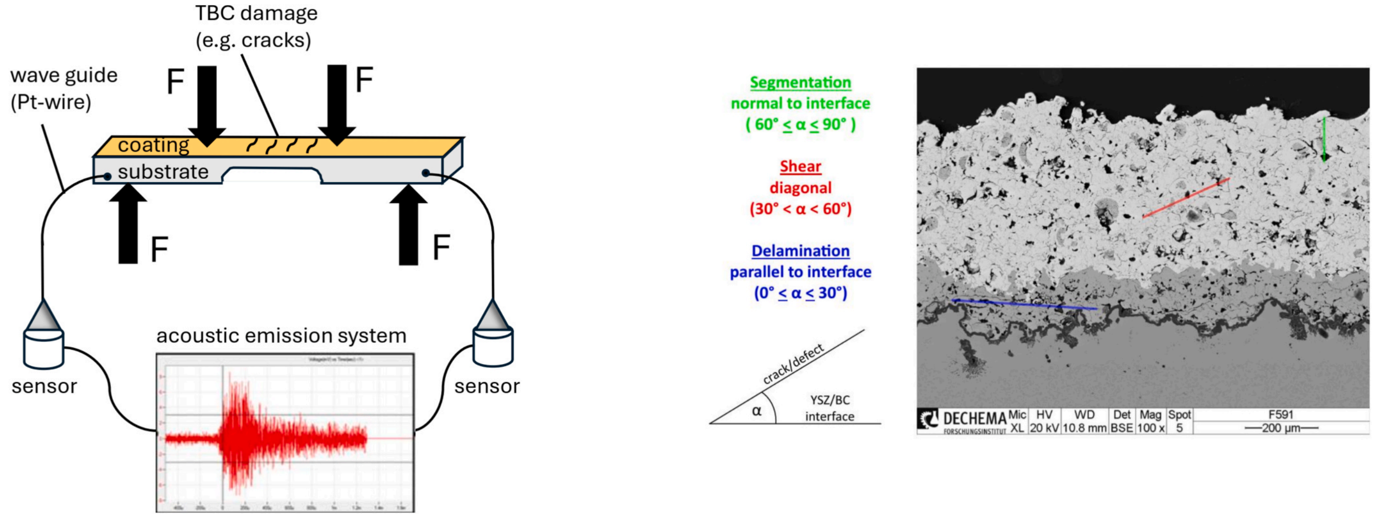

Fig. 52. Schematic illustration of four-point bending setup with in situ acoustic emission measurement (adopted from Ref. [129]) (left); Categorization of defects/cracks with respect to the three corresponding failure modes and SEM image illustrating the different defect orientations [129].

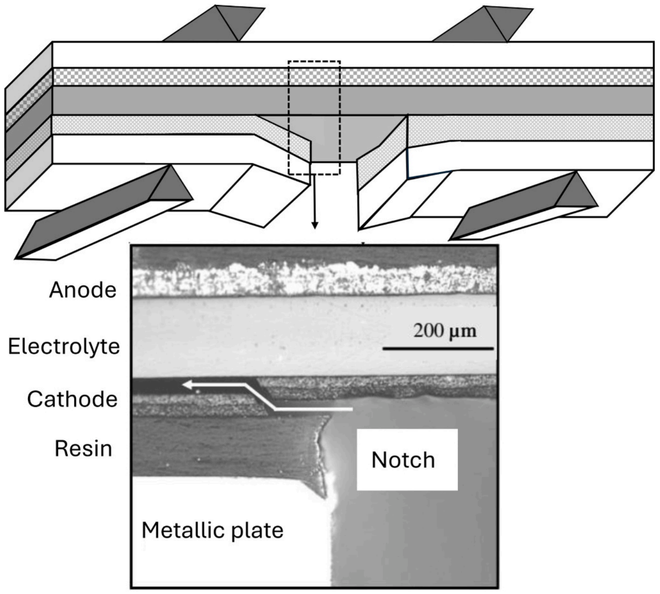

Fig. 53. Geometry of the four-point bending test specimen (adopted from Ref. [71]) and closed view on the notch where an interfacial crack was initiated at the stiffener/resin interface and then rapidly deviated at the cathode functional layer/electrolyte interface (optical microscopy) [71].

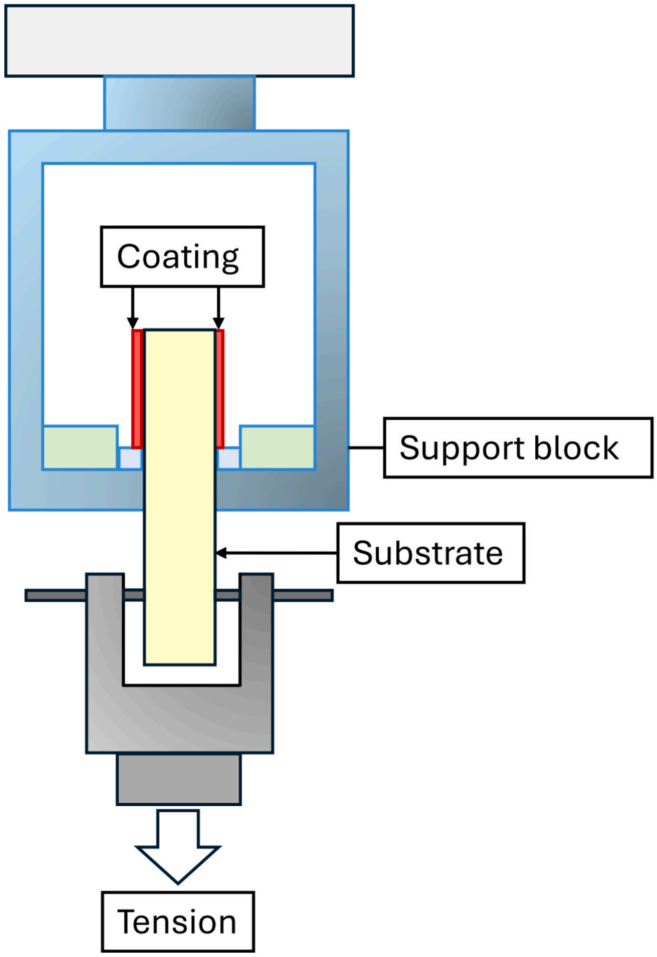

Fig. 54. Experimental arrangement of a ‘‘barb’’ test (adopted from Ref. [134]).

4.1.6. *Barb pullout test*

In this subsection, a new test method to measure the shear interfacial properties known as the barb pullout test along with the schematic of test setup, the microstructure of the fracture surface as well as benefits and drawbacks are discussed.

The barb pullout test method was introduced to determine the mode II fracture toughness in electron-beam physical vapor deposited (EB-PVD) thermal barrier coatings (TBC), see Fig. 54 [132]. The barb pullout tests were performed to calculate the interfacial shear properties in terms of interfacial toughness and coating thickness [133]. In that study, the investigated material included the thermal barrier coating of 4 mol% Y_2O_3 stabilized ZrO_2 thickness of 200 μm, a nickel-based super-alloy (MA738LC) substrate, which had dimensions of 55 × 20 × 2.5 mm^3. A bond coat of NiCoCrAlY was plasma sprayed on top of the substrate. The bond coat had thickness of 100–150 μm [132]. The barb tests were performed by using a screw-driven testing machine. The SEM images of the fracture surface are presented in Fig. 55. The tests were carried out with a constant crosshead displacement rate of 0.1 mm/min. The force–displacement responses during the experiments were digitized and recorded with a digital memory scope. The proposed barb pullout test method did not consider the residual stresses of the coatings, the mode-mixtures and the buckling of the coatings. Later, these limitations

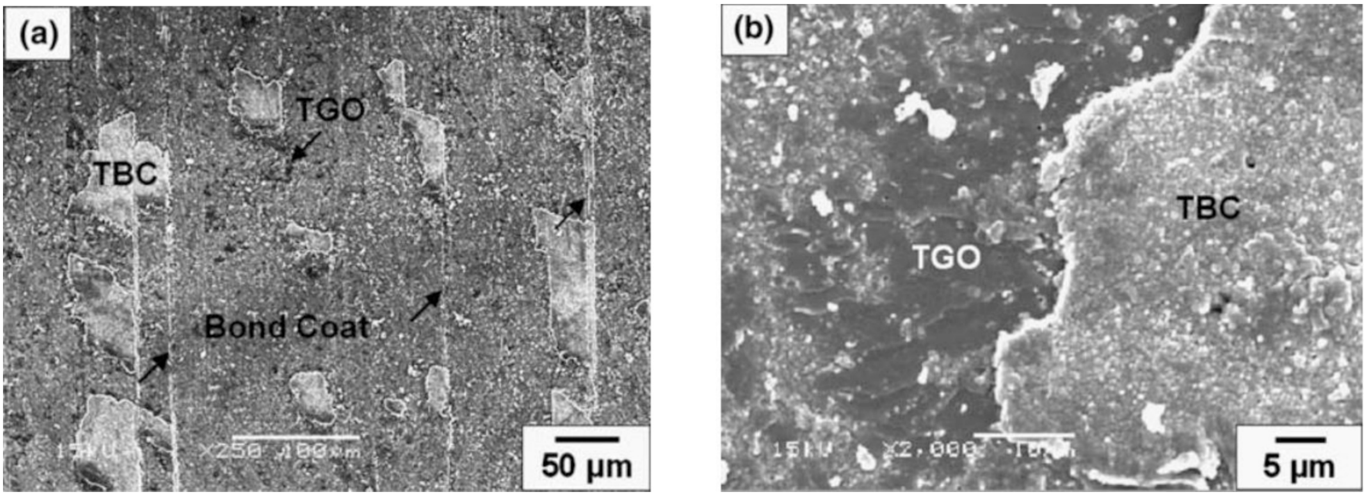

Fig. 55. SEM micrographs of the fracture surface on the metallic substrate side exposed by the delamination of the TBC layer in the EB-PVD TBC system: (a) a low-magnification image revealing characteristics of the crack growth and failure surface and (b) a high-magnification image showing embedded thermally grown oxides in the bond coat and the existence of thin layers of TBC remaining adhered to the TGO segments [132].

were included to improve the barb pull out test for determining the mixed-mode I/II fracture toughness in thermal barrier coatings along with analytical and numerical approaches [134].

The mixed-mode I/II steady-state energy release rate G was determined by,

$$G = \frac{h_2}{2\overline{E}_2}\cdot\left[\sigma_a + \frac{\Delta\alpha\Delta T}{1/\overline{E}_1\eta + 1/\overline{E}_2}\right]^2 + \frac{h_1}{2\overline{E}_1}\cdot\left[-\frac{1}{\eta}\sigma_a - \frac{\Delta\alpha\Delta T}{\eta/\overline{E}_2 + 1/\overline{E}_1}\right]^2 \tag{23}$$

where σ_a is the applied stress, h_1 and h_2 are the thicknesses of coating and the substrate respectively, $\overline{E}_1$ and $\overline{E}_2$ are the elastic modulus in plain strain condition of coating and substrate respectively, $\Delta\alpha$ and ΔT are defined as thermal expansion coefficient and the change in temperature, respectively. The value of $\Delta\alpha$ was determined from the elastic mismatch of the coating and the substrate, where $\Delta\alpha = \alpha_1^* - \alpha_2^*$; with $\alpha_i^* = (1+\upsilon_i)\cdot\alpha_i$, with $\alpha_i (i = 1, 2)$. The finite element method (FEM) was implemented to evaluate the strain energy release rates and phase angles of the delamination crack for different specimen geometries [135]. In addition, the stress distributions in thermal barrier coatings were also analyzed by FEM in barb pullout tests [136].

The key benefits of this method are that it can generate mixed-mode ratios and is applicable for both notched and unnotched specimens. An additional advantage is the applicability for both short and long crack length specimens. Further advantage is the availability of closed-form analytical formulation. However, the downsides of this test are complicated fabrication of the specimen requiring the alignment of both sides of the coating with the test fixture. Another disadvantage is the indirect calculation of the phase angles requiring numerical simulation to find the mode I and mode II stress intensity factors.

4.1.7. *Pushout test*

Though the barb pullout test is able to generate some mode II fracture toughness contribution, it is not able to provide a pure mode II fracture toughness. Thus, this subsection describes the push out method to estimate the interfacial fracture toughness (mode II) in pure shear loading conditions. Here, the pushout test is described along with the schematics of the test geometry, microstructure of the specimens, SEM micrographs of fractured surface after the test, benefits and limitations.

The pushout test was introduced in fiber-reinforced composites. This test methodology, see Fig. 56 and Fig. 57 was adopted to calculate the interfacial shear properties [137] and the influence of different thermal cycling temperatures (1000, 1025, 1050, 1100) °C on delamination toughness in electron-beam physical vapor deposited (EB-PVD) thermal barrier coatings [138]. The investigated thermal barrier coating was comprised of a ~ 500 µm thick 8 wt.% Y_2O_3-ZrO_2 (8YSZ) layer, a 150 µm thick bond coat layer of CoNiCrAlY and a 3 mm thick Inconel 738 LC Ni-base super-alloy substrate. The pushout test was performed by employing a screw-driven type testing machine with a constant cross-head displacement rate of 0.1 mm/min [137] and 0.01 mm/min [138]. The applied load–displacement responses were continuously stored by a digital memory scope with a sampling time of 5 ms. The AE event counts were monitored by an acoustic emission (AE) tester.

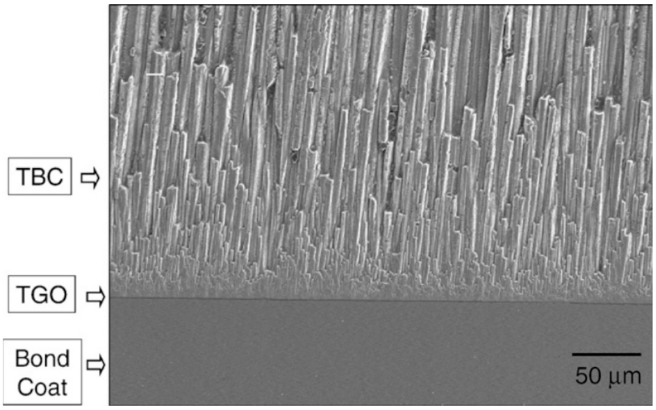

Fig. 56. A typical example of the polished transverse section of as deposited EB-PVD TBC system [137].

The SEM images of fracture surface of the specimen after the pushout test and a focused ion beam (FIB) cross section are displayed in Fig. 58 and Fig. 59. The pushout test was developed to determine the interfacial fracture toughness K in terms of shear loading conditions and was calculated by,

$$K \approx \frac{(\sigma_{tbc})^2 h_{tbc}}{2E^*_{tbc}} + \frac{(\sigma_{tgo})^2 h_{tgo}}{2E^*_{tgo}} + \frac{(\sigma_s)^2 h_s}{2E^*_s} + \Gamma_b \tag{24}$$

where σ_{tbc}, σ_{tgo} and σ_s are the in-plane stresses of the TBC layer, the TGO layer and the substrate, respectively and Γ_b is the contribution of the bending moment to the interface toughness. The detailed expression of the above-mentioned terms is described in Ref. [137].

The key strengths of the pushout test are simple test setup and specimen geometry. Further advantages are the suitability of small TBC

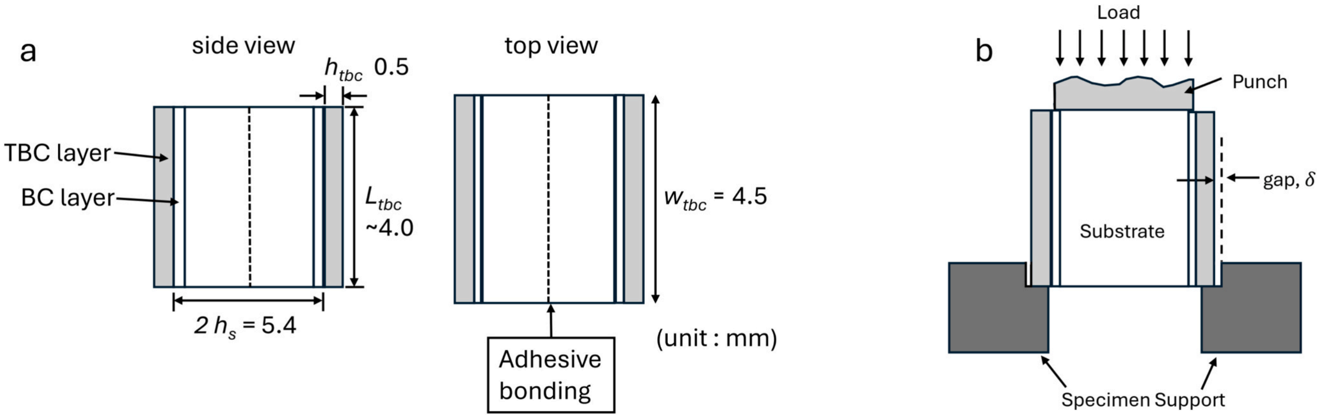

Fig. 57. (a) Shape and dimensions of the specimen for pushout test and (b) schematic illustration of loading geometry and applied force direction (adopted from Ref. [137]).

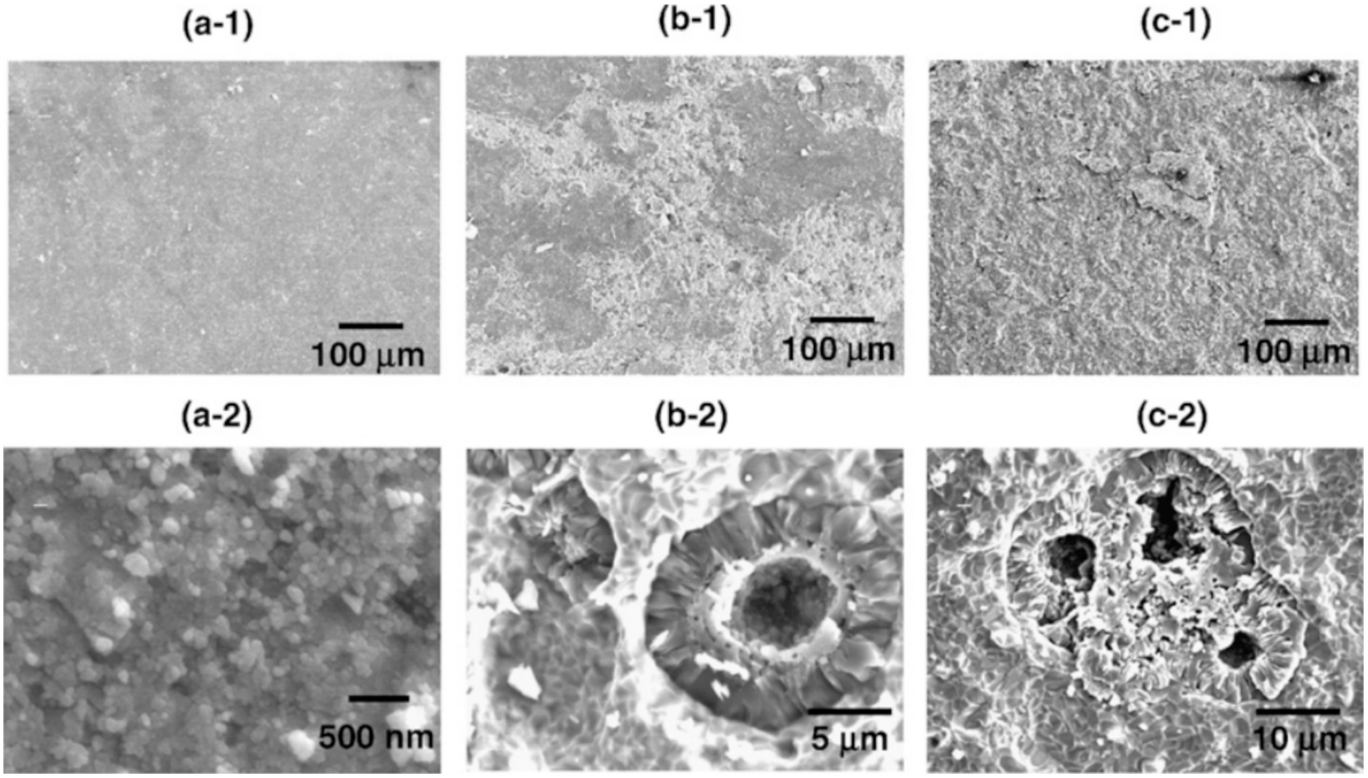

Fig. 58. Fracture surface morphology observed on pushout tested substrate side of specimens: (a-1, a-2) as-deposited, (b-1, b-2) $t_h = 50$ h and (c-1, c-2) $t_h = 200$ h [137].

coated specimens and providing crack growth behavior in shear loading conditions. Furthermore, the test offers a quantitative assessment of interfacial delamination toughness Γ_i. The major drawback of this test is providing only the mode II interfacial fracture toughness, where the delamination toughness strongly depends on the delamination path [137]. Therefore, proper delamination path tracking, and post processing are required to evaluate the actual interfacial toughness values.

4.1.8. *Mixed-mode test*

As the coating to substrate is a bi-material system, the interface between the coating and substrate is exposed to mixed-mode failure in real life conditions. Thus, in this subsection apart from the indentation, bending and barb pull out tests, two additional mixed-mode tests are introduced. These tests are described along with the schematics of the specimens, the test setups, benefits and drawbacks.

The first type of mixed-mode test, a biaxial fracture test device was developed to measure the mixed-mode I/II interfacial fracture toughness in thermal barrier coatings, see Fig. 60 and Fig. 61 [139]. In that study, the investigated tested TBC system was comprised of 8 wt% Y_2O_3–ZrO_2/CoNiCrAlY/IN738LC. A 1.0 mm thick 8 wt.% Y_2O_3–ZrO_2 layer and a 0.1 mm thick CoNiCrAlY alloy layer was sprayed by an atmospheric plasma spray (APS) process on a substrate of IN738LC having dimensions of 2 × 100 × 100 mm^3. The substrate of the extracted specimen from the coated plate had dimensions of 40 × 4 × 2 mm^3. A pre-crack was created by a diameter cutter having lengths of 10 to 20 mm and thickness of 0.1 mm inside the specimen. For performing the tests, two stiff load cells were employed to measure the compressive load P and slinging load Q. Displacement transducers such as strain-gauge were also connected to the linear guide spindle to apply the loads on the specimen. The measured load and displacement data were recorded by the transducers

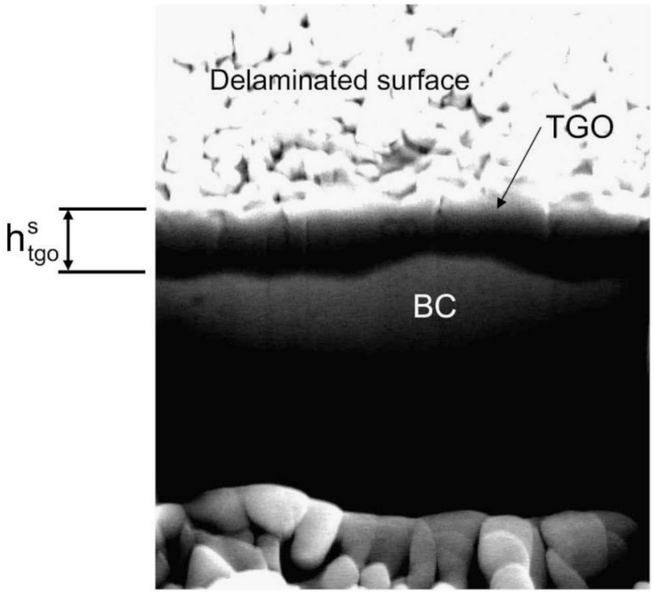

Fig. 59. SEM micrograph of a FIB section, showing the TGO layer thickness on the substrate side, h^s_{tgo} exposed by the delamination of the TBC layer (at $T_h = 1100\ ^\circ\mathrm{C}$) [138].

on a PC computer through an A/D converter. Additionally, the interfacial crack length during the test was monitored by a digital microscope.

The crack initiation, propagation and the spallation of the ceramic coating is depicted in Fig. 62. The proposed test method was also carried out to understand the effect of the high temperature exposure on the interfacial fracture toughness in thermal barrier coatings [140]. This mixed-mode test method has some notable advantages. It provides different mixed-mode ratios, which means a wide range of phase angles. Further benefit is the availability of the closed-form analytical solutions for energy release rates. In addition, crack monitoring is possible with a digital microscope. Despite having significant advantages, the key weakness is the complexity of the test setup. The test setup requires two types of loading fixtures (tensile and compressive loads).

In another study, a new test method combining compressive load and peeling load was performed to determine the interfacial fracture toughness in air plasma sprayed thermal barrier coatings for a wide range of mode mixtures, as presented in Fig. 63 and Fig. 64 [141]. The studied thermal coating system was comprised of a 0.15 mm thick NiCoCrAlY (Ni-22.8Co-17.42Cr-12.1Al-0.48Y,wt.%) bond coat, a 0.3 mm thick air plasma sprayed ceramic top coat of ZrO_2-8 wt.% Y_2O_3 and a Ni-based super-alloy DZ125 substrate having dimensions of 4 × 10 × 70 mm^3. A 4 mm thick steel stiffener was glued on the ceramic topcoat to increase the stored energy by suppressing cracking of it. Additionally, a 29 mm pre-crack was introduced by the wire-cut method along the interface between the ceramic topcoat and the bond coat. The force–displacement data were recorded during the test, where maximum

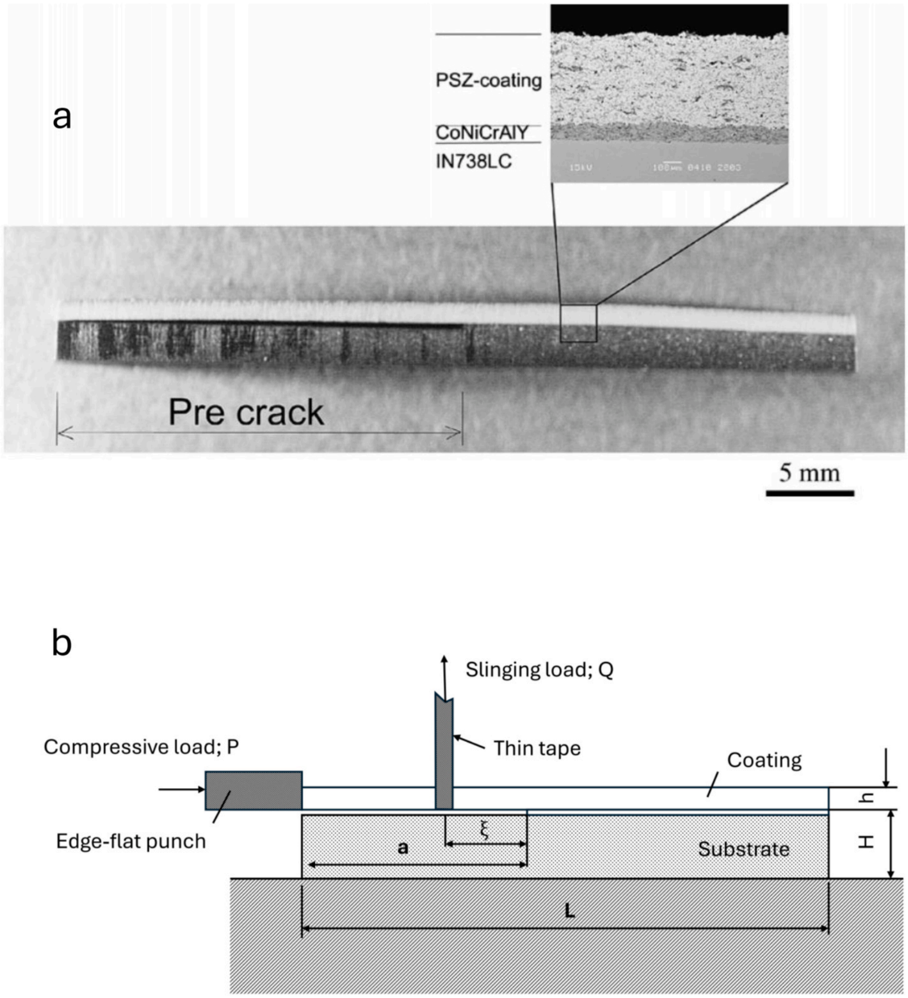

Fig. 60. (a) Aspect of TBC specimen with pre-interfacial crack that was processed by a diamond cutter, (b) Mixed-mode interfacial fracture testing method by combination of compressive load applied by edge-flat punch and slinging load by thin tape hooked in coating beam (adopted from Ref. [139]).

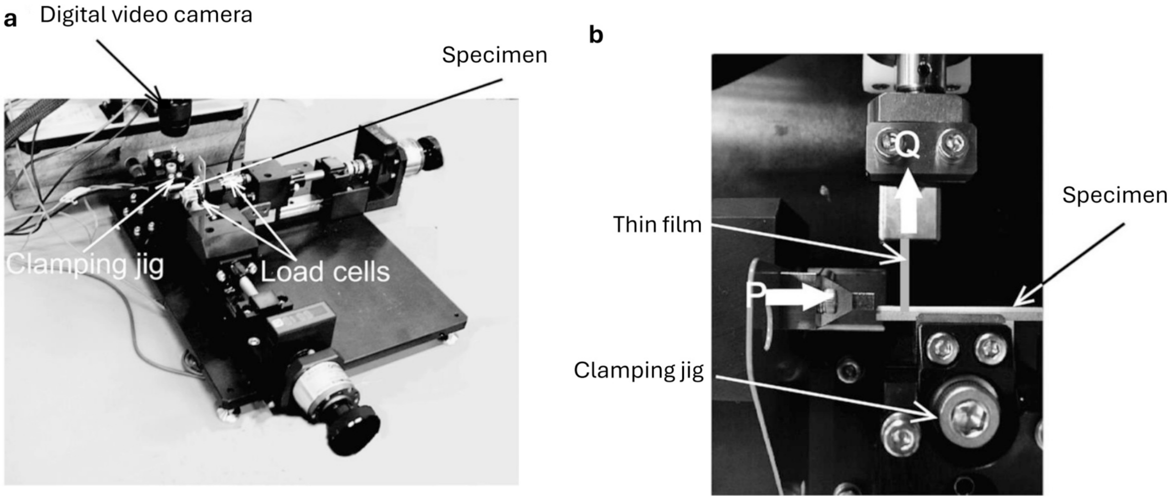

Fig. 61. Mixed-mode loading device developed in this study. (a) An appearance of mixed-mode loading device, (b) Magnified picture around loading part [139].

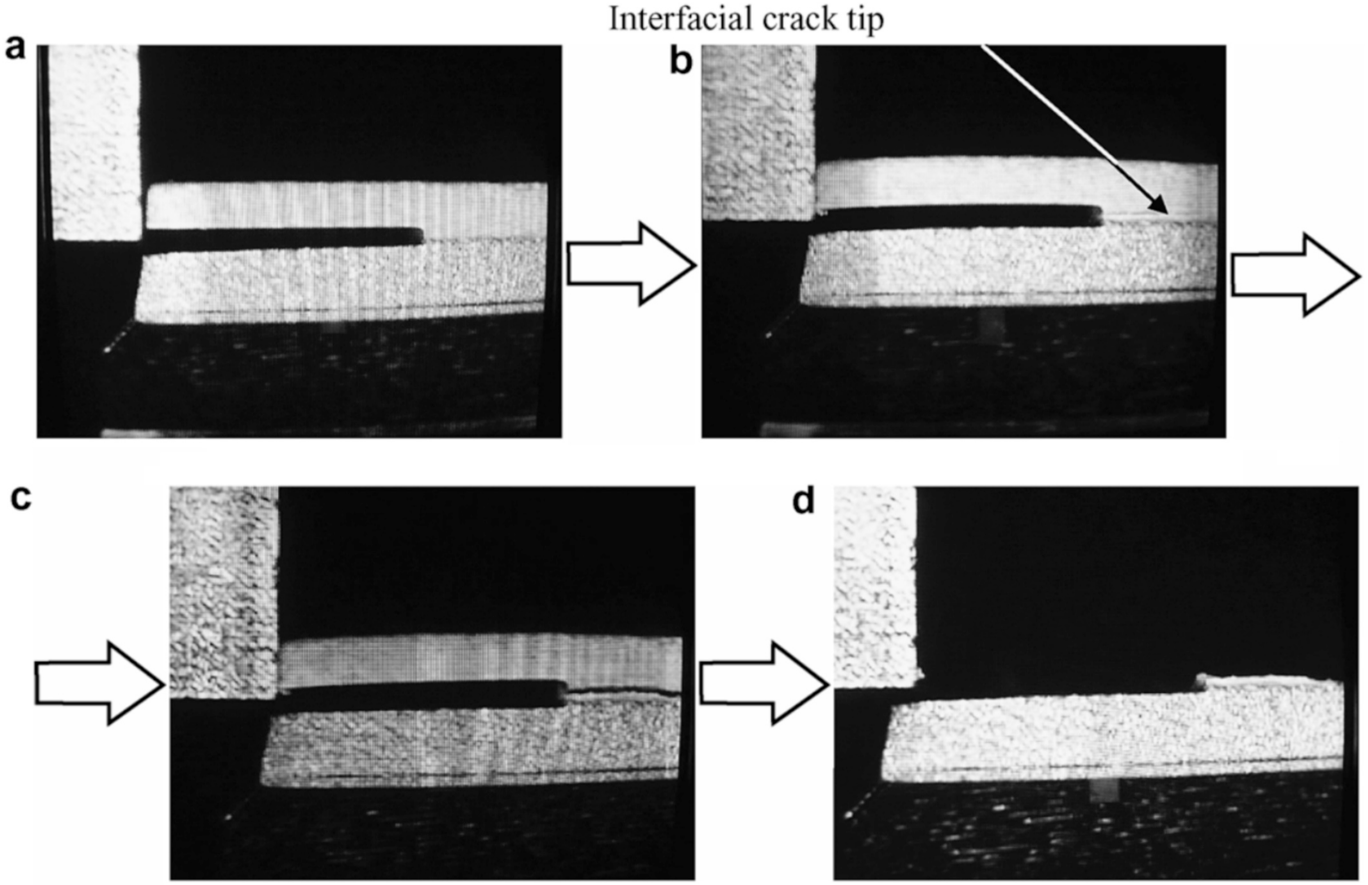

Fig. 62. Continuous observation result of interfacial crack initiation and propagation process observed by digital microscope: (a) initial state, (b) initial crack, (c) crack propagation and (d) spalling [139].

force F_{max} was considered as the critical force F_c due to the onset of the ceramic layer delamination to bond coat and applied to calculate the critical energy release rate and critical stress intensity factors.

The key strengths of this mixed-mode test are that it offers a wide range of mode-mixtures and is applicable for both thin and thick multilayered coatings. Moreover, the test can be carried out at both room and elevated temperatures [141]. Further advantages are the presence of a closed form analytical solution and an elliptical interfacial failure criterion based on stress intensity factor. Despite having significant advantages, the downsides of this method are difficulty of performing the test, the complexity of test setup due to having two loading features and complicated post processing i.e. numerical analysis is required to find the contribution of mode I and mode II fracture toughness.

4.1.9. *Further test methods*

Apart from the above-mentioned tests to determine the interfacial fracture toughness, there are other methods which are performed to

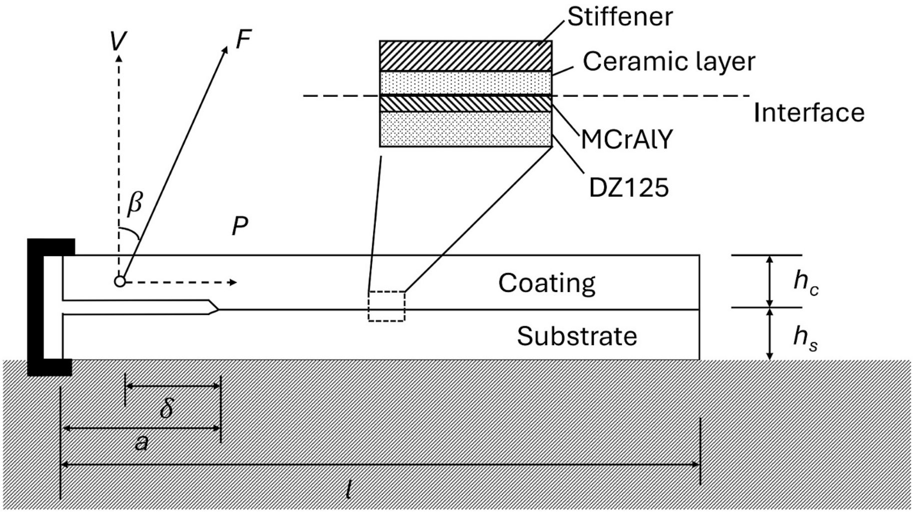

Fig. 63. A schematic diagram of interfacial fracture toughness test (adopted from Ref. [141]).

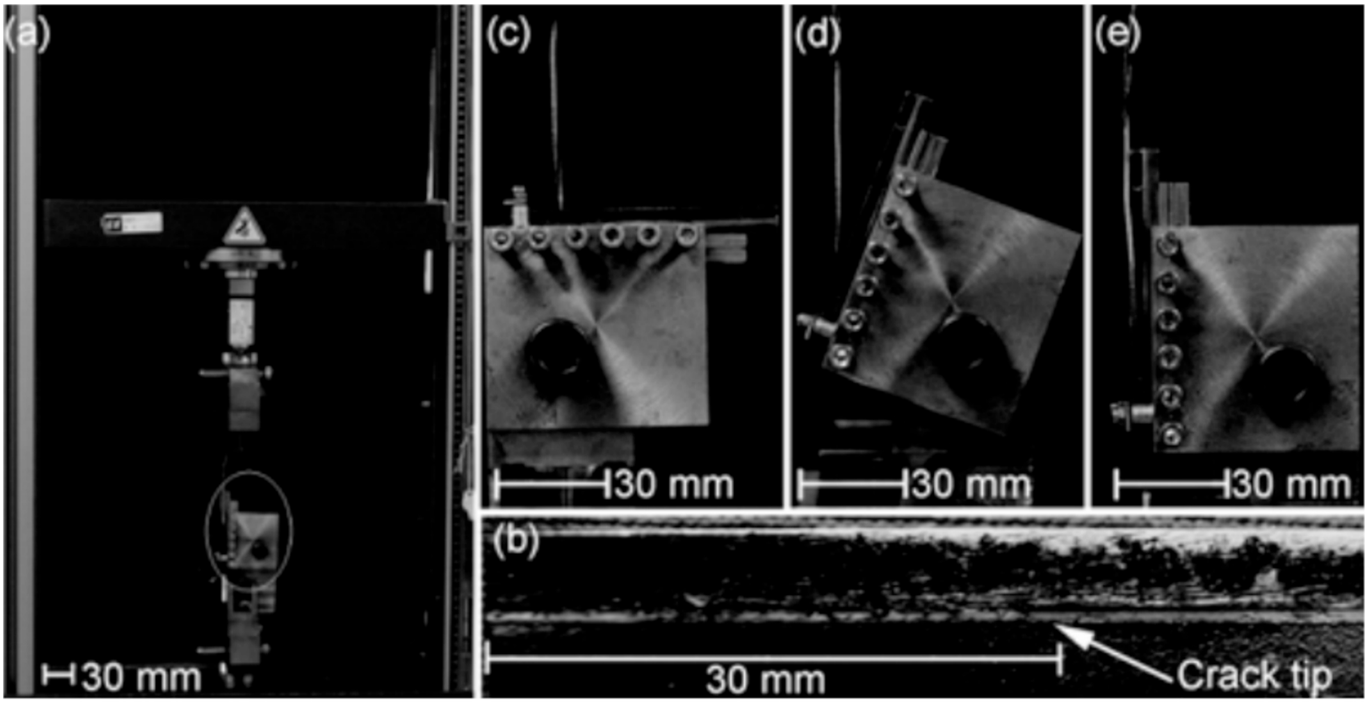

Fig. 64. (a) Mixed-mode fracture test; (b) specimen with stiffener and an interfacial crack; (c), (d), (e) tests with loading angles β = 0°, β = 75° and β = 90°, respectively [141].

evaluate the interfacial fracture toughness between the coatings and the substrate.

Further test methods such as blister tests were performed to evaluate the interfacial fracture toughness in thermal barrier coatings [142] and spallation failure characteristics in EB-PVD thermal barrier coatings [143]. The driving forces of blistering were studied by Laser Shock Adhesion Test (LASAT) method [144]. In-situ tests such as micro-cantilever test [145,146] and micro-cantilever bending test [147] were implemented to determine the mechanical properties such as elastic modulus and mode I (K_{Ic}) fracture toughness of air plasma sprayed thermal barrier coatings. The double torsion test was carried out for determining the mode I (K_{Ic}) fracture toughness of porous atmospheric plasma sprayed (APS) thermal barrier coatings [148] and anode substrates of solid oxide cells [149]. Interfacial properties of two flame-sprayed yttria-stabilized zirconia TBCs were evaluated in terms of mode II (G_{IIc}) fracture energy and stress intensity factor (K_{IIc}) by a steel blade driven shear test and inverse finite element method [150]. The uniaxial tension test was introduced to investigate the interfacial fracture properties of two-layer (non-functionally graded material) plasma-sprayed TBC on a stainless steel (SUS304) substrate [151]. The fracture characteristics of air-plasma-sprayed thermal barrier coatings (TBC) at different conditions such as without TBC, as-sprayed and peroxidized were studied with tensile test specimens and postprocessed from the patterns of acoustic emission (AE) method. The stress–strain curves were reported for the specimens of three conditions, but no fracture toughness of the TBC was reported [152]. In another study, the adhesion strength of ceramic topcoat in plasma-sprayed thermal barrier coatings (TBC) exposed to thermal exposures was investigated by tensile testing but no interfacial fracture toughness was reported either [153]. The influence of the roughness of the bond coat on the adhesion of thermal barrier

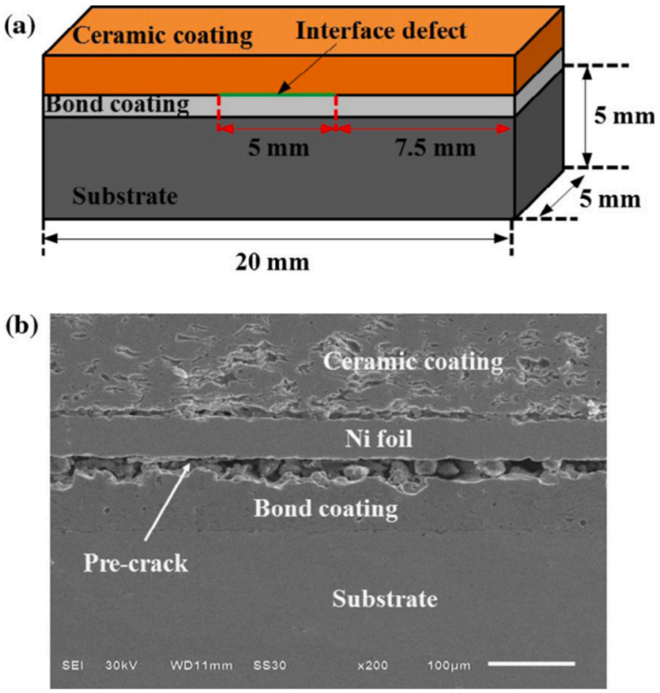

Fig. 65. (a) Schematic of a TBC specimen with an interface defect and (b) a typical cross-section image observed by scanning electron microscopy [158].

coatings deposited by electron beam physical vapor process was studied by tensile testing. In that study, no interfacial fracture toughness was determined [154]. In another study, tensile tests were performed to investigate the impact of different types of interfacial texture of 8YSZ TBCs under thermal cycling loadings. The delamination toughness at the interface was calculated by simulating the thermal shock conditions in a muffle furnace at 800 °C for 12 h [155]. An in-situ one point load flexure test was performed to evaluate the interfacial delamination toughness between the thermally grown oxide (TGO) layer and bond coat in thermal barrier coatings [156]. In another study, a buckling test setup prone to compressive strain was developed to the Ni-3YSZ anodes of solid oxide fuels to determine the fracture toughness. No interfacial fracture toughness between anode and substrate was determined. Only total fracture toughness of the anodes was evaluated [157].

A new novel compression test was developed along with the cohesive zone model to determine the interfacial fracture energy in TBCs, see Fig. 65 [158]. The investigated TBC was comprised of a 5 mm thick Ni-based super-alloy substrate, a 100 μm thick $NiCr_{22}Al_7Y_{0.2}$ bondcoat, a 350 μm thick YSZ topcoat and a nickel foil of 40 μm in thickness as an interfacial defect.

The compression tests were carried out with a universal testing machine at room temperature. As displayed in Fig. 66, a pancake indenter was applied to impress through one end of the specimen, where compression was along the direction parallel to the film/substrate interface. The applied loading rate was 250 N/min. Buckling and delamination of TBCs were monitored during compression by using an acoustic emission (AE) system and a charge-coupled device (CCD) camera. The AE sensor was placed on the surface of substrate. The CCD camera, equipped with a lens of 50 mm focal length, was put in front of the cross-section of the specimen to in-situ record the buckling and delamination process with a sampling rate of one image per second.

The advantages of the compression test are that the specimen preparation is simple. The test setup and test procedure are not complex. An additional benefit of the compression test is that the crack can be monitored by CCD camera and the in-situ failure can be captured by AE method. However, finite element simulation is required to determine the mixed mode fracture toughness and mixed-mode phase angle.

In a study, a uniaxial compression test was developed to quantify the damage mechanisms at the interface between the topcoat and bondcoat in EB-PVD TBCs. The damage phenomenon was characterized by the critical compressive strain causing the spallation of the TBCs. However, no interfacial fracture toughness was measured [159]. In a recent study, a compression test was performed to investigate the damage mechanism and corrosion resistance mechanism under CMAS corrosion environment in EB-PVD TBCs. A buckling theory depending on the critical compressive strain was employed to analyze the spallation of the TBCs. No interfacial fracture toughness was calculated in that study [160].

4.2. Tests at elevated temperatures

Testing at elevated temperatures is challenging. However, efforts are made to perform interfacial fracture toughness tests in ceramic coatings at elevated temperatures. In this subsection, high temperature test methods for interfacial fracture toughness in ceramic coatings are reviewed.

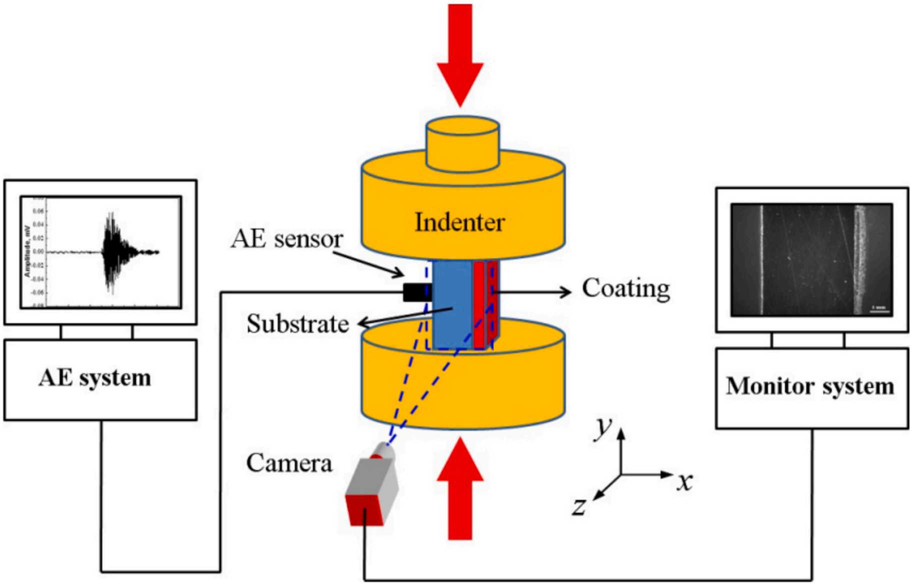

Fig. 66. Illustration of compression tests with AE and CCD camera monitoring systems [158].

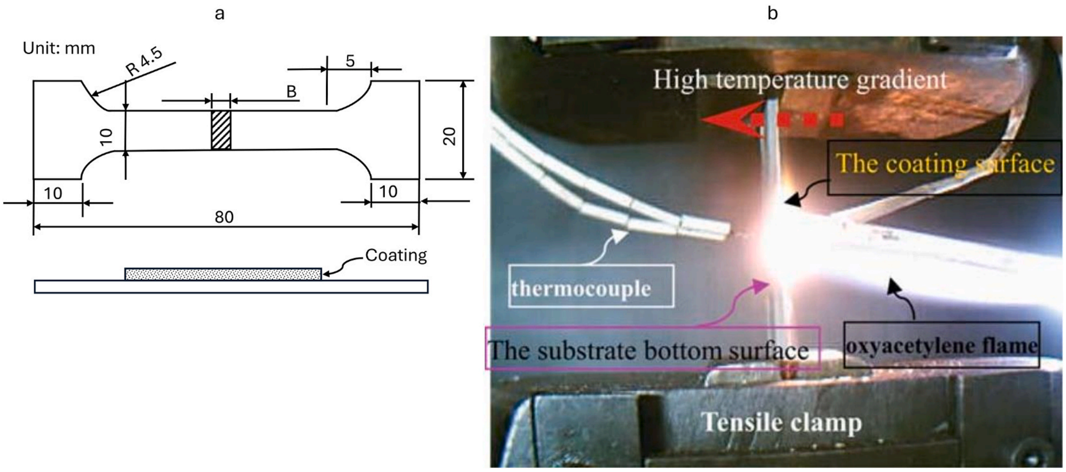

Fig. 67. (a) Dimensions of TBC specimens in the uniaxial tensile test (adopted from Ref. [161]); (b) the tensile test setup of thermal barrier coating system at 1000 °C [161].

4.2.1. *Tensile testing*

Tensile tests are performed mostly to calculate the strength of the materials. In this subsection, tensile testing is described to determine the interfacial fracture toughness between coating and substrate at elevated temperature along with schematic of specimen geometry, test setup, microstructure, advantages and disadvantages.

An in-situ uniaxial tensile test was carried out in plasma sprayed topcoat thermal barrier coatings to determine the mixed-mode I/II interfacial fracture toughness between the topcoat and the bond coat at 1000 °C, see Fig. 67 [161]. In that study, the investigated thermal barrier coating system was comprised of plasma sprayed ZrO_2–8 wt.% Y_2O_3 (YSZ) TC having thicknesses of 200 μm, 300 μm and 400 μm, a 100 μm thick NiCrAlY bond coat and a 1.8 mm thick SUS304 stainless steel substrate. A thermo-mechanical test setup was applied to perform the test where an oxyacetylene torch was used to heat only the surface of the ceramic coating up to 1000 °C. The temperature of the top surface of the ceramic coating (T_1), the bottom surface temperature of the substrate (T_2) and the cross-section temperature of the TBCs specimen (T_3) were measured by three thermo-couples. A constant displacement rate of 2.00 mm/min was applied for the tensile force until the spallation of the ceramic coating completely occurred. Additionally, the interfacial crack nucleation, propagation, and coating spallation were monitored by a miniature testing device and a high accuracy camera. For evaluating the fracture toughness, the critical force data and temperature gradient were recorded.

The optical images of the fracture process of a thermal barrier coating due to thermo-mechanical loading at high temperature is presented in Fig. 68. The morphology of the fractured specimens in scanning electron microscope is provided in Fig. 69. The interfacial fracture energy and toughness between the topcoat and the bond coat were evaluated from the formulation in Ref. [50].

The advantage of this test method is that it is suitable for in-situ high temperature tests. Additionally, crack nucleation, propagation and spallation in the coatings are monitored by the high-performance camera. Furthermore, a closed form solution for total fracture energy is provided and the specimen geometry as well as specimen preparation is

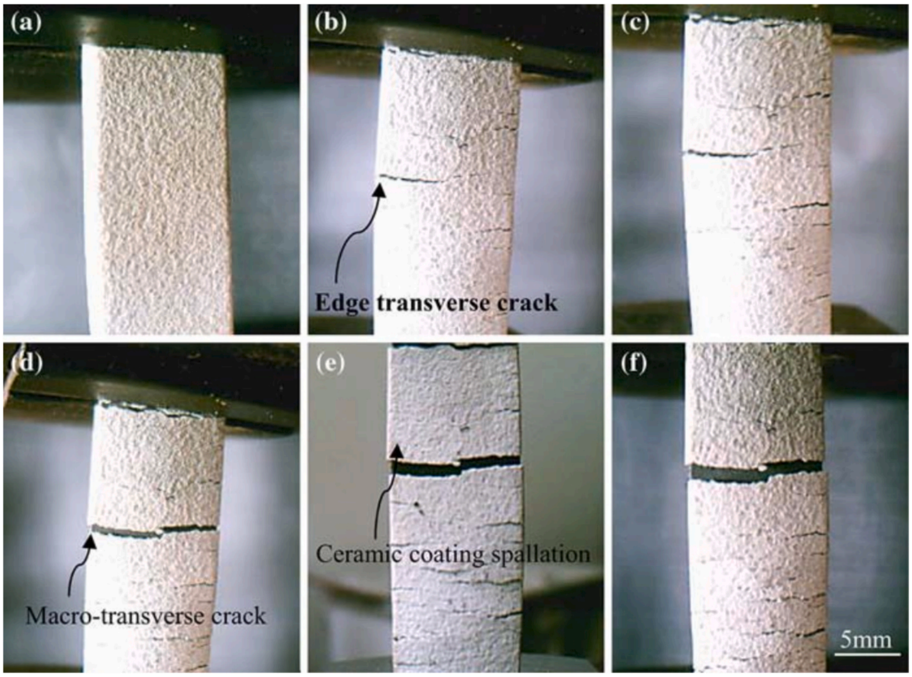

Fig. 68. The fracture/spallation process of the TBC specimen under thermo-mechanical tensile loading at high temperature [161].

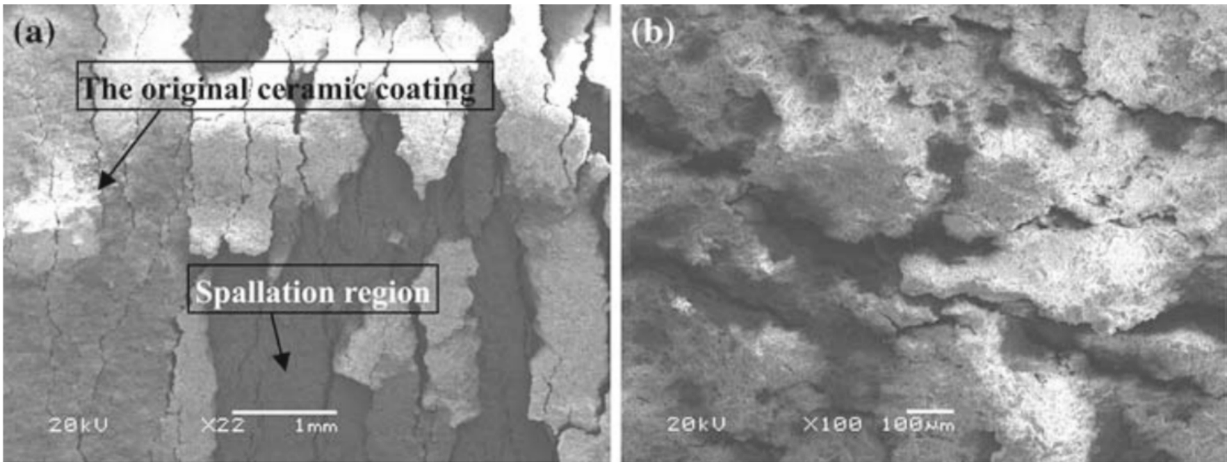

Fig. 69. SEM micrographs of the fracture morphology of (a) the TBC specimen surface and (b) its spalled fragment after thermo-mechanical tensile tests [161].

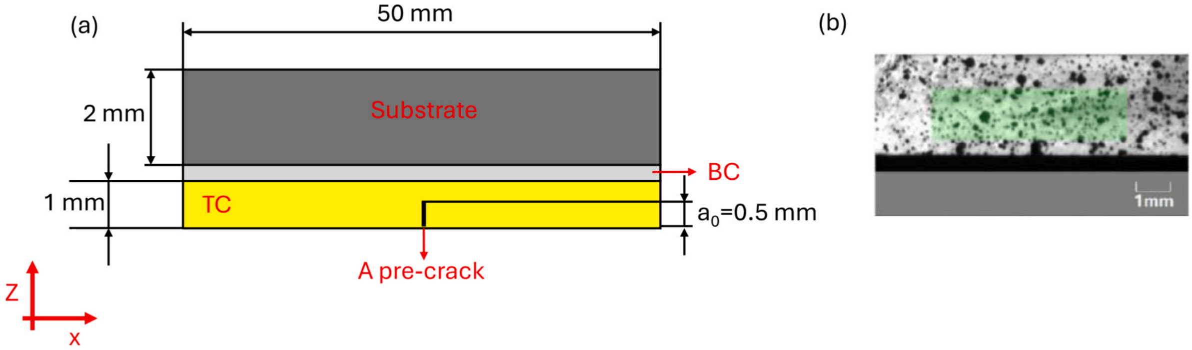

Fig. 70. (a) Schematic of a TBCs specimen with a pre-crack (adopted from Ref. [162]); (b) speckle patterns of a cross section of TBCs, in which the green zone is the strain measurement zone [162].

simple. However, one major drawback of this test method is the generation of multiple cracks and multiple crack propagation. The multiple crack propagation makes the accurate evaluation of interfacial fracture toughness difficult.

4.2.2. *Flexural test*

Apart from the tensile testing, efforts are also made to perform the flexural tests at elevated temperatures. In this subsection, three-point and four-point flexural tests carried out at elevated temperatures along with schematics, test setups, advantages and disadvantages are discussed.

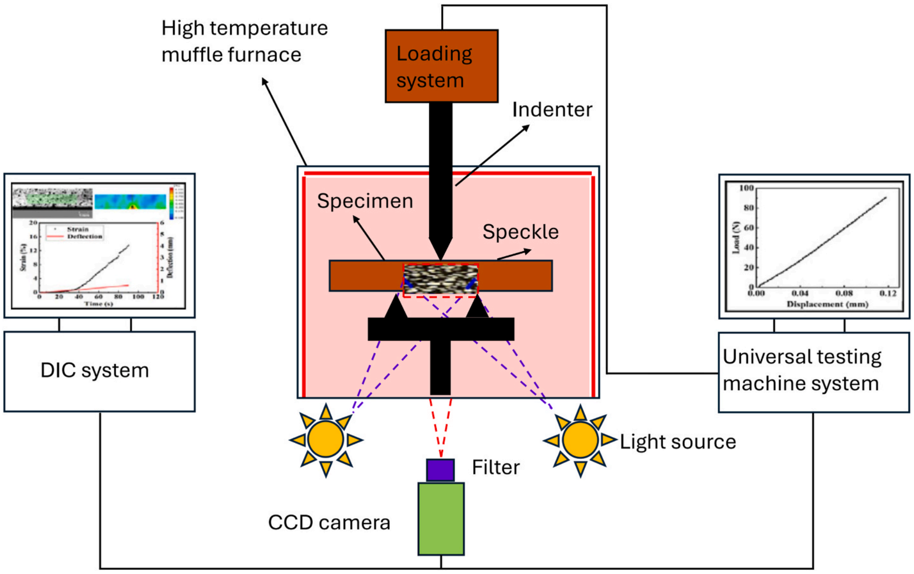

Fig. 71. The schematic of high temperature three-point bending test with DIC system (adopted from Ref. [162]).

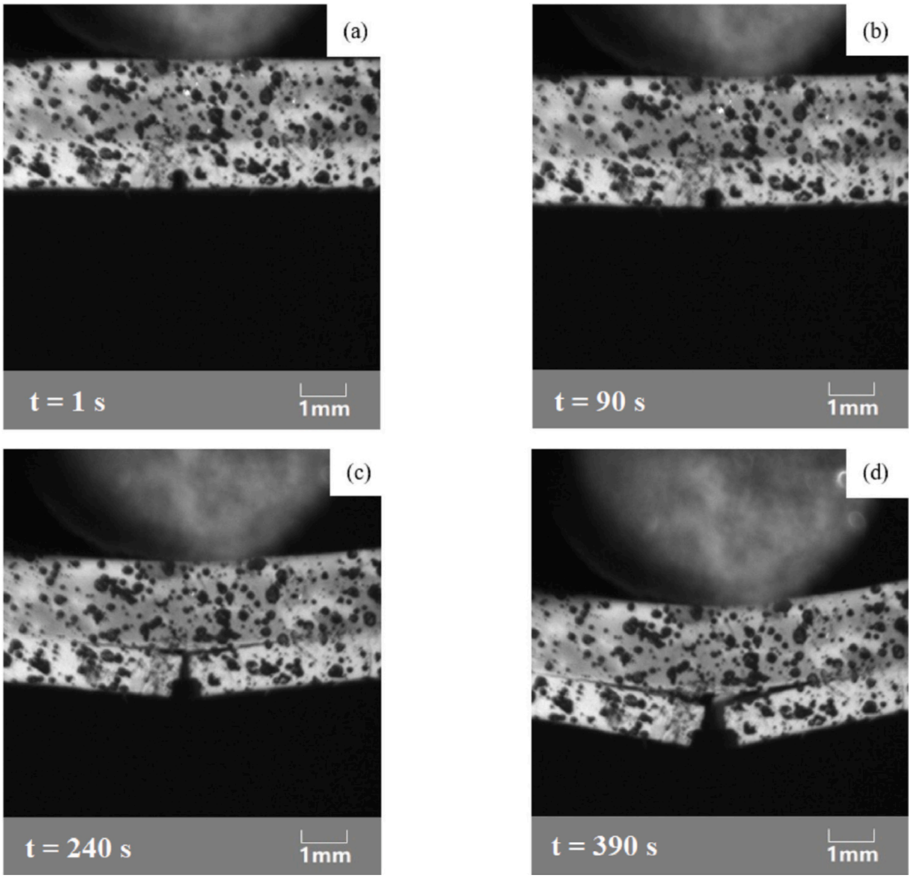

Fig. 72. The process of crack initiation and propagation observed by DIC at the room temperature (30 °C): (a) Initial state; (b) the initiation of surface crack; (c) the initiation of interfacial crack between TC and BC and (d) the propagation of interfacial crack [162].

An in-situ three-point flexural test combined with digital image correlation (DIC) was introduced to determine the elastic modulus, fracture toughness and mode I interfacial toughness of thermal barrier coating from the temperature of 30–800 °C, as illustrated in Fig. 70 and Fig. 71 [162]. In that study, the investigated thermal barrier coating system was comprised of a 1 mm thick air plasma sprayed 8YSZ top coat, an 80 μm thick NiCoCrAlY bond coat and a 2 mm thick Ni-based alloy substrate (GH536). The tested specimens had dimensions of 50 × 6 mm^2 for elastic modulus measurement of TC and substrate. A 0.5 mm depth groove was cut in the middle of TC as a pre-crack. For carrying out the test, the high temperature environment was generated by a muffle furnace. The temperatures near the specimen were measured by thermocouples. The crack and deformation of the specimen was monitored by a DIC system.

The real time process for crack initiation and propagation of the surface and the interfacial crack initiated by bending test at temperature of 30 °C was monitored by the DIC method, as presented in Fig. 72. The interfacial fracture toughness was calculated by the formulation according to Ref. [120]. This in-situ three-point bending test overcomes the challenge of evaluating the interfacial toughness at elevated temperatures. This method has key benefits such as monitoring the crack with a DIC system and easy post processing through the compliance calibration method. An additional advantage is the availability of a closed form solution to calculate interfacial fracture toughness. Further advantage is no numerical analysis necessary to evaluate the interfacial fracture toughness.

Although this method overcomes certain challenges, it only offers the total interfacial fracture toughness. But in real scenarios, at the interface mixed-mode loadings are present. Thus, the contribution of mode I stress intensity factor (K_{IIc}) and mode II stress intensity factor (K_{IIc}) should be investigated. Further drawbacks are the complex fabrication of the specimen requiring a well-positioned pre-crack for crack propagation at the interface and the complicated test setup requiring a DIC system and a muffle furnace.

Recently, two types of four-point flexure tests were developed at elevated temperatures to measure the interfacial fracture toughness. In the first type of test, a four-point flexural test, as displayed in Fig. 73 were performed on CMC/EBC systems at room temperature and at 1000 °C in a furnace using full field measurements to determine the interfacial energy release rate [163,164].

The above mentioned four-point flexural method overcomes the challenges of testing the interfacial properties of environmental barrier coatings at elevated temperatures. Despite resolving the challenge to perform the tests at elevated temperatures, the notable weaknesses of this test are the complicated test setup and testing environment. The test setup requires the employment of a DIC method. In addition to it, the testing condition is harsh because of testing at elevated temperatures. Further weakness of this test is that the method only offers the total interfacial energy release rate not the contribution of mode I and mode II crack intensity factors, which are necessary for the proper evaluation of the results. Moreover, finite element method (FEM) is required for the validation of the experimental results, which is not cost effective.

The other type of test where a four-point flexure test using CO_2 laser heating system, see Fig. 74 was implemented to investigate the fracture mechanisms of EBC/CMC system [165]. An yttrium disilicate ($Y_2Si_2O_7$) topcoat was deposited by thermal spray on a SiC/SiC composite. The impact of test parameters such as mechanical loading level, temperature level, and EBC thickness on the crack network, shape and depth were analyzed.

This test method provides advantages such as in-situ crack

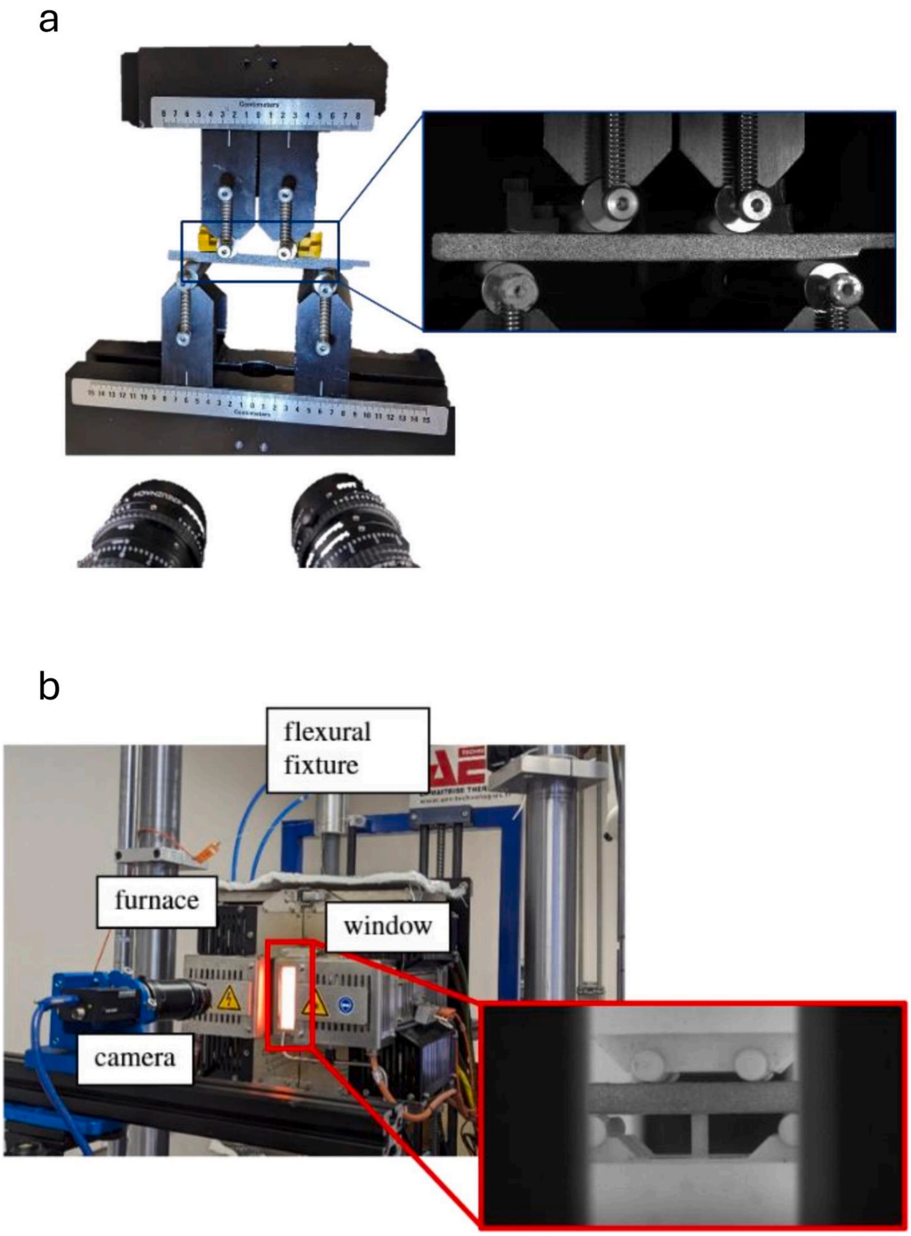

Fig. 73. Four-point flexural setups with the associated instrumentation (a) at room and (b) at high temperatures [163].

monitoring using acoustic emission sensors and is suitable for high temperature testing. Additionally, the specimen preparation and the test setup are less complicated. However, no interfacial fracture toughness can be estimated with this method as the vertical cracks do not develop any delamination at the interface of EBC/CMC.

4.2.3. *Indentation test*

Different types of indentation tests were implemented to determine the interfacial facture toughness at room temperature which are described in subsection 4.1.3. Apart from tensile and bending tests mentioned above, efforts are also made to determine the interfacial fracture toughness using indentation tests at elevated temperatures. Thus, in this subsection, indentation tests conducted at elevated temperatures to calculate the interfacial fracture toughness along with schematics, test setup, advantages and disadvantages are discussed.

A diamond Berkovich nanoindenter was applied to calculate the mechanical properties of 8YSZ thermal barrier coatings at temperatures of 250 and 450 °C [166]. The method was performed to measure the hardness H, elastic modulus E and fracture toughness K_c of the TBC. The investigated thermal barrier coatings were comprised of a nickel base alloy (Inconel 718), a 150 μm thick bond coat and a 400 μm thick top coat. The nanoindentation technique provided the fracture toughness of TBC at intermediate temperatures. But no interfacial fracture toughness was reported.

In another study, an in-situ high temperature digital image correlation (DIC) along with finite element method was introduced to understand the critical delamination and fracture behavior of dense vertically cracked TBCs [167]. In that study, nanoindentation was conducted to determine the elastic modulus E and fracture toughness K_c of top coat up to 1000 °C. No direct interfacial energy release rate was deduced as numerical simulation was required for determining the energy release rate. Furthermore, no interfacial fracture toughness was calculated by using nanoindentation. In another study, the elastic and hardness of 8YSZ topcoat was determined at 25, 1000 and 1200 °C [168]. Afterwards, a high temperature indentation method was developed to determine the fracture toughness considering residual stress of 8 wt% yttria partially stabilized zirconia (YSZ) coating at 25, 800 and 1000 °C. No interfacial fracture toughness was reported using nanoindentation

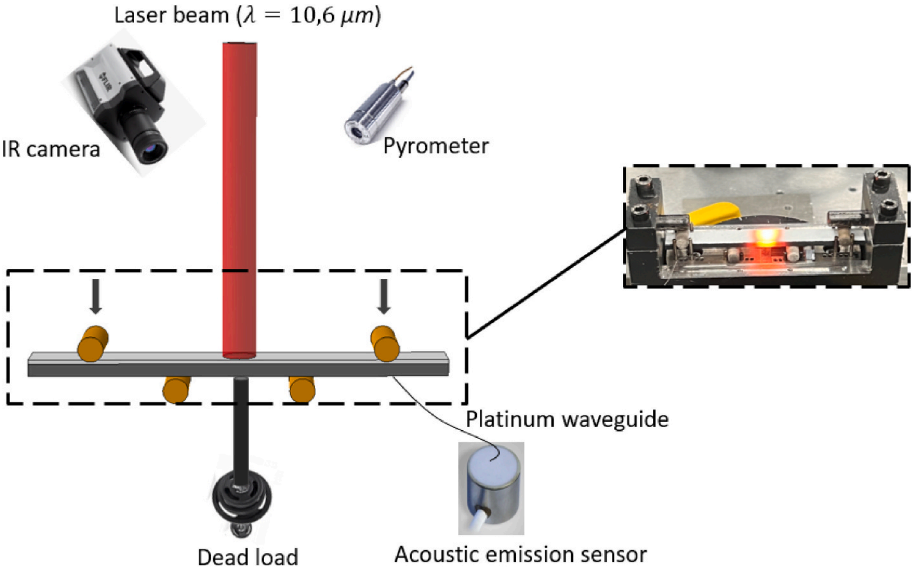

Fig. 74. Experimental setup for 4-point bend test under laser loading [165].

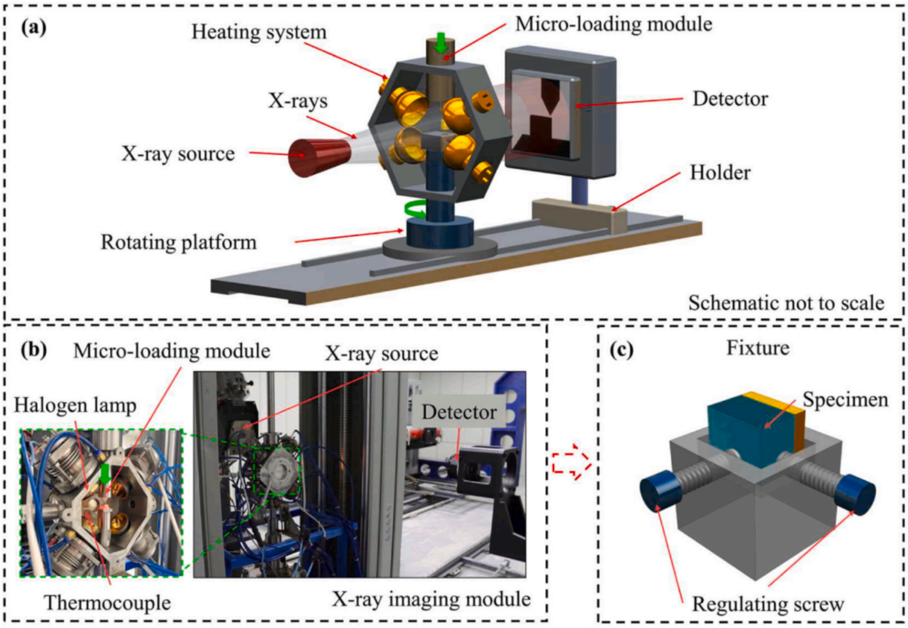

Fig. 75. (a) Schematic of the in-situ HCSI tests, (b) In-situ microtomography apparatus with a laboratory X-ray source, (c) Schematic of the fixture to prevent the specimen from tilting [170].

[169].

Recently, an in-situ indentation method based on X-ray imaging was developed to study the mixed-mode I/II interfacial failure behavior of TBC at RT, 400 °C and 800 °C, as provided in Fig. 75 [170]. The investigated TBC was based on an EB-PVD deposited 8YSZ as the topcoat, a low vacuum pressure plasma sprayed NiCoCrAlY as the bond coat and a Ni-based super-alloy as the substrate.

Though the in-situ indentation high temperature X-ray imaging method overcomes the challenges to determine the interfacial fracture toughness of TBCs at elevated temperatures, this method has several disadvantages such as complex test setup (heating system, rotating platform, micro-loading mode and X-Ray source); complex specimen preparation; expensive test fixture and setup. Moreover, numerical simulation is needed for the verification of the experimental results, which is less cost-effective.

In the above-mentioned test methods for high temperature testing, indentation tests were used to determine the mechanical properties such as elastic modulus and hardness as well as interfacial fracture toughness of the TBCs. A comparative data set to perform the indentation test at elevated temperatures is listed in Table 1.

4.2.4. Further test methods

Apart from the above-mentioned test methods to estimate the interfacial fracture toughness at elevated temperatures, there are other methods which are implemented to evaluate the interfacial fracture behavior of the coating to the substrate systems.

An in-situ acoustic emission (AE) method was performed to analyze the plasma sprayed thermal barrier coatings, which were thermally cycled up to 1150 °C [171]. The investigated thermal barrier coating was comprised of a ZrO_2-12 wt.% Y_2O_3 top ceramic layer of thickness

Table 1
Test data of TBCs for different indentation tests at different temperatures.

Method	Indenter type	Temperature	Indentation load
Nanoindentation [166]	Diamond Berkovich (100 nm edge radius)	250 and 450 °C	100–200 mN
Nanoindentation [167]	Cubic boron nitride (cBN) Berkovich, sapphire Vickers	RT-1000 °C	50, 100 and 500 mN
In-situ indentation [169]	Sapphire Berkovic, cube corner,	RT-1000 °C	3, 80, 100 and 120 N
In-situ Indentation with X-Ray imaging [170]	Sapphire Vickers, cone-shaped diamond indenter (tip radius 0.005 mm and tip angle 90°)	RT-800 °C	3 N

0.49 mm and 0.40 mm, a 0.17 mm thick NiCrA1Y bond coat and a 6 mm thick disk-shaped substrate of U-700 super-alloy with a radius of 13 mm. A platinum (Pt) wave guide was TIG welded to the specimen to place it inside the furnace. The methodology was described for the failure behavior of the coatings in terms of signal counts and accumulative signal count per thermal cycle to distinguish the microcracking and the macro-cracking. In that method, only the failure behavior of the coatings was discussed. There were neither the specific quantitative assessments nor the fracture toughness of the coatings discussed. Furthermore, no interfacial properties of the coatings were evaluated.

In another study, an in-situ fracture toughness of thermally sprayed thermal barrier coatings up to an elevated temperature of 1200 °C was determined by performing acoustic emission (AE) method with laser interferometer [172]. The investigated thermal barrier coating was comprised of a 500 μm thick Al_2O_3 topcoat, a 100 μm thick Ni–Cr–Al–Y bond coat and a SUS304 steel substrate having dimensions of 5 × 15 × 15 mm^3. In that study, an inverse AE method was introduced to calculate the radii of microcracks in the coatings. Additionally, numerical analysis was performed based on the Pop-in fracture model to calculate the radii of the microcracks at different fracture toughness and the initial crack radius at high temperature. Furthermore, a combination of both inverse AE method and numerical model was applied to determine the in-situ fracture toughness of the coatings. Though the test method resolves the problem of locating the exact source of AE signals by laser interferometer, it still requires a mirror to deflect the laser beam to the specimen surface, which might lead to some interference of the AE signal. No direct closed-form solution is defined to evaluate the fracture toughness. Moreover, a numerical analysis is required to calculate the fracture toughness of the coating, which is not cost effective.

It has to be mentioned that mechanical testing at elevated temperatures is always challenging. The drawbacks include complex test setup, maintaining constant temperature distribution throughout specimens, in-situ monitoring, time consuming test procedure, oxidation of the specimens. Furthermore, often vacuum or inert gas conditions are needed to avoid oxidation of specimens. Moreover, if the specimens are small an SEM is needed, which is also a time-consuming procedure. Additionally, specimen heating and cooling down takes time. Thus, testing many specimens is not only expensive but also time-intensive.

Moreover, the thermal effects at elevated temperatures will affect stress intensity factors. To obtain the interfacial fracture toughness, the crack intensity factor needs to be determined. The crack intensity factors are calculated from the contribution of the elastic modulus of the material, stresses and crack length. The elastic modulus can be expressed as a function of temperature according to Ref. [170],

$$E_{(T)} = E_{RT} - CTe^{(T_0/T)} \tag{25}$$

where E_{RT} is the elastic modulus of the coating at room temperature T_0. T is the temperature and C is a fitting constant. Equation 25 provides the relationship between the elastic modulus and temperature. The higher the temperature, the lower is the elastic modulus based on Equation 25. The reason behind the decrease in elastic modulus is due to the brittle to ductile transition at elevated temperatures, see Fig. 76, where the material starts to exhibit plastic deformations, reduced thermal stresses and residual stresses.

The high temperature cross-sectional indentation method concluded that with the increase of temperature, the interfacial fracture toughness decreases. The reason behind the decrease of the interfacial fracture toughness was the weak intercolumn bonding at the YSZ topcoat due to plasticity of the YSZ topcoat at elevated temperature. Thus, the weak intercolumnar microfracture and shear displacement within the YSZ significantly influenced the crack intensity factors and the energy release mechanisms, greatly reducing the strain energy available to drive interfacial cracking [170].

5. Discussion

The above-mentioned test methods are performed to determine the interfacial fracture toughness in multilayered ceramic coatings. Depending on the criteria mentioned in section 4, an overview table of the different test methods is presented in Table 2.

It can be seen that the frequently implemented test methods to evaluate the interfacial fracture toughness in ceramic coatings are indentation tests (macro, micro and nano-indentation), scratch tests (macro, micro and nano-scratch) and flexural tests (three point and four point). These test methods are quite well established and closed-form analytical expressions are available to calculate the interfacial fracture toughness.

Both nanoindentation and nano-scratching provide the scope to

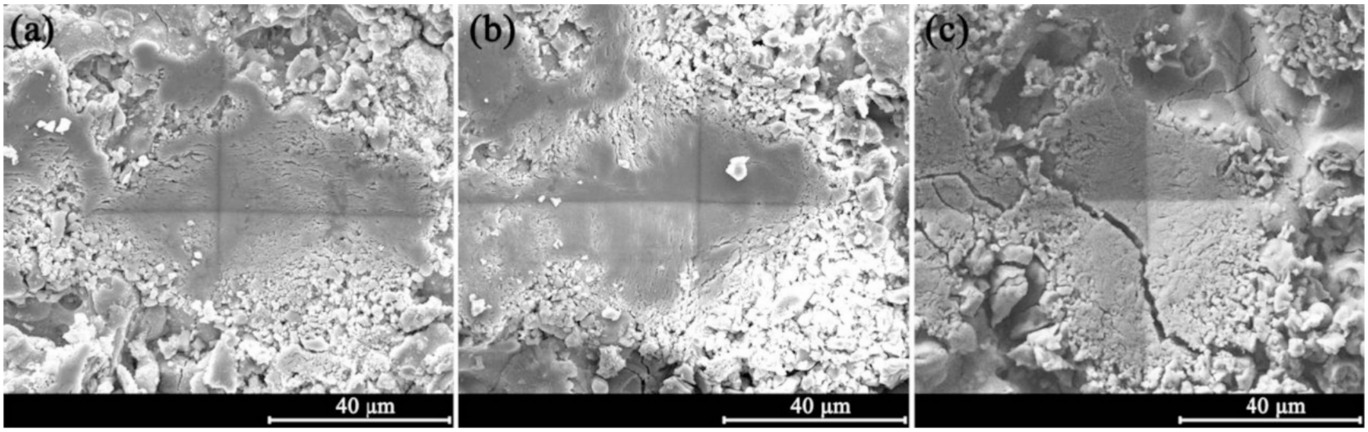

Fig. 76. The SEM observation of residual indentation impression at (a) 25, (b) 1000 and (c) 1200 °C, respectively [168].

Table 2
Criteria for the selection of the test method for multilayered ceramic coatings.

Method	Application	In/ Ex-situ	Test conditions	Specimen preparation	Test setup	Crack Length Monitoring	Closed-form solution	Failure mode	Interfacial Fracture Toughness	Interfacial Fracture Energy
Double Cantilever Beam Test [63,64]	SOC	In-situ	RT	Notch required, specimen preparation less complicated (++)	Complex (+)	Required	Yes	Mode I, crack opening	No	Yes
Wedge Impression Test [84,85]	TBC	Ex-situ	RT	Notch not required, specimen preparation less complicated (++)	Easy (+++)	Required	Yes	Mode II, shear failure	Yes	Yes
Wedge Test [66,67]	EBC, TBC	In-situ	RT	Notch required, specimen preparation less complicated (++)	Complicated (+)	Required	Yes	Mode I, crack opening	No	Yes
Single Wedge Test [88]	SOC	Ex-situ	RT	Pre-crack required, simple specimen preparation (+++)	Easy (+++)	Required	Yes	Mode I, crack opening	No	Yes
Rockwell Indentation Test [89]	TBC	Ex-situ	RT	Notch not required, simple specimen preparation (+++)	Easy (+++)	Required	Yes	Mixed-Mode I/II	Yes	Yes
Vickers Indentation Test [90]	TBC	Ex-situ	RT	Notch not required, specimen preparation less complex (++)	Less complex (++)	Required	Yes	Mode I, crack opening	Yes	No
Instrumental Indentation Test [94,95]	TBC	Ex-situ	RT	Notch not required, specimen preparation less complex (++)	Less complicated (++)	Required	Yes	Mode I, crack opening	Yes	No
Modified micro- Vickers Indentation Test [68]	TBC	Ex-situ	RT	Notch not required, specimen preparation less complex (++)	Less complex (++)	Required	Yes	Mode I, crack opening	Yes	No
Cross-sectional Indentation Test [69]	TBC	Ex-situ	RT	Notch not required, Specimen preparation less complex (++)	Less challenging (++)	Required	Yes	Mixed-Mode I/II	No	Yes
Rockwell Indentation Test [99]	SOC	Ex-situ	RT	Notch not required, specimen preparation easy (+++)	Easy (+++)	Required	Yes	Mode II, shear failure	Yes	Yes
Nanoindentation [12,13,100,101,102]	SOC	In/ Ex-situ	RT	Notch not required, specimen preparation complex (+)	Complex (+)	Required	Yes	Mode I, crack opening	No, only total fracture toughness of LSCF cathodes	No
In-situ indentation using X-ray imaging [170]	TBC	In-situ	RT, HT	Not required, Specimen preparation complex (+)	Complex (+)	Required	Yes	Mixed-Mode I/II	Yes	Yes
Nano-Scratch Test [111]	EBC	Ex-situ	RT	Notch not required, specimen preparation less complex (++)	Less complicated (++)	Not required	Yes	Mode II	Yes	Yes
3 PB Test [116,117,118,120]	TBC	In-situ	RT	Pre-crack required, complex specimen preparation (+)	Less complex (++)	Required	Yes	Mixed-Mode I/II, Mode I	No	Yes
3 PB Test with Schwickerath crack initiation test [121]	SOC	Ex-situ	RT	Pre-crack required, relatively complex specimen preparation (+)	Less challenging (++)	Not required	Not applicable	Not applicable	No fracture toughness, bonding strength	No
4 PB Test [122]	TBC	Ex-situ	RT	Notch required, complex specimen preparation (+)	Less complex (++)	Not required	Yes	Mixed-Mode I/II	No	Yes
4 PB Test [125]	TBC	In-situ	RT	Notch required, complex specimen preparation (+)	Complex (+)	Required	Yes	Mixed-Mode I/II	No	Yes
Asymmetric 4 PB Test with single crack [126]	TBC	In-situ	RT	Pre-crack required, complex specimen preparation (+)	Complicated (+)	Required	Yes	Mixed-Mode I/II	No	Yes
Asymmetric Modified 4 PB Test [127]	TBC	Ex-Situ	RT	Notch required, complex specimen preparation (+)	Less complex (++)	Not required	Yes	Mixed-Mode I/II	No	Yes
In-situ 4 PB Test [128]	TBC	In-situ	RT	Notch not required, specimen preparation less complex (++)	Complex (+)	Required	Yes	Mixed-Mode I/II	No	Yes
4 PB Test with Acoustic Emission [129]	TBC	In-situ	RT	Notch required, specimen preparation less complex (++)	Less complex (++)	Not required	Yes	Mixed-Mode I/II	Yes	No
4 PB Test [70,71,130,131]	SOC	Ex-situ	RT	Notch required, complex specimen preparation (+)	Less complicated (++)	Not required	Yes	Mixed-Mode I/II	No	Yes

(*continued on next page*)

Table 2 (*continued*)

Method	Application	In/Ex-situ	Test conditions	Specimen preparation	Test setup	Crack Length Monitoring	Closed-form solution	Failure mode	Interfacial Fracture Toughness	Interfacial Fracture Energy
4 point flexure Test [163,164]	EBC/CMC	In-situ	RT, HT	Notch not required, simple specimen preparation (+++)	Complex (+)	Required	Yes	No	No	Yes
Laser induced 4 PB Test [165]	EBC/CMC	In-situ	RT, HT	Notch not required, simple specimen preparation (+++)	Less complex (++)	Required	No	No	No	No
Barb Pullout Test [132,133]	TBC	Ex-situ	RT	Complex specimen preparation (+)	Complex (+)	Not required	Yes	Mixed-Mode I/II	No	Yes
Pushout Test [137,138]	TBC	Ex-situ	RT	Complex specimen preparation (+)	Less complex (++)	Not required	Yes	Mode II, shear failure	No	Yes
Compression test [158]	TBC	In-situ	RT	Pre-crack required, specimen preparation less complicated	Less complex (++)	Required	No	Mixed-Mode	No	Yes
Tensile Test [161]	TBC	In-situ	HT	Simple specimen preparation (+++)	Complex (+)	Not required	Yes	Mode I, crack opening	Yes	Yes
Bi-axial Mixed-Mode Test [139,140]	TBC	In-situ	RT, HT	Pre-crack required, complex specimen preparation (+)	Complex (+)	Required	Yes	Mixed-Mode I/II	Yes	Yes
Mixed-Mode Test [141]	TBC	Ex-situ	RT, HT	Pre-crack required, specimen preparation less complex (++)	Less complex (++)	Required	Yes	Mixed-Mode I/II	Yes	Yes
In-situ 3 PB Test [162]	TBC	In-situ	RT, HT	Notch required, specimen preparation less complex (++)	Complex (+)	Required	Yes	Mode I, crack opening	No, only total fracture toughness for topcoat	Yes
Nanoindentation [166]	TBC	Ex-situ	RT, HT	Notch not required, specimen preparation less complicated (++)	Less complex (++)	Required	Yes	Mode I, crack opening	No, only total fracture toughness of TBC	No
Indentation [167,169]	TBC	In-situ	RT, HT	Notch not required, specimen preparation less complicated (++)	Complex (+)	Required	Yes	Mode I, crack opening	No, only total fracture toughness of TBC	No
Acoustic Emission (AE) Method [171]	TBC	In-situ	HT	Pre-crack not required, specimen preparation less complex (++)	Complex (+)	Not applicable	No	No	No	No
Acoustic Emission (AE) Method [172]	TBC	In-situ	HT	Pre-crack not required, specimen preparation less challenging (++)	Complex (+)	Not applicable	No	Mode I, crack opening	No	No, total fracture toughness of TBC

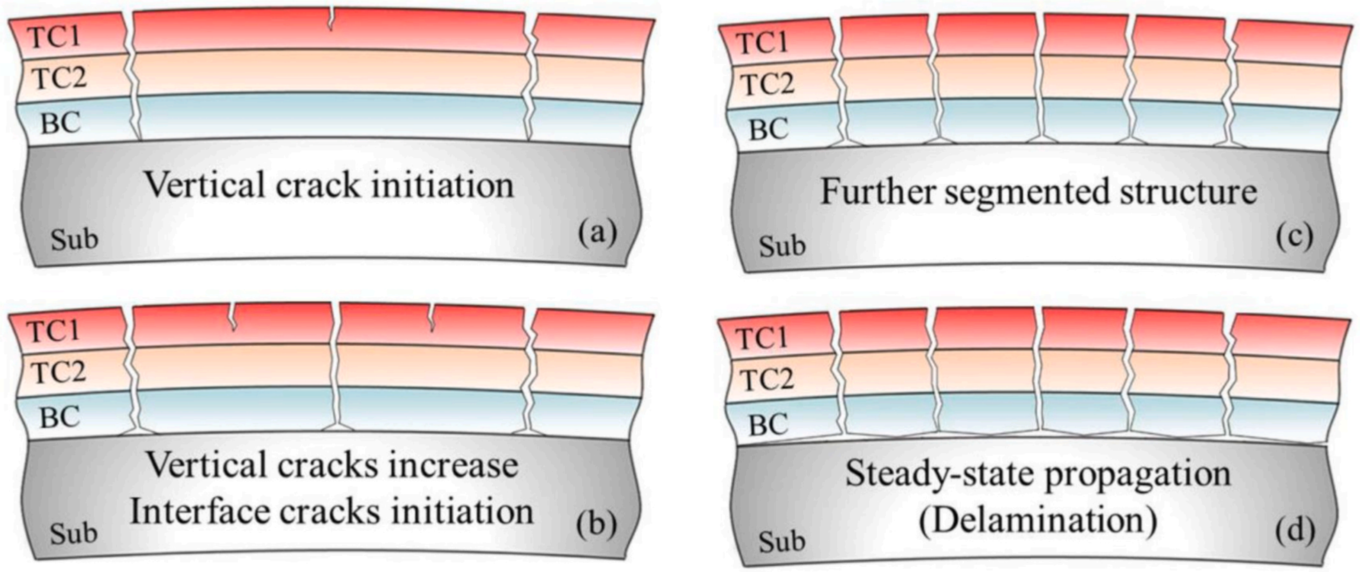

Fig. 77. Schematic of the cracking process of a coating segment and the generation of sub-segments in DCL-TBC system during bending: (a) vertical crack initiates from the top of the segment; (b) the vertical crack is arrested at BC/Substrate interface leading to two new sub-segments; (c) the multiple vertical cracks grow rapidly, and a further segmented structure is formed in DCL-TBC system; (d) at a critical moment, the steady-state propagation occurs at the interface [128].

determine the interfacial fracture toughness for small and thin coatings at local level. The nanoindentation method does not only provide interfacial adhesion properties but also offers key mechanical properties such as elastic modulus, nano-hardness and fracture toughness of the materials locally on a microstructure level, whereas nano-scratching only provides the interfacial adhesion properties. The testing of nanoindentation and nano-scratching should be performed where the coatings are thinner than 500 μm. For thicker coatings of more than 500 μm, micro-indentation and micro-scratching tests are applicable. For macro-scale or global values, the bending tests are suitable. If tribological properties of the coatings are needed, scratch tests can be implemented from nanoscale to macro-scales depending on the demands of the user.

Furthermore, the influence of vertical cracks in the topcoat needs to be considered for interfacial fracture energy evaluation, as there is an interaction between the vertical cracks and the interfacial cracks to some point [173–175]. Thus, a cohesive zone element model was developed depending on the crack density, where the TBCs were in tension [173]. That model suggested that interfacial delamination and propagation might be stabilized by increasing the surface crack density and interfacial adhesion energy to some extent, which could delay the coating delamination and might increase the lifetime of TBCs. Vertical crack densities and failure maps were provided for the durability of TBCs by performing in-situ 4 PB test, see Fig. 77 and Fig. 78 [128]. The failure maps proposed that high interfacial fracture toughness, high interfacial shear strength and high vertical crack densities were needed to prolong the lifetime of TBCs. If there are vertical cracks or surface cracks present at the topcoat of TBCs, then tensile tests and four point bending test should be performed.

Moreover, porosity of the topcoat in TBCs would influence the test results. As the interfacial fracture toughness depends on the elastic modulus of the coating and substrates, the elastic modulus of the topcoat in TBCs would be affected by the porosity. The porous topcoat would have less elastic modulus than the dense metallic bondcoat and the metal substrate, because the pores act as defects and stress concentrations. Thus, the porosity of the topcoat of the TBCs would influence the interfacial facture toughness results. The higher the porosity of the topcoat, the lower will be the mechanical properties as well as the interfacial adhesion properties of the topcoat with the bondcoat in TBCs.

Recently, both the nanoindentation and flexural tests (three-point and four-point) offered the scope to determine the interfacial fracture toughness in ceramic coatings both at room and elevated temperatures up to 1000 °C and to determine the mechanical properties of TBCs by indentation tests upto 1200 °C [168]. A survey of test sets for the TBCs, EBCs and SOCs is listed in Table 3.

From the above-mentioned test methods, it can be noted that each of the test methods comes with different advantages and disadvantages. Considering the application, the potential candidates to determine the interfacial fracture toughness are the scratch tests, the indentation tests and the flexural tests. As mentioned in the literature, nanoindentation and flexural tests provide the facility to estimate the interfacial fracture toughness between the coating and substrate both at room and elevated temperatures. However, the suitability of nanoindentation test and flexural test for functional layered materials such as solid oxide cells less than 200 μm in thickness for both room and high temperature should be investigated, as the interfacial properties are vital for the long-term operation and further development of this type of system.

6. Conclusion

This overview article provides the scope to study the interfacial fracture toughness in ceramic coatings such as TBC, EBC and electrodes in SOCs. Because interfacial adhesion is a crucial property for the robustness of these systems. Furthermore, due to their operating conditions, these materials go through harsh environments such as elevated temperatures around 1200 °C or even more, thermal cycles and high thermo-mechanical stresses. To extend the lifetime of these materials, the failure and damage mechanisms need to be investigated. In this comprehensive review, both the cohesive and adhesive failures in ceramic coatings along with the test methods for evaluating interfacial fracture toughness are discussed. Certain criteria such as applicability, test setups, in-situ/ex-situ monitoring of crack during testing, temperature range, crack length monitoring and closed-form solution are proposed for room and elevated temperatures which will contribute to the further development of these types of coating systems.

Both the indentation tests and flexural tests offer the facility to perform the interfacial fracture test at both room and elevated

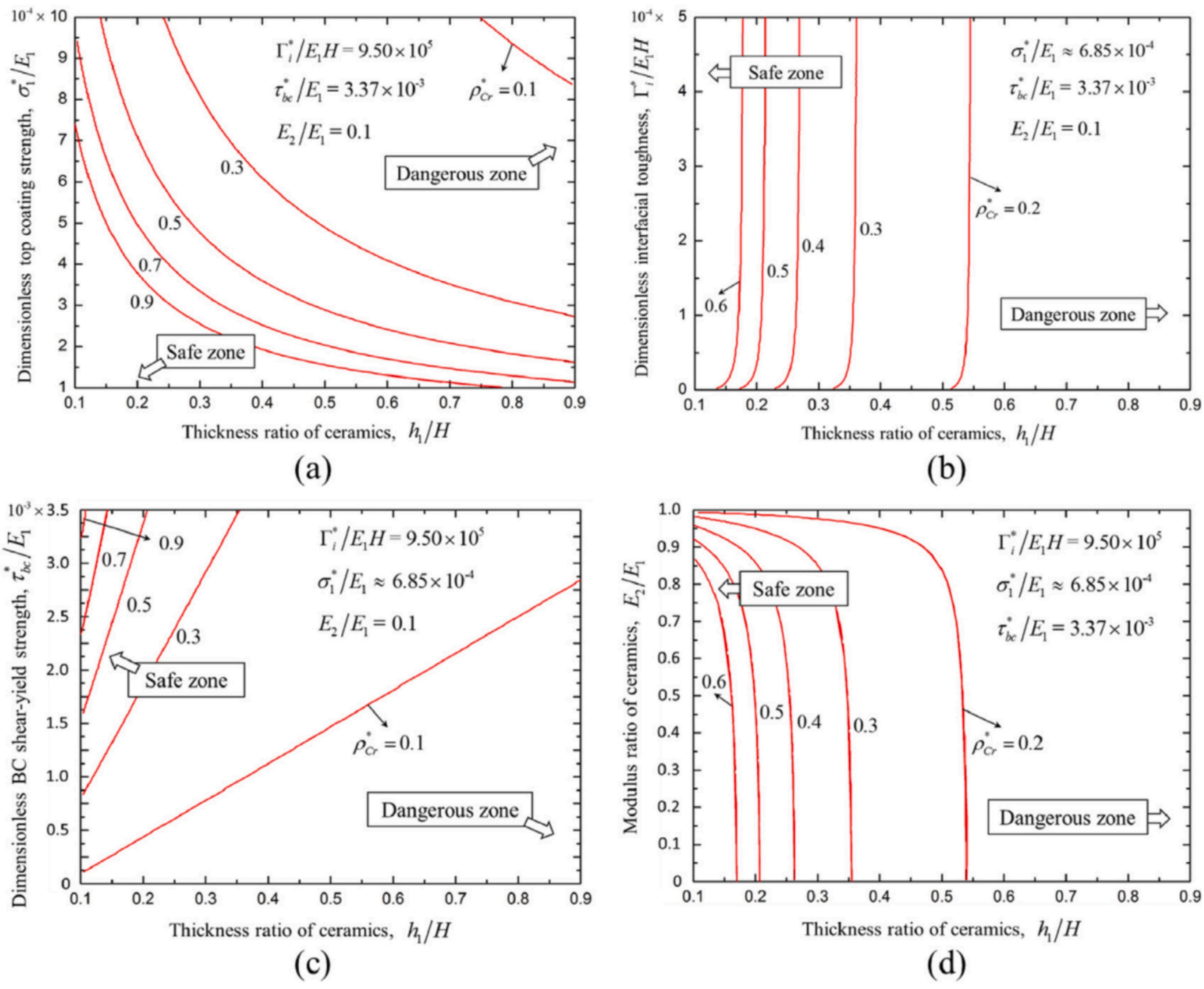

Fig. 78. Failure maps showing the effects of different factors that affect the critical crack density: (a) h_1/H and σ_1^*/E_1, (b) h_1/H and Γ_i^*/E_1H, (c) h_1/H and τ_{bc}^*/E_1, (d) h_1/H and E_2/E_1 [128].

temperatures. The recently developed in-situ nanoindentation tests employing X-Ray imaging are applicable from room temperature to 800 °C, whereas four-point flexural tests are used more than 1000 °C. The nanoindentation requires a small specimen size and suitable for both thinner and thicker coating. But the in-situ high temperature cross-sectional indentation method employing X-Ray imaging has a complex test fixture including too many features such as heating systems, rotating platform and micro-loading module. Furthermore, the test protocol is complicated, as too many features need to be utilized simultaneously. Moreover, the comprehensive test setup involves high costs and considerable amount of time.

In contrast, the flexural tests require a large specimen geometry and applicable for thicker coatings greater than 1 mm. In addition, the flexure tests require a digital image correlation (DIC) method, which necessitates specific calibration technique. From this perspective, the flexure tests are less expensive than the X-Ray imaged nanoindentation test. If complexity and cost effectiveness is not considered for the test setup and the coatings are thinner than 500 μm, the X-Ray imaged high temperature cross-sectional nanoindentation can be performed up to 800 °C. Alternatively, four-point flexure tests can be carried out with thicker coatings greater than 500 μm. It is worth noting that no test is perfect, thus a combination of the tests can be sought by implementing a test campaign to support one test with another.

High temperature scratch tests were carried out on Fe- and Ni-based alloys at 800 °C, where the scratch test device could go upto 1000 °C [176]. Additionally, high temperature nano-scratching upto 300 °C was implemented on Ti_2AlC coatings on an Inconel 625 substrate [177] and single crystal gallium nitride (GaN) upto 500 °C [178], which could be carried out in TBCs, EBCs and SOCs to determine the interfacial fracture energy at elevated temperatures. Moreover, high temperature nanoindentation was developed to test upto 1100 °C [179], which might be applicable to test the interfacial fracture toughness in TBCs, EBCs and SOCs. Furthermore, a modified cantilever beam technique was developed recently to determine the interfacial fracture energies of ceramic/metal interfaces in thermal sprayed coatings [180]. That method could be applied to TBCs and EBCs to perform tests at room temperature and might be applicable to conduct at elevated temperatures as well.

A good combination can be performing nanoindentation tests at room temperature and four-point flexure tests at elevated temperatures. Nevertheless, it depends on the user which tests need to be

Table 3
Comparison of reported test temperature and test data for interfacial adhesion testing in TBCs, EBCs and SOCs.

Method	Application	Specimen thickness	Temperature	Interfacial Fracture Toughness K (MPa.m$^{1/2}$)	Interfacial Fracture Energy G (J/m^2)
Double Cantilever Beam Test [63,64]	SOC	LSM layer: 20–50 µm Ni-YSZ: 0.3 mm	RT	Ni-YSZ: 1.80–2.16 [64]	LSM layer: 1.4–3.8 [63] Ni-YSZ: 25–30 [64]
Wedge Impression Test [84,85]	TBC	Al_2O_3 layer: 3 µm ZrO_2 layer: 100 µm Substrate: 3 mm	RT	N/A	Al_2O_3-ZrO_2 bi-layer/substrate: 56 [84,85]
Wedge Test [66]	EBC	SiC/SiCN substrate: 2 mm Si bondcoat: 300 µm $Yb_2Si_2O_7$ topcoat: 250 µm	RT	N/A	Si bondcoat/ $Yb_2Si_2O_7$ topcoat: 8–14.6 [66]
Wedge Test [67]	TBC	CoNiCrAlY bondcoat: 100 µm 8YSZ coating: 350 µm Inconel 718 Ni-based alloy substrate: N/A	RT	N/A	CoNiCrAlY bondcoat/8YSZ: 117.07 ± 19.36 (0 h oxidation) [67] 20.23 ± 0.38 (200 h oxidation) [67]
Single Wedge Test [88]	SOC	3YSZ thin beam: 0.15–0.3 mm 3YSZ substrate: 10 mm LSCF layer: 10–30 µm	RT	N/A	LSCF/3YSZ: 11 [88]
Rockwell Indentation Test [89]	TBC	Ni-based super-alloy: 3.18 mm NiCoCrAlY bondcoat: 50 µm TGO: 0.25 µm YSZ TBC: 100 µm	RT	YSZ TBC and TGO bi-layer/ NiCoCrAlY bondcoat: 1.1–3.7	YSZ TBC and TGO bi-layer/NiCoCrAlY bondcoat: 4.3–49 [89]
Vickers Indentation Test [90]	TBC	CoNiCrAlY bondcoat: 120 µm DZ40M substrate: N/A	RT	DZ40M substrate/ CoNiCrAlY bondcoat: 4.4–6.3 [90]	N/A
Instrumental Indentation Test [94,95]	TBC	Ni-based super-alloy: 5 mm CoNiCrAlY alloy bondcoat: 100 µm YSZ topcoat: 500 µm	RT	CoNiCrAlY bondcoat/YSZ topcoat: 1.3–1.9 [95]	CoNiCrAlY bondcoat/YSZ topcoat: 80–110 [94]
Modified micro- Vickers Indentation Test [68]	TBC	Ni-based super-alloy: 2.4 mm NiCrAlY bondcoat: 150 µm 8YSZ topcoat: 400–600 µm	RT	NiCrAlY bondcoat/8YSZ topcoat: 0.11–0.81 [68]	N/A
Cross-sectional Indentation Test [69]	TBC	Super-alloy: N/A Pt diffused Bondcoat: N/A 3YSZ topcoat: 130 µm	RT	N/A	Bondcoat/YSZ topcoat and TGO layer: 29 ± 9 [69]
Rockwell Indentation Test [99]	SOC	NiO-YSZ substrate: 0.8 mm NiO-SDC anode: 15 µm SDC electrolyte: 15 µm	RT	NiO-SDC anode /NiO-YSZ substrate: 0.51 [99] SDC electrolyte /NiO-SDC anode: > 0.56 [99]	NiO-SDC anode/NiO-YSZ substrate: 1.51 [99] SDC electrolyte/NiO-SDC anode: > 1.51 [99]
In-situ indentation using X-ray imaging [170]	TBC	Ni-based super-alloy: 5 mm NiCoCrAlY bondcoat: 30 µm YSZ topcoat: 70 µm	RT, 400 and 800 °C	N/A	RT: NiCoCrAlY bondcoat/YSZ topcoat: 70.15 ± 3.61 [170] 400 °C: NiCoCrAlY bondcoat/YSZ topcoat: 62.69 ± 2.36 [170] 800 °C: NiCoCrAlY bondcoat/YSZ topcoat: 33.19 ± 4.55 [170]
Nano-Scratch Test [111]	EBC	$3Al_2O_3 \cdot 2SiO_2$ film: 1.07 ± 0.15 µm SiC substrate: N/A	RT	$3Al_2O_3 \cdot 2SiO_2$ film /SiC substrate: 1–1.7	$3Al_2O_3 \cdot 2SiO_2$ film /SiC substrate: 5–20 [111]
3 PB Test [116]	TBC	Ni-based super-alloy: 2 mm NiCrAlY bondcoat: 150 µm YSZ bondcoat: 400 µm	RT	NiCrAlY bondcoat/YSZ topcoat: 2.13 [116] NiCrAlY bondcoat/Ni-based super alloy: 2.27 [116]	NiCrAlY bondcoat/YSZ topcoat: 51.82 [116] NiCrAlY bondcoat/Ni-based super alloy: 23.52 [116]
3 PB Test [117]	TBC	SUS304 stainless steel substrate: 2 mm NiCoCrAl bondcoat: 100 µm YSZ topcoat: 200 µm	RT	N/A	NiCoCrAl bondcoat/ YSZ topcoat: 152 [117]
3 PB Test [118]	TBC	SUS304 stainless steel substrate: 2 mm NiCoCrAl bondcoat: 100 µm YSZ topcoat: 200 µm	RT	N/A	NiCoCrAl bondcoat/ YSZ topcoat: 77.1 [118]
3 PB Test [120]	TBC	Superalloy GH4169 substrate: 2 mm NiCoCrAl bondcoat: 150 µm YSZ topcoat: 250 µm	RT	N/A	NiCoCrAl bondcoat/ YSZ topcoat: 79 ± 9 [120]
3 PB Test with Schwickerath crack initiation test [121]	SOC	Cell thickness: 0.4 ± 0.001 mm Crofer 22 APU stainless steel interconnector: 0.3 mm	RT	N/A, only bonding strength	N/A
4 PB Test [122]	TBC	Ni-based super-alloy: 5 mm CoNiCrAlY bondcoat: 350–360 µm	RT	N/A	CoNiCrAlY bondcoat/8YSZ topcoat: 140–270 [122]

(continued on next page)

Table 3 (*continued*)

Method	Application	Specimen thickness	Temperature	Interfacial Fracture Toughness *K* (MPa.m$^{1/2}$)	Interfacial Fracture Energy *G* (J/m^2)
		8YSZ topcoat: 330–340 μm			
4 PB Test [125]	TBC	AM1 super-alloy: N/A β-(Ni,Pt)Al bondcoat: N/A β-NiAl(Zr) bondcoat: N/A YSZ topcoat: 135 μm	RT	N/A	β-(Ni,Pt)Al bondcoat/YSZ topcoat: 23–112 [125] β-NiAl(Zr) bondcoat/YSZ topcoat: 27–114 [125]
Asymmetric 4 PB Test with single crack [126]	TBC	Mild steel Q235 substrate: 4.9 mm NiCrAlY bondcoat: 100 μm 8YSZ: 250–300 μm	RT	N/A	NiCrAlY bondcoat/8YSZ topcoat: 17–35 [126]
Asymmetric Modified 4 PB Test [127]	TBC	Single crystal alloy substrate: 4.9 mm CoNiCrAlY bondcoat: 0.32–0.37 mm YSZ topcoat: 0.11–0.51 mm GZO topcoat: 0.40–0.50 mm	RT	N/A	CoNiCrAlY bondcoat/YSZ topcoat: 151.5 [127] Double layer TBC GZO topcoat/YSZ topcoat: 82.0–93.5 [127]
4 PB Test with Acoustic Emission [129]	TBC	Ni-based super-alloy substrate: 5 mm NiCoCrAlY bondcoat: 330 μm 8YSZ topcoat: 400–500 μm GZO topcoat: 100 μm	RT	NiCoCrAlY bondcoat/8YSZ topcoat: 7.58–8.41 Double layer TBC GZO topcoat/8YSZ topcoat: 4.14–5.77 [129]	N/A
4 PB Test [70]	SOC	Ni-YSZ cermet anode: 1.5 mm YSZ electrolyte: 11 μm LSM cathode: 60 μm	RT	LSM cathode/YSZ electrolyte: 0.46 ± 0.03 [70]	LSM cathode/YSZ electrolyte: 13.2 ± 1.9 [70]
4 PB Test [71]	SOC	Ni-CGO cermet anode: 60 μm YSZ electrolyte: 135 μm LSM-YSZ cathode: 33 μm	RT	N/A	LSM-YSZ cathode/YSZ electrolyte: 20.2 ± 6.7 [71]
4 PB Test [130]	SOC	Crofer 22 APU stainless steel interconnector: 310–330 μm V11 glass–ceramic sealant: 48–55 μm	RT	Crofer 22 APU interconnector/ V11 glass–ceramic sealant: 1.6–2.5 [130]	Crofer 22 APU interconnector/ V11 glass–ceramic sealant: 13.6–15.9 [130]
4 point flexure Test [163]	EBC/CMC	SiC/SiC CMC substrate: 2.7 mm EBC: 2 mm	RT, 1000 °C	N/A	CMC substrate/EBC: 67 ± 16 at RT [163] 209 ± 115 at 1000 °C [163]
Barb Pullout Test [132]	TBC	Ni-based super-alloy substrate: 2.5 mm NiCoCrAlY bondcoat: 100–150 μm YSZ topcoat: 200 μm	RT	N/A	NiCoCrAlY bondcoat/YSZ topcoat: 60–90 [132]
Barb Pullout Test [133]	TBC	Ni-based super-alloy substrate: N/A NiCoCrAlY bondcoat: 200 μm YSZ topcoat: 200–500 μm	RT	N/A	NiCoCrAlY bondcoat/YSZ topcoat: 84–123 [133]
Pushout Test [137]	TBC	Ni-based super-alloy Inconel 738LC substrate: 3 mm CoNiCrAlY bondcoat: 150 μm YSZ topcoat: 500 μm	RT	N/A	CoNiCrAlY bondcoat/YSZ topcoat: 10–115 [137]
Pushout Test [138]	TBC	Ni-based super-alloy Inconel 738LC substrate: 3 mm NiCoCrAlY bondcoat: 200 μm YSZ topcoat: 200 μm	RT	N/A	NiCoCrAlY bondcoat/YSZ topcoat: 9–95 [138]
Compression Test [158]	TBC	Ni-based super-alloy substrate: 5 mm $NiCr_{22}Al_7Y_{0.2}$ bondcoat: 100 μm YSZ topcoat: 350	RT	N/A	100–150 [158]
Tensile Test [161]	TBC	SUS304 stainless steel substrate: 1.8 mm NiCrAlY bondcoat: 100 μm YSZ topcoat: 200–400 μm	RT, 1000 °C	NiCrAlY bondcoat/YSZ topcoat: 0.9–1.5 [161]	NiCrAlY bondcoat/YSZ topcoat: 22.15–37.8 [161]
Bi-axial Mixed-Mode Test [139,140]	TBC	Ni-based super-alloy substrate: 2 mm CoNiCrAlY bondcoat: 0.1 mm YSZ topcoat: 1.0 mm	RT, 700 °C, 900 °C	CoNiCrAlY bondcoat/YSZ topcoat: 0.81–2.46 at RT [139]	CoNiCrAlY bondcoat/YSZ topcoat: 50–100 at RT [139] CoNiCrAlY bondcoat/YSZ topcoat: 90–190 at 700 °C [140] CoNiCrAlY bondcoat/YSZ topcoat: 180–190 at 900 °C [140]
Mixed-Mode Test [141]	TBC	Ni-based super-alloy substrate: 4 mm NiCoCrAlY bondcoat: 0.15 mm	RT	NiCrAlY bondcoat/YSZ topcoat: 2.22–4.66 [141]	NiCrAlY bondcoat/YSZ topcoat: 13–85 [141]

(*continued on next page*)

Table 3 (*continued*)

Method	Application	Specimen thickness	Temperature	Interfacial Fracture Toughness K (MPa.m$^{1/2}$)	Interfacial Fracture Energy G (J/m^2)
In-situ 3 PB Test [162]	TBC	YSZ topcoat: 0.3 mm Ni-based super-alloy substrate: 2 mm NiCoCrAlY bondcoat: 80 μm 8YSZ topcoat: 1 mm	RT-800 °C	N/A	NiCoCrAlY bondcoat/8YSZ topcoat: 83.7–156.3 [162]

implemented. The criteria listed in this overview article are a good guideline to carry out the desired tests based on the demand of the user and further optimize these multilayered coatings for long-term applications.

CRediT authorship contribution statement

Borhan Uddin Manam: Writing – review & editing, Writing – original draft, Investigation, Conceptualization. **Nico Langhof:** Writing – review & editing, Resources, Funding acquisition, Conceptualization. **Carolin Sitzmann:** Supervision, Resources, Funding acquisition. **Stefan Schafföner:** Writing – review & editing, Writing – original draft, Resources, Funding acquisition, Conceptualization.

Declaration of competing interest

The authors declare that they have no known competing financial interests or personal relationships that could have appeared to influence the work reported in this paper.

Acknowledgement

The authors greatly acknowledge the financial support from the German Federal Ministry of Research, Technology and Space (BMFTR) within the framework of the flagship project H_2Giga, project “HTEL-Stacks – ready for gigawatt”, via the grant number 03HY124D.

Data availability

No data was used for the research described in the article.

References

[1] T. Wei, F. Yan, J. Tian, Characterization and wear- and corrosion-resistance of microarc oxidation ceramic coatings on aluminum alloy, J. Alloy. Compd. 389 (2005) 169–176, https://doi.org/10.1016/j.jallcom.2004.05.084.

[2] N. Jacobson, E. Opila, K. Lee, Oxidation and corrosion of ceramics and ceramic matrix composites, Curr. Opin. Solid State Mater. Sci. 5 (2001) 301–309, https://doi.org/10.1016/S1359-0286(01)00009-2.

[3] M. Schacht, N. Boukis, E. Dinjus, Corrosion of alumina ceramics in acidic aqueous solutions at high temperatures and pressures, J. Mater. Sci. 35 (2000) 6251–6258, https://doi.org/10.1023/A:1026714218522.

[4] S. Ueno, N. Kondo, D. Jayaseelan, T. Ohji, S. Kanzaki, High temperature hydro corrosion resistance of silica based oxide ceramics, Turbo Expo: Power for Land, Sea, and Air 36843 (2003) 625–632, https://doi.org/10.1115/GT2003-38878.

[5] N. Padture, M. Gell, E. Jordan, Thermal barrier coatings for gas-turbine engine applications, Science 296 (2002) 280–284, https://doi.org/10.1126/science.1068609.

[6] S. Meier, D. Gupta, The Evolution of thermal Barrier Coatings in Gas Turbine Engine applications, Journal of Engineering for Gas Turbines Power 116 (1) (1994) 250–257, https://doi.org/10.1115/1.2906801.

[7] M. Peters, C. Leyens, U. Schulz, W. Kaysser, EB-PVD thermal barrier coatings for aeroengines and gas turbines, Adv. Eng. Mater. 3 (4) (2001) 193–204, https://doi.org/10.1002/1527-2648(200104)3:4%3C193::AID-ADEM193%3E3.0.CO;2-U.

[8] K. Lee, Current status of environmental barrier coatings for Si-based ceramics, Surf. Coat. Technol. 133 (2000) 1–7, https://doi.org/10.1016/S0257-8972(00)00889-6.

[9] H. Chen, C. Zhang, Y. Liu, P. Song, W. Li, G. Yang, B. Liu, Recent progress in thermal/environmental barrier coatings and their corrosion resistance, Rare Met. 39 (2020) 498–512, https://doi.org/10.1007/s12598-019-01307-1.

[10] C.J. Li, X.T. Luo, S.W. Yao, G.R. Li, C.X. Li, G.J. Yang, The bonding formation during thermal spraying of ceramic coatings: a review, J. Therm. Spray Technol. 31 (4) (2022) 780–817, https://doi.org/10.1007/s11666-022-01379-z.

[11] A. Nakajo, J. Kuebler, A. Faes, U.F. Vogt, H.J. Schindler, L. Chiang, S. Modena, J. V. Herle, T. Hocker, Compilation of mechanical properties for the structural analysis of solid oxide fuel cell stacks. Constitutive materials of anode-supported cells, Ceram. Int. 38 (2012) 3907–3927, https://doi.org/10.1016/j.ceramint.2012.01.043.

[12] Z. Chen, X. Wang, V. Bhakhri, F. Giuliani, A. Atkinson, Nanoindentation of porous bulk and thin films of $La_{0.6}Sr_{0.4}Co_{0.2}Fe_{0.8}O_{3-\delta}$, Acta Mater. 61 (15) (2013) 5720–5734, https://doi.org/10.1016/j.actamat.2013.06.016.

[13] Z. Chen, X. Wang, F. Giuliani, A. Atkinson, Fracture Toughness of Porous Material of LSCF in Bulk and Film Forms, J. Am. Ceram. Soc. (2015) 1–8, https://doi.org/10.1111/jace.13507.

[14] Y.G. Yushkov, E.M. Oks, A.V. Tyunkov, A.Y. Yushenko, D.B. Zolotukhin, Electron-beam deposition of aluminum nitride and oxide ceramic coatings for microelectronic devices, Coatings 11 (6) (2021) 645, https://doi.org/10.3390/coatings11060645.

[15] S.Y. Je, B.G. Son, H.G. Kim, M.Y. Park, L.M. Do, R. Choi, J.K. Jeong, Solution-Processable $LaZrO_x/SiO_2$ Gate Dielectric at Low Temperature of 180 °C for High-Performance Metal Oxide Field-effect Transistors, ACS Appl. Mater. Interfaces 6 (21) (2014) 18693–18703, https://doi.org/10.1021/am504231h.

[16] K.S. Park, P.S. Ko, S.D. Kim, Effects of N_2O plasma treatment on perhydropolysilazane spin-on-dielectrics for inter-layer-dielectric applications, Thin Solid Films 551 (2014) 57–60, https://doi.org/10.1016/j.tsf.2013.11.104.

[17] A. Mallik, “Ceramic coatings for semiconductors,” in *In Advanced Ceramic*, Coatings (2023) 255–267, https://doi.org/10.1016/B978-0-323-99659-4.00009-7.

[18] S. Choi, J. Hutchinson, A. Evans, Delamination of multilayer thermal barrier coatings, Mech. Mater. 31 (1999) 431–447, https://doi.org/10.1016/S0167-6636(99)00016-2.

[19] T. Patterson, D. Orloff, F. Bloom, Delamination Buckling and Spalling of Plasma Sprayed thermal Barrier Coatings, Math. Comput. Model. 35 (2002) 165–190, https://doi.org/10.1016/S0895-7177(01)00158-3.

[20] X. Chen, J. Hutchinson, M. He, A. Evans, On the propagation and coalescence of delamination cracks in compressed coatings: with application to thermal barrier systems, Acta Mater. 51 (2003) 2017–2030, https://doi.org/10.1016/S1359-6454(02)00620-1.

[21] W. Mao, C. Dai, Y. Zhou, Q. Liu, An experimental investigation on thermo-mechanical buckling delamination failure characteristic of air plasma sprayed thermal barrier coatings, Surf. Coat. Technol. 201 (2007) 6217–6227, https://doi.org/10.1016/j.surfcoat.2006.11.025.

[22] B.T. Richards, S. Sehr, F. De Franqueville, M.R. Begley, H.N. Wadley, Fracture mechanisms of ytterbium monosilicate environmental barrier coatings during cyclic thermal exposure, Acta Mater. 103 (2016) 448–460, https://doi.org/10.1016/j.actamat.2015.10.019.

[23] S. Oliveira, A. Bower, An analysis of fracture and delamination in thin coatings subjected to contact loading, Wear 198 (1996) 15–32, https://doi.org/10.1016/0043-1648(95)06885-6.

[24] U. Wiklund, J. Gunnars, S. Hogmark, Influence of residual stresses on fracture and delamination of thin hard coatings, Wear 232 (1999) 262–269, https://doi.org/10.1016/S0043-1648(99)00155-6.

[25] K. Mondal, L. Nuñez III, C.M. Downey, I.J. Van Rooyen, Thermal barrier coatings overview: Design, manufacturing, and applications in high-temperature industries, Ind. Eng. Chem. Res. 60 (17) (2021) 6061–6077, https://doi.org/10.1021/acs.iecr.1c00788.

[26] B.T. Richards, H.N. Wadley, Plasma spray deposition of tri-layer environmental barrier coatings, J. Eur. Ceram. Soc. 34 (12) (2014) 3069–3083, https://doi.org/10.1016/j.jeurceramsoc.2014.04.027.

[27] M.B. Mogensen, M. Chen, H.L. Frandsen, C. Graves, J.B. Hansen, K.V. Hansen, A. Hauch, T. Jacobsen, S.H. Jensen, T.L. Skafte, X. Sun, Reversible solid-oxide cells for clean and sustainable energy, Clean Energy 3 (3) (2019) 175–201. https://doi:10.1093/ce/zkz023.

[28] J. Chen, S. Bull, Approaches to investigate delamination and interfacial toughness in coated systems: an overview, J. Phys. D Appl. Phys. 44 (2011) 34001, https://doi.org/10.1088/0022-3727/44/3/034001.

[29] Z. Chen, K. Zhou, X. Lu, Y.C. Lam, A review on the mechanical methods for evaluating coating adhesion, Acta Mech. 225 (2014) 431–452, https://doi.org/10.1007/s00707-013-0979-y.

[30] G. Li, C. Tang, G. Yang, Dynamic-stiffening-induced aggravated cracking behavior driven by metal-substrate-constraint in a coating/substrate system, Journal of Materials Science & Technology 65 (2021) 154–163, https://doi.org/10.1016/j.jmst.2020.04.076.

[31] Z. Wei, H.N. Cai, Understanding the failure Mechanism of thermal Barrier Coatings considering the Local Bulge at the Interface between YSZ Ceramic and Bond Layer, Materials (basel, Switzerland) 15 (2021) 275, https://doi.org/10.3390/ma15010275.

[32] F. Xiao, S. Liu, J. Xia, J.W. Guo, W. Zhu, Corrosion of tri-layer $LaMgAl_{11}O_{19}$/Yb_2SiO_5/Si environmental barrier coatings with molten calcium-magnesium-alumina-silicate (CMAS), Corros. Sci. 227 (2024) 111781, https://doi.org/10.1016/j.corsci.2023.111781.

[33] M. Leite, U. Degenhardt, W. Krenkel, S. Schafföner, G. Motz, In Situ Generated $Yb_2Si_2O_7$ Environmental Barrier Coatings for Protection of Ceramic Components in the Next Generation of Gas Turbines, Adv. Mater. Interfaces 9 (2022) 2102255, https://doi.org/10.1002/admi.202102255.

[34] C. Levi, J. Hutchinson, M.H. Vidal-Sétif, C. Johnson, Environmental degradation of thermal-barrier coatings by molten deposits, MRS Bull. 37 (2012) 932–941, https://doi.org/10.1557/mrs.2012.230.

[35] J. Perepezko, The hotter the engine, the better, Science 326 (2009) 1068–1069, https://doi.org/10.1126/science.1179327.

[36] A. Nieto, R. Agrawal, L. Bravo, C. Hofmeister-Mock, M. Pepi, A. Ghoshal, Calcia–magnesia–alumina–silicate (CMAS) attack mechanisms and roadmap towards Sandphobic thermal and environmental barrier coatings, Int. Mater. Rev. 66 (2021) 451–492, https://doi.org/10.1080/09506608.2020.1824414.

[37] X. Hu, G. Liu, Q. Liu, W. Zhu, S. Liu, Z. Ma, Failure Mechanism of EB-PVD thermal Barrier Coatings under the Synergistic effect of thermal shock and CMAS Corrosion, Coatings 12 (2022) 1290, https://doi.org/10.3390/coatings12091290.

[38] T. Riyadi, D. Setiadhi, A. Anggono, W. Siswanto, H. Al-Kayiem, Analysis of mechanical and thermal stresses due to TiN coating of Fe substrate by physical vapor deposition, Forces Mech. 4 (2021) 100042, https://doi.org/10.1016/j.finmec.2021.100042.

[39] D. S. Rickerby and P. Morrell, "Advantages/Disadvantages of various TBC systems as perceived by the Engine Manufacturer," *ROLLS ROYCE PLC-REPORT-PNR,* 1998.

[40] M. Watanabe, C. Mercer, C.G. Levi, A.G. Evans, A probe for the high temperature deformation of thermal barrier oxides, Acta Mater. 52 (2004) 1479–1487, https://doi.org/10.1016/j.actamat.2003.11.029.

[41] J.R. Nicholls, Y. Jaslier, D.S. Rickerby, Erosion and Foreign Object damage of thermal Barrier coatings, Mater. Sci. Forum 251 (1997) 935–948, https://doi.org/10.4028/www.scientific.net/MSF.251-254.935.

[42] J.R. Nicholls, Y. Jaslier, D.S. Rickerby, Erosion of EB-PVD thermal Barrier Coatings, Mater. High Temp. 15 (1998) 15–22, https://doi.org/10.1080/09603409.1998.11689572.

[43] X. Chen, J.W. Hutchinson, A.G. Evans, Simulation of the High Temperature Impression of thermal Barrier Coatings with Columnar Microstructure, Acta Mater. 52 (2004) 565–571, https://doi.org/10.1016/j.actamat.2003.09.047.

[44] X. Chen, R. Wang, N. Yao, A.G. Evans, J.W. Hutchinson, R.W. Bruce, Foreign object damage in a thermal barrier system: mechanisms and simulations, Mater. Sci. Eng. A 352 (2003) 221–231, https://doi.org/10.1016/S0921-5093(02)00905-X.

[45] J.R. Nicholls, R.G. Wellman, Erosion and Foreign Object Damage of Thermal Barrier Coatings, in: The Control and Reduction of Wear in Military Platforms, Williamsburg, USA, 2003.

[46] A. Evans, J. Hutchinson, The mechanics of coating delamination in thermal gradients, Surf. Coat. Technol. 201 (2007) 7905–7916, https://doi.org/10.1016/j.surfcoat.2007.03.029.

[47] A. El-amiri, A. Saifi, A. Obbadi, Y. Errami, S. Sahnoun, A. Elhassnaoui, Control of Solid Oxide fuel Cells damage using Infared Thermography, in: *International Renewable and Sustainable Energy Conference (IRSEC)*, 2017, pp. 1–6, https://doi.org/10.1016/j.ijhydene.2018.04.222.

[48] M.A. Laguna-Bercero, R. Campana, A. Larrea, J.A. Kilner, V.M. Orera, Electrolyte degradation in anode supported microtubular yttria stabilized zirconia-based solid oxide steam electrolysis cells at high voltages of operation, J. Power Sources 196 (21) (2011) 8942–8947, https://doi.org/10.1016/j.jpowsour.2011.01.015.

[49] K.J. Soderholm, Review of the fracture toughness approach, Dent. Mater. 26 (2) (2010) e63–e77, https://doi.org/10.1016/j.dental.2009.11.151.

[50] J.W. Hutchinson, Z. Suo, Mixed-mode cracking in layered materials, Adv. Appl. Mech. 29 (1992) 63–191, https://doi.org/10.1016/S0065-2156(08)70164-9.

[51] R.G. Hutchinson, J.W. Hutchinson, Lifetime Assessment for thermal Barrier Coatings: Tests for measuring mixed Mode Delamination Toughness, J. Am. Ceram. Soc. 94 (S1) (2011) S85–S95, https://doi.org/10.1111/j.1551-2916.2011.04499.x.

[52] J. Rice, Elastic fracture mechanics concepts for interfacial cracks, J. Appl. Mech. 55 (1988) 98–103, https://doi.org/10.1115/1.3173668.

[53] N.W. Klingbeil, J.L. Beuth, Interfacial fracture testing of deposited metal layers under four-point bending, Eng. Fract. Mech. 56 (1997) 113–126, https://doi.org/10.1016/S0013-7944(96)00109-9.

[54] J. Dundurs, Edge-bonded dissimilar orthogonal elastic wedges, J. Appl. Mech. 36 (1969) 650–652, https://doi.org/10.1115/1.3564739.

[55] ASTM D4541-17: Standard Test Method for Pull-Off Strength of Coatings Using Portable Adhesion Testers. https://doi.org/10.1520/D4541-17.

[56] K. Kendall, Thin-film peeling-the elastic term, J. Phys. D Appl. Phys. 8 (1975) 1449, https://doi.org/10.1088/0022-3727/8/13/005.

[57] S. Bull, D. Rickerby, A. Matthews, A. Leyland, A. Pace, J. Valli, The use of scratch adhesion testing for the determination of interfacial adhesion: the importance of frictional drag, Surf. Coat. Technol. 36 (1988) 503–517, https://doi.org/10.1016/0257-8972(88)90178-8.

[58] S.J. Bull, D.S. Rickerby, New developments in the modelling of the hardness and scratch adhesion of thin films, Surf. Coat. Technol. 42 (1990) 149–164, https://doi.org/10.1016/0257-8972(90)90121-R.

[59] S.J. Bull, Failure modes in scratch adhesion testing, Surf. Coat. Technol. 50 (1991) 25–32, https://doi.org/10.1016/0257-8972(91)90188-3.

[60] S.J. Bull, Failure mode maps in the thin film scratch adhesion test, Tribol. Int. 30 (1997) 491–498, https://doi.org/10.1016/S0301-679X(97)00012-1.

[61] "ASTM D3359-09: Standard Test Methods for Measuring Adhesion by Tape Test". Doi: 10.1520/D3359-09.

[62] "DIN EN ISO 2409: Paints and varnishes-Cross-cut test". https://dx.doi.org/10.31030/3171026.

[63] B.F. Sørensen, A. Horsewell, Crack Growth along Interfaces in Porous Ceramic Layers, Journal of American Ceramic Society 84 (9) (2001) 2051–2209, https://doi.org/10.1111/j.1151- 2916.2001.tb00957.x.

[64] S. Goutianos, H. Frandsen, B. Sørensen, Fracture properties of nickel-based anodes for solid oxide fuel cells, J. Eur. Ceram. Soc. 30 (2010) 3173–3179, https://doi.org/10.1016/j.jeurceramsoc.2010.07.028.

[65] H. Kakisawa, T. Nishimura, A method for testing the interface toughness of ceramic environmental barrier coatings (EBCs) on ceramic matrix composites (CMCs), J. Eur. Ceram. Soc. 38 (2) (2018) 655–663, https://doi.org/10.1016/j.jeurceramsoc.2017.09.032.

[66] M. Wolf, H. Kakisawa, F. Süß, D.E. Mack, R. Vaßen, Determining Interface Fracture Toughness in Multi Layered Environmental Barrier Coatings with Laser Textured Silicon Bond Coat, Coatings 11 (55) (2021) 1–12, https://doi.org/10.3390/coatings11010055.

[67] Y.M. Wang, W.X. Weng, M.H. Chi, B.L. Liu, Q. Li, Investigation into the evolution of interface fracture toughness of thermal barrier coatings with thermal exposure treatment by wedge indentation, J. Mater. Res. 35 (13) (2020) 1715–1725, https://doi.org/10.1557/jmr.2020.79.

[68] W. Mao, J. Wan, C. Dai, J. Ding, Y. Zhang, Y. Zhou, C. Lu, Evaluation of microhardness, fracture toughness and residual stress in a thermal barrier coating system: a modified Vickers indentation technique, Surf. Coat. Technol. 206 (2012) 4455–4461, https://doi.org/10.1016/j.surfcoat.2012.02.060.

[69] X. Wang, C. Wang, A. Atkinson, Interface fracture toughness in thermal barrier coatings by cross-sectional indentation, Acta Mater. 60 (2012) 6152–6163, https://doi.org/10.1016/j.actamat.2012.07.058.

[70] J. Malzbender, R.W. Steinbrech, L. Singheiser, Determination of the interfacial fracture energies of cathodes and glass ceramic sealants in a planar solid-oxide fuel cell design, J. Mater. Res. 18 (4) (2003) 929–934, https://doi.org/10.1557/JMR.2003.0127.

[71] G. Delette, J. Laurencin, M. Dupeux, J.B. Doye, Measurement of the fracture energy at the interface between porous cathode layer and electrolyte in planar solid oxide fuel cells, Scr. Mater. 59 (2008) 31–34, https://doi.org/10.1016/j.scriptamat.2008.02.018.

[72] R. Olsson, A simplified improved beam analysis of the DCB specimen, Compos. Sci. Technol. 43 (1992) 329–338, https://doi.org/10.1016/0266-3538(92)90056-9.

[73] Z. Yang, C. Sun, Interlaminar fracture toughness of a graphite/epoxy multidirectional composite, J. Eng. Mater. Technol. 122 (2000) 428–433, https://doi.org/10.1115/1.1289027.

[74] A. de Morais, M. de Moura, A. Marques, P. de Castro, Mode-I Interlaminar Fracture of Carbon/Epoxy Cross-ply Composites, Compos. Sci. Technol. 62 (2002) 679–686, https://doi.org/10.1016/S0266-3538(01)00223-8.

[75] B. Sørensen, A. Horsewell, O. Jørgensen, A. Kumar, P. Engbæk, A Fracture Resistance Measurement Method for In Situ Observation of Crack Mechanisms in Brittle Materials, Journal of American Ceramic Society 81 (3) (1998) 661–669, https://doi.org/10.1111/j.1151- 2916.1998.tb02387.x.

[76] S.W. Freiman, D.R. Mulville, P.W. Mast, "Crack Propagation Studies in Brittle Materials," *Journal of Material*, Science (1973), https://doi.org/10.1007/BF00754886.

[77] D. Dalmas, E. Barthel, D. Vandembroucq, Crack front pinning by design in planar heterogeneous interfaces, J. Mech. Phys. Solids 57 (2009) 446–457, https://doi.org/10.1016/j.jmps.2008.11.012.

[78] E. Barthel, O. Kerjan, P. Nael, N. Nadaud, Asymmetric silver to oxide adhesion in multilayers deposited on glass by sputtering, Thin Solid Films 473 (2005) 272–277, https://doi.org/10.1016/j.tsf.2004.08.017.

[79] X. Geng , "Failure Mechanisms of Weak Adhesion Optical Coatings Under Sliding Contact, Ph.D Thesis," Pierre et Marie Curie University, 2008.

[80] M. Isakov, M. May, P. Hahn, H. Paul, M. Nishi, Fracture toughness measurement without force data–Application to high rate DCB on CFRP, Compos. A Appl. Sci. Manuf. 119 (2019) 176–187, https://doi.org/10.1016/j.compositesa.2019.01.030.

[81] M. May, P. Hahn, B.U. Manam, M. Imbert, Mixed-Mode I/II Testing of Composite Materials—A Refined Data Reduction Scheme for the Wedge-Loaded Asymmetric double Cantilever Beam Test, Journal of Composites Science 6 (2022) 319, https://doi.org/10.3390/jcs6100319.

[82] F. Xiao, C.Y. Hui, E. Kramer, Analysis of a mixed mode fracture specimen: the asymmetric double cantilever beam, J. Mater. Sci. 28 (1993) 5620–5629, https://doi.org/10.1007/BF00367838.

[83] R.v. Tijum, Interface and surface roughness of polymer-metal laminates, in: Chapter-4 Crack propagation and adhesion: ADCB test, 2006, pp. 55–77.

[84] M.R. Begley, D.R. Mumm, A.G. Evans, J.W. Hutchinson, Analysis of a Wedge Impression Test for measuring the Interface Toughness between Films/Coatings and Ductile Substrates, Acta Mater. 48 (2000) 3211–3220, https://doi.org/10.1016/S1359-6454(00)00108-7.

[85] D. Mumm, A. Evans, On the Role of Imperfections in the failure of a thermal Barrier Coating made by Electron Beam Deposition, Acta Mater. 48 (2000) 1815–1827, https://doi.org/10.1016/S1359-6454(99)00473-5.

[86] G. Irwin, Measuring plane-strains near the end of a crack traversing a plate, J. Appl. Mech. 24 (1957) 361, https://doi.org/10.1115/1.4011547.

[87] A.J. Smiley, R.B. Pipes, Rate effects on mode I interlaminar fracture toughness in composite materials, J. Compos. Mater. 21 (1987) 670, https://doi.org/10.1177/002199838702100706.

[88] X. Wang, F. He, Z. Chen, A. Atkinson, Porous LSCF/Dense 3YSZ Interface Fracture Toughness measured by Single Cantilever Beam Wedge Test, J. Eur. Ceram. Soc. 34 (10) (2014) 2351–2361, https://doi.org/10.1016/j.jeurceramsoc.2014.02.008.

[89] A. Vasinonta, J. Beuth, Measurement of interfacial toughness in thermal barrier coating systems by indentation, Eng. Fract. Mech. 68 (2001) 843–860, https://doi.org/10.1016/S0013-7944(00)00130-2.

[90] Q. Hongyu, Y. Xiaoguang, L. Rui, Interfacial Fracture Toughness of APS thermal Barrier Coating under High Temperature, Key Eng. Mater. 348–349 (2007) 181–184, https://doi.org/10.4028/www.scientific.net/KEM.348-349.181.

[91] D. Chicot, P. Démarécaux, J. Lesage, Apparent interface toughness of substrate and coating couples from indentation tests, Thin Solid Films 283 (1996) 151–157, https://doi.org/10.1016/0040-6090(96)08763-9.

[92] B. Ekici, Role of impact on determination of interfacial toughness measurement by indentation for thermal barrier coating systems, Surf. Eng. 21 (2005) 456–462, https://doi.org/10.1179/174329405X68605.

[93] J. Yan, T. Leist, M. Bartsch, A. Karlsson, On Cracks and Delaminations of thermal Barrier Coatings due to Indentation Testing: Experimental Investigations, Acta Mater. 56 (15) (2008) 4080–4090, https://doi.org/10.1016/j.actamat.2008.04.039.

[94] Y. Yamazaki, S. Kuga, M. Jayaprakash, Interfacial Strength Evaluation Technique for thermal Barrier Coated Components by using Indentation Method, Procedia Eng. 10 (2011) 845–850, https://doi.org/10.1016/j.proeng.2011.04.139.

[95] Y. Yamazaki, S. Kuga, T. Yoshida, Evaluation of interfacial strength by an instrumented indentation method and its application to an actual TBC vane, Acta Metall. Sin. 24 (2) (2011) 109–117, https://doi.org/10.11890/1006-7191-112-109.

[96] B.K. Jang, S.H. Kim, C.A. Fischer, H.T. Kim, Effect of isothermal heat treatment on nanoindentation hardness and Young's modulus of 4 mol% Y_2O_3-ZrO_2 EB-PVD TBCs, Mater. Today Commun. 31 (2022) 103330, https://doi.org/10.1016/j.mtcomm.2022.103330.

[97] F. Zhou, S. Wang, B. Xu, Y. Wang, X. Zhang, Y. Wang, Nanomechanical properties of plasma-sprayed nanostructured and conventional 8YSZ thermal barrier coatings, Ceram. Int. 48 (24) (2022) 37483–37487, https://doi.org/10.1016/j.ceramint.2022.09.229.

[98] A. Kleinbichler, M.J. Pfeifenberger, J. Zechner, N.R. Moody, D.F. Bahr, M. J. Cordill, New insights into nanoindentation-based adhesion testing, JOM 69 (2017) 2237–2245, https://doi.org/10.1007/s11837-017-2496-2.

[99] Y. Xie, X. Zhang, M. Robertson, R. Maric, D. Ghosh, Measurement of the interface adhesion of solid oxide fuel cells by indentation, J. Power Sources 162 (2006) 436–443, https://doi.org/10.1016/j.jpowsour.2006.07.034.

[100] Z. Chen, X. Wang, A. Atkinson, N. Brandon, Spherical indentation of porous ceramics: Elasticity and hardness, J. Eur. Ceram. Soc. 36 (2016) 1435–1445, https://doi.org/10.1016/j.jeurceramsoc.2015.12.049.

[101] Z. Chen, X. Wang, A. Atkinson, N. Brandon, Spherical indentation of porous ceramics: Cracking and toughness, J. Eur. Ceram. Soc. 36 (2016) 3473–3480, https://doi.org/10.1016/j.jeurceramsoc.2016.05.010.

[102] Z. Chen, X. Wang, N. Brandon, A. Atkinson, Analysis of spherical indentation of porous ceramic films, J. Eur. Ceram. Soc. 37 (2017) 1031–1038, https://doi.org/10.1016/j.jeurceramsoc.2016.10.002.

[103] "ASTM C1624-05: Standard Test Method for Adhesion Strength and Mechanical Failure Modes of Ceramic Coatings by Quantitative Single Point Scratch Testing". Doi: 10.1520/C1624-05.

[104] Y. Xie, H. Hawthorne, A model for compressive coating stresses in the scratch adhesion test, Surf. Coat. Technol. 141 (2001) 15–25, https://doi.org/10.1016/S0257- 8972(01)01130-6.

[105] J. Malzbender, G. de With, A model to determine the interfacial fracture toughness for chipped coatings, Surf. Coat. Technol. 154 (2002) 21–26, https://doi.org/10.1016/S0257-8972(01)01708-X.

[106] S. Bull, E. Berasetegui, An Overview of the Potential of Quantitative Coating Adhesion Measurement by Scratch Testing 39 (2) (2006) 99–114, https://doi.org/10.1016/j.triboint.2005.04.013.

[107] J. Smolik, K. Zdunek, B. Larisch, Investigation of adhesion between component layers of a multi-layer coating TiC/Ti(C_x, N_{1-x})/TiN by the scratch-test method, Vacuum 55 (1999) 45–50, https://doi.org/10.1016/S0042-207X(99)00122-0.

[108] L. He, Z. Xu, X. Cao, X. Zhong, R. Mu, S. He, Adhesive strength of new thermal barrier coatings of rare earth zirconates, Vacuum 83 (11) (2009) 1388–1392, https://doi.org/10.1016/j.vacuum.2009.04.053.

[109] E. Roos, S.M. Naga, R.N. Richter, S. Lauf, M. Awaad, A. Lyutovich, M.A. Tameem, Electron beam physical vapour deposition and mechanical properties of c-ZrO_2-ZTA-coatings on alloy 617 substrates, Ceram. Int. 38 (4) (2012) 3317–3326, https://doi.org/10.1016/j.ceramint.2011.12.041.

[110] Y. Wang, Y. Bai, Y.T. Yin, B. Wang, Q.S. Zheng, F.L. Yu, Y.B. Qin, X.J. Zhang, M. Liu, H.D. Wang, Wide-velocity range high-energy plasma sprayed yttria-stabilized zirconia thermal barrier coating—Part I: Splashing splat formation and micro-adhesive property, Surf. Coat. Technol. 476 (2024) 130280, https://doi.org/10.1016/j.surfcoat.2023.130280.

[111] C. Botero, L. Cabezas, V. Sarin, L. Llanes, E. Jiménez-Piqué, Nanoscratch Testing of $3Al_2O_3 \cdot 2SiO_2$ EBCs: Assessment of Induced damage and Estimation of Adhesion Strength, Ceramics 6 (2023) 664–677, https://doi.org/10.3390/ceramics6010040.

[112] M. Laugier, An energy approach to the adhesion of coatings using the scratch test, Thin Solid Films 117 (1984) 243–249, https://doi.org/10.1016/0040-6090(84)90354-7.

[113] M. Thouless, An analysis of spalling in the microscratch test, Eng. Fract. Mech. 61 (1) (1998) 75–81, https://doi.org/10.1016/S0013-7944(98)00049-6.

[114] J. Den Toonder, J. Malzbender, G. de With, R. Balkenende, Fracture Toughness and Adhesion Energy of Sol-gel Coatings on Glass, J. Mater. Res. 17 (2002) 224–233, https://doi.org/10.1557/JMR.2002.0032.

[115] A.H. Paksoy, D. Scotson, E. Yilmaz, P. Xiao, Interfacial characteristics and adhesion behaviour of ytterbium silicate environmental barrier coatings exposed to steam oxidation, Corros. Sci. 251 (2025) 112879, https://doi.org/10.1016/j.corsci.2025.112879.

[116] L. Yang, Z. Zhong, J. You, Q. Zhang, Y. Zhou, W. Tang, Acoustic emission evaluation of fracture characteristics in thermal barrier coatings under bending, Surf. Coat. Technol. 232 (2013) 710–718, https://doi.org/10.1016/j.surfcoat.2013.06.085.

[117] Q. Zhu, G. Yan, J. Zhu, W. He and D. Chen, "Determination on Interfacial Fracture Toughness of Thermal Barrier Coatings," in *21st International Conference on Composite Materials*, Xi'an, 2017.

[118] Q. Zhu, W. He, L. Chen, J. Zhu, W. Hao, Interfacial toughness evaluation of thermal barrier coatings by bending test, Theoretical & Applied Mechanics Letters 8 (2018) 3–6, https://doi.org/10.1016/j.taml.2017.09.007.

[119] D. Gross and T. Seelig, Fracture Mechanics with an Introduction to Micromechanics, second ed., Newyork: Springer, 2011. Doi: 10.1007/978-3-642-19240-1.

[120] Q. Zhu, W. He, J. Zhu, Y. Zhou, L. Chen, Investigation on interfacial fracture toughness of plasma-sprayed TBCs using a three-point bending method, Surf. Coat. Technol. 353 (2018) 75–83, https://doi.org/10.1016/j.surfcoat.2018.08.070.

[121] D.N. Boccaccini, O. Sevecek, H.L. Frandsen, I. Dlouhy, S. Molin, B. Charlas, J. Hjelm, M. Cannio, P.V. Hendriksen, Determination of the bonding strength in solid oxide fuel cells'interfaces by Schwickerath crack initiation test, J. Eur. Ceram. Soc. 37 (2017) 3565–3578, https://doi.org/10.1016/j.jeurceramsoc.2017.04.018.

[122] Y. Yamazaki, A. Schmidt, A. Scholz, The determination of the delamination resistance in thermal barrier coating system by four-point bending tests, Surf. Coat. Technol. 201 (2006) 744–754, https://doi.org/10.1016/j.surfcoat.2005.12.023.

[123] I. Hofinger, M. Oechsner, H. Bahr, M. Swain, Modified four-point bending specimen for determining the interface fracture energy for thin, brittle layers, Int. J. Fract. 92 (1998) 213–220, https://doi.org/10.1023/A:1007530932726.

[124] S. Howard, Y. Tsui, T. Clyne, The effect of residual stresses on the debonding of coatings—I. a model for delamination at a bimaterial interface, Acta Metall. Mater. 42 (8) (1994) 2823–2836, https://doi.org/10.1016/0956-7151(94)90223-2.

[125] P.Y. Théry, M. Poulain, M. Dupeux, M. Braccini, Spallation of two thermal barrier coating systems: experimental study of adhesion and energetic approach to lifetime during cyclic, J. Mater. Sci. 44 (2009) 1726–1733, https://doi.org/10.1007/s10853-008-3108-x.

[126] P. Zhao, C. Sun, X. Zhu, F. Shang, C. Li, Fracture toughness measurements of plasma-sprayed thermal barrier coatings using a modified four-point bending method, Surf. Coat. Technol. 204 (2010) 4066–4074, https://doi.org/10.1016/j.surfcoat.2010.05.029.

[127] M. Frommherz, A. Scholz, M. Oechsner, E. Bakan, R. Vaßen, Gadolinium zirconate/YSZ thermal barrier coatings: Mixed-mode interfacial fracture toughness and sintering behavior, Surf. Coat. Technol. 286 (2016) 119–128, https://doi.org/10.1016/j.surfcoat.2015.12.012.

[128] P. Jiang, X. Fan, Y. Sun, D. Li, T. Wang, Bending-driven failure mechanism and modelling of double-ceramic-layer thermal barrier coating system, Int. J. Solids Struct. 130–131 (2018) 11–20, https://doi.org/10.1016/j.ijsolstr.2017.10.024.

[129] M. Rudlophi, M. Galetz, M. Schütze, Mechanical Stability Diagrams for thermal Barrier Coating Systems, J. Therm. Spray Technol. 30 (2021) 694–707, https://doi.org/10.1007/s11666-021-01163-5.

[130] I. Ritucci, R. Kiebach, B. Talic, L. Han, P. Zielke, P. Hendriksen, H. Frandsen, Improving the interface adherence at sealings in solid oxide cell stacks, J. Mater. Res. 34 (7) (2019) 1167–1178, https://doi.org/10.1557/jmr.2018.459.

[131] L. Han, B. Talic, K. Kwok, P. Hendriksen, H. Frandsen, Interface Fracture Energy of Contact Layers in a Solid Oxide Cell Stack, ACS Appl. Energy Mater. 3 (3) (2020) 2372–2385, https://doi.org/10.1021/acsaem.9b02026.

[132] S. Guo, D. Mumm, A. Karlsson, Y. Kagawa, Measurement of interfacial shear mechanical properties in thermal barrier coating systems by a barb pullout method, Scr. Mater. 53 (2005) 1043–1048, https://doi.org/10.1016/j.scriptamat.2005.07.012.

[133] S. Guo, Y. Tanaka, Y. Kagawa, Effect of interface roughness and coating thickness on interfacial shear mechanical properties of EB-PVD yttria-partially stabilized zirconia thermal barrier coating systems, J. Eur. Ceram. Soc. 27 (2007) 3425–3431, https://doi.org/10.1016/j.jeurceramsoc.2007.02.196.

[134] Y.F. Liu, Y. Kagawa, A. Evans, Analysis of a "barb test'' for measuring the mixed-mode delamination toughness of coatings, Acta Mater. 56 (2008) 43–49, https://doi.org/10.1016/j.actamat.2007.08.052.

[135] N.Y. Cao, Y.F. Liu, Y. Kagawa, Finite element analysis of a barb test for thermal barrier coating delamination toughness measurement, Surf. Coat. Technol. 202 (2008) 3109–3114, https://doi.org/10.1016/j.surfcoat.2007.11.012.

[136] N.Y. Cao, Y. Kagawa, Y.F. Liu, Stress analysis of a barb test for thermal barrier coatings, Surf. Coat. Technol. 202 (2008) 3413–3418, https://doi.org/10.1016/j.surfcoat.2007.12.011.

[137] S.S. Kim, Y.F. Liu, Y. Kagawa, Evaluation of interfacial mechanical properties under shear loading in EB-PVD TBCs by the pushout method, Acta Mater. 55 (2007) 3771–3781, https://doi.org/10.1016/j.actamat.2007.02.027.

[138] M. Tanaka, Y.F. Lui, S.S. Kim, Y. Kagawa, Delamination toughness of electron beam physical vapor deposition (EB-PVD) Y_2O_3–ZrO_2 thermal barrier coatings by the pushout method: effect of thermal cycling temperature, J. Mater. Res. 23 (9) (2008) 2382–2392, https://doi.org/10.1557/jmr.2008.0288.

[139] M. Arai, Y. Okajima, K. Kishimoto, Mixed-mode interfacial fracture toughness for thermal barrier coating, Eng. Fract. Mech. 74 (2007) 2055–2069, https://doi.org/10.1016/j.engfracmech.2006.10.021.

[140] M. Arai, K. Kishimoto, Influence of High-temperature Exposure on Interfacial Fracture Toughness of thermal Barrier Coating, Journal of Solid Mechanics and Materials Engineering 1 (8) (2007) 1005–1016, https://doi.org/10.1299/jmmp.1.1005.

[141] H. Deng, H. Shi, H. Yu, B. Zhong, Determination of mixed-mode interfacial fracture toughness for thermal barrier coatings, SCIENCE CHINA Physics, Mechanics & Astronomy 54 (4) (2011) 618–624, https://doi.org/10.1007/s11433-011-4278-0.

[142] Y. Zhou, T. Hashida, C. Jian, Determination of Interface Fracture Toughness in thermal Barrier Coating System by Blister Tests, J. Eng. Mater. Technol. 125 (2003) 176–182, https://doi.org/10.1115/1.1555658.

[143] B. Yuan, C. Harvey, R. Thomson, G. Critchlow, S. Wang, A new spallation mechanism of thermal barrier coatings on aero-engine turbine blades, Theoretical & Applied Mechanics Letters 8 (2018) 7–11, https://doi.org/10.1016/j.taml.2018.01.007.

[144] L. Mahfouz, B. Marchand, V. Guipont, F. Coudon, V. Maurel, Driving forces in thermal barrier coatings blistering, Materialia 28 (2023) 101728, https://doi.org/10.1016/j.mtla.2023.101728.

[145] D. Liu, P. Flewitt, The Measurement of Mechanical Properties of thermal Barrier Coatings by Micro-Cantilever Tests, Key Eng. Mater. 525–526 (2012) 13–16, https://doi.org/10.4028/www.scientific.net/KEM.525-526.13.

[146] D. Liu, J. Brown and P. Flewitt, "Micro-cantilever Testing to Evaluate the Mechanical Properties of Thermal Barrier Coatings", unpublished results.

[147] Y. Chen, X. Zhang, X. Zhao, N. Markocsan, P. Nylén, P. Xiao, Measurements of Elastic Modulus and Fracture Toughness of an Air Plasma Sprayed thermal Barrier Coating using Micro-Cantilever Bending, Surf. Coat. Technol. 374 (2019) 12–20, https://doi.org/10.1016/j.surfcoat.2019.05.031.

[148] G. Dwivedi, V. Viswanathan, S. Sampath, A. Shyam, E. Lara-Curzio, Fracture Toughness of Plasma-Sprayed thermal Barrier Ceramics: Influence of Processing, Microstructure, and thermal Aging, Journal of American Ceramic Society 97 (9) (2014) 2736–2744, https://doi.org/10.1111/jace.13021.

[149] G. Pećanac, J. Wei, J. Malzbender, Fracture toughness of solid oxide fuel cell anode substrates determined by a double-torsion technique, J. Power Sources 327 (2016) 629–637, https://doi.org/10.1016/j.jpowsour.2016.07.103.

[150] Z. Xu, Y. Yang, P. Huang, X. Li, Determination of interfacial properties of thermal barrier coatings by shear test and inverse finite element method, Acta Mater. 58 (18) (2010) 5972–5979, https://doi.org/10.1016/j.actamat.2010.07.013.

[151] Y. Zhou, T. Tonomori, A. Yoshida, L. Liu, G. Bignall, T. Hashida, Fracture characteristics of thermal barrier coatings after tensile and bending tests, Surf. Coat. Technol. 157 (2002) 118–127, https://doi.org/10.1016/S0257-8972(02)00154-8.

[152] L. Yang, Y. Zhou, W. Mao, Q. Liu, Acoustic emission evaluation of the fracture behavior of APS-TBCs subjecting to bondcoating oxidation, Surface and Interface Analysis 39 (2007) 761–769, https://doi.org/10.1002/sia.2586.

[153] M. Okazaki, S. Yamagishi, Y. Yamazaki, K. Ogawa, H. Waki, M. Arai, Adhesion strength of ceramic top coat in thermal barrier coatings subjected to thermal cycles: Effects of thermal cycle testing method and environment, Int. J. Fatigue 53 (2013) 33–39, https://doi.org/10.1016/j.ijfatigue.2012.02.014.

[154] G. Maciaszek, A. Nowotnik, Influence of Bond Coat Roughness on Adhesion of thermal Barrier Coatings Deposited by the Electron Beam–Physical Vapour Deposition Process, Appl. Sci. 14 (16) (2024) 7401, https://doi.org/10.3390/app14167401.

[155] Q. Ding, L. Hu, Y. Huang, H. Lei, W. Zhang, Impact of interfacial texture on failure behaviour of 8YSZ thermal barrier coatings under thermal cyclic loading, J. Eur. Ceram. Soc. 44 (12) (2024) 7265–7276, https://doi.org/10.1016/j.jeurceramsoc.2024.04.059.

[156] C. Eberl, X. Wang, D. Gianola, T. Nguyen, M. He, A. Evans, K. Hemker, In Situ Measurement of the Toughness of the Interface between a thermal Barrier Coating and a Ni Alloy, Journal of American Ceramic Society 94 (S1) (2011) 120–127, https://doi.org/10.1111/j.1551- 2916.2011.04588.x.

[157] K. Hbaieb, Measurement of fracture toughness of anode used in Solid Oxide fuel Cell, Thin Solid Films 517 (2009) 4892–4894, https://doi.org/10.1016/j.tsf.2009.03.143.

[158] W. Zhu, L. Yang, J.W. Guo, Y.C. Zhou, C. Lu, Determination of interfacial adhesion energies of thermal barrier coatings by compression test combined with a cohesive zone finite element model, Int. J. Plast 64 (2015) 76–87, https://doi.org/10.1016/j.ijplas.2014.08.003.

[159] F. Jing, J. Yang, S. Tang, Q. Wen, T. Zhang, J. Wu, X. Fan, Quantitative characterization of the interfacial damage in EB-PVD thermal barrier coating, Coatings 12 (7) (2022) 984, https://doi.org/10.3390/coatings12070984.

[160] K. Xiong, J. Wang, C. Hou, Z. Zhou, X. Jin, X. Fan, Damage quantification and failure mechanism of EB-PVD thermal barrier coatings under CMAS corrosion, Surf. Coat. Technol. (2025) 131554, https://doi.org/10.1016/j.surfcoat.2024.131554.

[161] W. Mao, C. Dai, L. Yang, Y. Zhou, Interfacial fracture characteristic and crack propagation of thermal barrier coatings under tensile conditions at elevated temperatures, Int. J. Fract. 151 (2008) 107–120, https://doi.org/10.1007/s10704-008-9246-y.

[162] W. Zhu, Q. Wu, L. Yang, Y. Zhou, In situ characterization of high temperature elastic modulus and fracture toughness in air plasma sprayed thermal barrier coatings under bending by using digital image correlation, Ceram. Int. 46 (11) (2020) 18526–18533, https://doi.org/10.1016/j.ceramint.2020.04.158.

[163] P. Bertrand, C. Huchette, T. Archer, T. Vandellos, F. Hild, Identification of fracture properties at the interface between CMC and EBC at room and high temperatures using full field measurements, ECCM (2024, 2024.), https://doi.org/10.60691/yj56-np80.

[164] P. Bertrand, C. Huchette, T. Archer, T. Vandellos, F. Hild, Determination of interfacial fracture energy of an environmental barrier coating on ceramic matrix composite substrate, J. Eur. Ceram. Soc. 45 (2) (2025) 116886, https://doi.org/10.1016/j.jeurceramsoc.2024.116886.

[165] I. Hamadouche, T. Archer, P. Beauchêne, T. Vandellos, F. Hild, Fracture mechanisms of an environmental barrier coating under thermomechanical loadings, J. Eur. Ceram. Soc. 44 (15) (2024) 116737, https://doi.org/10.1016/j.jeurceramsoc.2024.116737.

[166] F. Shang, X. Zhang, X. Guo, P. Zhao, Y. Chang, Determination of high temperature mechanical properties of thermal barrier coatings by nanoindentation, Surf. Eng. 30 (4) (2014) 283–289, https://doi.org/10.1179/1743294413Y.0000000227.

[167] C. Bumgardner, B. Croom, X. Li, High-temperature delamination mechanisms of thermal barrier coatings: In-situ digital image correlation and finite element analyses, Acta Mater. 128 (2017) 54–63, https://doi.org/10.1016/j.actamat.2017.01.061.

[168] R. He, Z. Qu, Y. Pei, D. Fang, High temperature indentation tests of YSZ coatings in air up to 1200 °C, Mater. Lett. 209 (2017) 5–7, https://doi.org/10.1016/j.matlet.2017.07.091.

[169] Z. Qu, K. Wei, Q. He, R. He, Y. Pei, S. Wang, D. Fang, High temperature fracture toughness and residual stress in thermal barrier coatings evaluated by an in-situ indentation method, Ceram. Int. 44 (7) (2018) 7926–7929, https://doi.org/10.1016/j.ceramint.2018.01.230.

[170] S. Luo, R. Huang, H. Bai, P. Jiang, Z. Qu, D. Fang, Interfacial failure behavior of thermal Barrier Coatings (TBCs) at high temperatures: an in-situ indentation study based on X-ray imaging, J. Mech. Phys. Solids 187 (2024) 105647, https://doi.org/10.1016/j.jmps.2024.105647.

[171] C. Berndt, Failure processes within ceramic coatings at high temperatures, J. Mater. Sci. 24 (1989) 3511–3520, https://doi.org/10.1007/BF02385733.

[172] M. Watanabe, T. Okabe, M. Enoki, T. Kishi, Evaluation of in situ fracture toughness of ceramic coatings at elevated temperature by AE inverse analysis, Sci. Technol. Adv. Mater. 4 (2003) 205–212, https://doi.org/10.1016/S1468-6996(03)00032-9.

[173] W. Zhu, L. Yang, J.W. Guo, Y.C. Zhou, C. Lu, Numerical study on interaction of surface cracking and interfacial delamination in thermal barrier coatings under tension, Appl. Surf. Sci. 315 (2014) 292–298, https://doi.org/10.1016/j.apsusc.2014.07.142.

[174] L. Yang, Q.X. Liu, Y.C. Zhou, W.G. Mao, C. Lu, Finite element simulation on thermal fatigue of a turbine blade with thermal barrier coatings, Journal of Materials Science & Technology 30 (4) (2014) 371–380, https://doi.org/10.1016/j.jmst.2013.11.005.

[175] Z.Y. Wei, X.X. Dong, H.N. Cai, G.R. Li, S.D. Zhao, Vertical crack distribution effect on the TBC delamination induced by crack growth from the ceramic surface and near the interface, Ceram. Int. 48 (22) (2022) 33028–33040, https://doi.org/10.1016/j.ceramint.2022.07.235.

[176] M. Varga, S. Leroch, H. Rojacz, M.R. Ripoll, Study of wear mechanisms at high temperature scratch testing, Wear 388 (2017) 112–118, https://doi.org/10.1016/j.wear.2017.04.027.

[177] A. Loganathan, A. Sahu, C. Rudolf, C. Zhang, S. Rengifo, T. Laha, B. Boesl, A. Agarwal, Multi-scale tribological and nanomechanical behavior of cold sprayed Ti_2AlC MAX phase coating, Surf. Coat. Technol. 334 (2018) 384–393, https://doi.org/10.1016/j.surfcoat.2017.11.067.

[178] Y. Wang, Q. Rao, Y. Wu, H. Huang, X. Xu, Unveiling the temperature-dependent deformation mechanisms of single crystal gallium nitride in nanoscratching, Appl. Surf. Sci. 682 (2025) 161606, https://doi.org/10.1016/j.apsusc.2024.161606.

[179] C. Minnert, W.C. Oliver, K. Durst, New ultra-high temperature nanoindentation system for operating at up to 1100 °C, Mater. Des. 192 (2020) 108727, https://doi.org/10.1016/j.matdes.2020.108727.

[180] A.K. Mishra, S. Abbas, D. Srinivasan, S. Sampath, B.N. Jaya, Novel, high throughput interface fracture testing method for thermal spray coatings: the modified cantilever bend technique, J. Eur. Ceram. Soc. 44 (12) (2024) 7285–7295, https://doi.org/10.1016/j.jeurceramsoc.2024.04.074.